SILICON NITRIDE MEMBRANES AS SUBSTRATES IN MEASURING THE MECHANICAL LOSS PROPERTIES OF OPTICAL COATINGS USED IN GRAVITATIONAL WAVE DETECTION

A Thesis

Presented to

The Faculty of the Physics Department

California State University, Los Angeles

In Partial Fulfillment

of the Requirements for the Degree

Master of Science

In

Physics

By

Seth David Linker

May 2018

LIGO-P1800110-v1

© 2018

Seth David Linker

ALL RIGHTS RESERVED

The thesis of Seth David Linker is approved.

Jose Rodriguez, Committee Chair

Riccardo DeSalvo

Oscar Bernal

Radi Al-Jishi, Department Chair

California State University, Los Angeles

May 2018

ABSTRACT

Study of Silicon Nitride Membranes as Substrates for Measuring the Mechanical Loss Properties of Optical Coatings Used in Gravitational Wave Detection

By

Seth David Linker

Thermal noise due to the interaction of optical coatings with their environment is a fundamental source of noise in the current generation of gravitational wave detectors. Thermal noise is suppressed in high Quality (Q) factor materials. It is crucial to accurately characterize materials and coating methods that yield the largest possible mechanical Q factor. Current methods to measure the Q of optical coating candidates suffer in precision due to their deposition onto relatively much thicker substrates which store a disproportionate fraction of the elastic energy of oscillations monitored during measurements. We propose a new experimental approach that may more precisely measure the Q of coatings by drastically reducing the elastic energy stored in the substrates, depositing the coatings onto 100 nm thick Silicon Nitride membranes.

ACKNOWLEDGMENTS

Thank you to my colleagues at California State University, Los Angeles for their help during the research performed for this thesis. Especially, Joshua Neilson, Michael Milovich Goff, Lamar Glover, Morgan Shaner and Alex Kass from the Physics department and Joseph Tien, Ian Marquez, Xavier Talbot-Thiebaux, Dustin Krogstad, and Matthew Schwab from the Engineering department.

I would also like to thank the professors and researchers from CSULA and Caltech who gave me access to their experience and knowledge, especially Dr. Marina Mondin and Dr. Gabriele Vajente.

Thank you to my family and my friends who have given me strength and enabled me to remain centered throughout a long academic career. Special thanks to my Mother, Father, Sister, and my partner and love of my life, Sarah Madden.

A most special thank you goes, finally to Dr. Riccardo DeSalvo who's joy of life and Physics are not mutually exclusive, and who gave me all of the opportunities involved with this research. It has been the most fortunate chance to meet him and thus become part of a global scientific experiment with both academic and popular appeal. To be a part of LIGO is to be part of a family of supportive scientists, and I hope to continue the relationship.

This thesis is registered on the LIGO Document Control Center with the number LIGO-P1800110-v1 and I gratefully acknowledge support from the NSF-CCR grant.

TABLE OF CONTENTS

Abstract iv

Acknowledgments v

List of Tables ix

List of Figures x

Chapter

1. Introduction 1

1.1 The Theoretical Prediction of Gravitational Waves 1

1.2 Magnitude of Space-Time Strain 3

1.3 Polarization of Gravitational Waves 5

1.4 Detecting Gravitational Waves with a Laser Interferometer 7

2. The LIGO and Virgo Detectors 11

2.1 Basic Operation of the LIGO Detector 11

2.2 Detections of Gravitational Waves by LIGO and Virgo 15

2.3 Characterizing the Strain Due to Noise in a GW Detector 19

2.4 Sources of Noise 22

Seismic Noise 22

Suspension Thermal Noise 23

Newtonian or Gravity Gradient Noise 23

Excess Gas Noise 24

Coating Thermo-Optic Noise 24

Quantum Noise 25

Coating Brownian Noise 27

2.4 The LIGO Sensitivity Standard 27

3. Coating Brownian Noise 30

3.1 The Fluctuation Dissipation Theorem and Brownian Motion 30

3.2 Mechanical Quality Factor 35

Qualitative Explanation of the Fluctuating Force Causing Thermal Noise 36

Resonance Width and Amplitude 38

Quality Factor Versus Frequency 39

Examples of Quality Factor Frequency Dependence 39

3.3 LIGO's Optical Coatings 42

Mechanical Losses in Actual Mirrors 45

3.4 Levin's Formula for Coating Noise 48

3.5 Methods for Measurements of the Loss Angle of Optical Coatings 53

Coating a Substrate 54

Extracting the Loss Angle by Subtraction 57

The Cantilever Method 59

Gentle Nodal Suspension 62

Summary of Dilution Factors and Nano-layer Motivation 65

4. Our Method 67

4.1 Silicon Nitride Membranes as Substrates 67

4.2 The Evolution of Our Proposed Method 75

The Michelson 75

The Weighted Membrane 77

Weighted Membrane Prototypes..... 79

Optical Lever Readout……...80

4.3 Gluing the Membrane to a Stage 81

Glue Tests…….....…...83

4.4 The Vacuum Chamber 85

4.5 Electrostatic Actuation..... 85

The Quadrant Position Sensitive Photodetector 90

Experimental Characterization of the Excitation System…….…93

Sweep Measurements of Q……..…100

Ring-down Measurements of Q…….…….107

4.6 Observations of the Effects of Depositing Coatings on the Membrane.. 110

5. Conclusion ……...….112

References..... 114

LIST OF TABLES

Table

1. Range of a detectable BNS merger and BBH 28
2. Data for Q measurements of 5 different samples of maraging steel 40
3. Measurements of Q for Silicon Nitride membranes 41
4. Dilution factors of coatings on cantilever blades 61
5. Various dilution factors that are yielded as a function of substrate and coating thicknesses 66
6. Comparison of dilution factors 70
7. Frequencies calculated using equation 75 73
8. Measured values performed by Zwickl et al in kHz for the same membrane dimensions 73
9. COMSOL simulation (50 nm thick, 1mm square SiN membrane) values 73
10. Finding membrane tension value to use in COMSOL simulation 74
11. COMSOL simulations of 1st mode resonant frequency for different geometries of square Silicon Nitride membranes with no island mass 75
12. The α values extracted from the fit parameters for six ring-down measurements of the first mode for the single slide glass sample 109

LIST OF FIGURES

Figure

1. A gravitational wave that is incident on the page will cause the ring of test masses to expand and contract 7
2. The arm length configuration for the Michelson interferometer 8
3. Superimposing the interferometer onto the ring of test masses 9
4. When the detector is oriented in the “Plus” configuration 9
5. Schematic of the LIGO detectors 11
6. These plots illustrate the detected laser power due to strain 14
7. The two strains in space-time transduced into a signal from the length changes in the LIGO observatories 16
8. All of the physical sources that induce a noise strain 22
9. A graph of some external fluctuating force 31
10. Amplitude of a system that is damping down as it oscillates 37
11. Results of an experiment performed to measure the Quality factor of two different polymers 40

12. LIGO's 40 kg test masses before installation 42
13. Illustration of how the test mass is mounted, SEM image of the cross section of an optical coating stack 42
14. Schematic of thin film interference 44
15. Simplified model of the multicomponent system 46
16. Log-Log plot of total Loss Angle for the system of substrate and coatings 48
17. Illustration of the pressure profile that Levin proposes 50
18. Plot of the Levin formula 53
19. Different arrangements of deposited coating layers 56
20. Simplified schematic of a typical EBID coating chamber 57
21. Photograph of a fused silica blade 60
22. First 8 mode shapes for an oscillating disc 62
23. Data extracted by (Vajente et al, 2017) using the GeNS method 63
24. View inside the vacuum chamber of the GeNS 64
25. Beam paths for the various optical levers in GeNS setup 64
26. Photograph of one of the LIGO end test masses which exhibits many scatterers 65
27. A Silicon Nitride membrane pictured next to a penny for scale 67
28. Side view illustrating the fabrication process for a Silicon Nitride membrane 68
29. Pair of graphs that show the very high Q factor for Silicon Nitride membranes.. 69
30. This arrangement minimizes the mechanical losses in the substrate 71
31. First 4 non-degenerate modes for the 1mm square, 50 nm thick membrane 74
32. Photograph of the miniature Michelson Interferometer 76
33. Schematic drawing of our miniature Michelson Interferometer 77

34. Simplified model to show how adding rigid mass to the membrane will lower the resonant frequency 78
35. Photographs of two samples fabricated by National Tsing Hua University in Taiwan..... 80
36. Differences between membrane response to actuation 80
37. Schematics of the experiment 81
38. View of the glass stage and the framed membrane sample 82
39. Illustration of the setup for the "popsicle stick" shape of the first sample 84
40. Photograph of two "popsicle stick" samples mounted 84
41. Illustration of the membrane with island mass being excited into resonance..... 86
42. The voltage divider that was used to reduce the output of the coil..... 87
43. Plot of Gain versus high values of frequency for the ignition coil 88
44. Plot of Gain versus low values of frequency for the ignition coil 88
45. The transformer used, an automobile ignition coil 89
46. Optical setup used to test the optical lever with the ignition coil actuator 89
47. The QPSPD used as well as a diagram showing the four photodiode quadrants . 90
48. Equations used to extract the position signal 90
49. The large incident spot on a changing curved surface will diverge..... 92
50. A small spot size, ~ 2mm in width, is also best for the position sensitive photo-detector to capture the motion..... 92
51. COMSOL models constructed to represent the two glass samples 94
52. Photograph of the two glass samples 94
53. The first mode shapes for the two glass samples modeled in COMSOL 95

54. The COMSOL simulated 2nd mode frequency shapes 95

55. Photograph of the actuating wire placed just along the top edge of the "double slide" sample 96

56. Graph shows the "double slide" sample being mechanically excited 97

57. The FFT data that shows the ~1kHz peak for the first mode 97

58. Photograph of the electrode orientation to drive the second resonance 98

59. The FFT data when the laser beam is incident on the sample but the actuator is moved away 99

60. Zoom in to the data of figure 59 100

61. Peak at 1040 Hz 100

62. Broad peak detected when sweeping through a range of frequencies 101

63. FFT data fitted with a Lorentzian curve 102

64. Plot of the residuals 103

65. The electrostatic comb 104

66. Photograph of the actual electrostatic comb 105

67. Comb positioned just behind the "single slide" 105

68. Excited higher order mode of the square glass slide 106

69. Captured data for a ring-down measurement 107

70. The fit for a short portion of the period before the actuation is turned off 108

71. The fit to the ring-down measurement 108

72. 100nm thick membrane coated with 100nm of Silica 111

CHAPTER 1

Introduction

1.1 The Theoretical Prediction of Gravitational Waves

Einstein's field equations tell one story from two sides.

$$G_{\mu\nu} = 8\pi\, T_{\mu\nu} \tag{1}$$

On the right-hand side sits the Stress-Energy tensor, explaining how matter behaves in a given region of space-time. This object carries information about the density in, and the flux of energy and momentum through, said region of space-time.

The left side of the equation describes the "shape" of space time with respect to a local neighborhood. It is comprised of the Ricci Curvature tensor, $R_{\mu\nu}$ an object which measures by how much a slice of a geodesic object has been altered from its original shape in Euclidean space, as well as the metric tensor, $g_{\mu\nu}$ which defines the total geometric structure of space-time.

$$G_{\mu\nu} = R_{\mu\nu} - \frac{1}{2} g_{\mu\nu} R \tag{2}$$

And so, the complete story is that the curvature of space-time dictates to mass and energy how to move, while mass and energy are continuously sculpting the curvature of space-time.

If we make the assumption that deviations from the flat space-time metric are small, which is true far from Black Holes and Neutron Stars, then the equations may be linearized into the form

$$-\bar{h}_{\mu\nu,\alpha}{}^{\alpha} = 16\pi T_{\mu\nu} \tag{3}$$

where the components of $\bar{h}$ contain information about small amplitude deviations from the flat space-time metric. The repeated Greek indices imply summing over all terms (the three spatial directions and time), and the comma instructs us to take the derivative of each term with respect to each of the four dimensions.

To provide an analogy that will "shine light" on the implications of writing the equations this way (as well as to make clearer how to understand the notation), consider a tensor that contains all the information about electric and magnetic fields, the Faraday Tensor.

$$\left\|F^{\alpha}{}_{\beta}\right\| = \begin{Vmatrix} 0 & E_x & E_y & E_z \\ E_x & 0 & B_z & -B_y \\ E_y & -B_z & 0 & B_x \\ E_z & B_y & -B_x & 0 \end{Vmatrix} \tag{4}$$

In this notation α enumerates the rows and β the columns of the tensor. One can then state (Misner, Thorne, Wheeler *Gravitation* 1973) Gauss' Law and Ampere's Circuit Law at the same time by writing

$$F^{\alpha\beta}{}_{,\beta} = 4\pi J^{\alpha} \tag{5}$$

If we take J^0 to be the charge density ρ and J^1, J^2, J^3 to be the x, y, and z components of the current density, then we can write a few terms. Starting with $\alpha = 0$, summing over all β from 0 to 3, and taking the cue from the comma to perform a derivative on each β with respect to 0,1,2, and 3 (t, x, y, z) we get

$$0 + \frac{\partial E_x}{\partial x} + \frac{\partial E_y}{\partial y} + \frac{\partial E_z}{\partial z} = 4\pi\rho \tag{6}$$

which is Gauss' Law. Stepping to the next α value, 1 we find

$$\frac{\partial E_x}{\partial t} + 0 + \frac{\partial B_z}{\partial y} - \frac{\partial B_y}{\partial z} = 4\pi J_x \tag{7}$$

or the x component of Ampere's Law. Continuing, we obtain the other two spatial dimensions. It is well known that a clever manipulation of Gauss's law and Ampere's Law leads to the wave equations that are solved by plane waves propagating at the speed of light.

The reason for this diversion was simply to illustrate that (3), apart from having a raised and lowered derivative index, behaves in the same fashion as (5). The similar mathematical form implies that the solutions to the linearized space-time field equations are also plane waves. However, as gravitational charge (mass) is only positive, the tensors of the field equations require the sources of the plane waves to be quadrupole in nature, as opposed to the dipole radiation sources of the electro-dynamical equations. This means that changes in the Stress-Energy tensor over time that possess spherical or cylindrical symmetry will not emit gravitational waves. Another difference from electromagnetic radiation is that, for gravitational waves the orthogonal polarization states that form the complete set are now rotated 45 degrees from each other ("Plus" and "Cross") as opposed to the 90 degrees ("Vertical" and "Horizontal") of light waves.

1.2 Magnitude of Space-Time Strain

It has been shown (Press and Thorne, 1972) that the distortion induced in space-time by a "slow changing source" that emits wavelengths much larger than the physical space the source occupies, may be written as

$$h \sim 10^{-16} \left(\frac{M_{eff}}{M_{\odot}}\right)\left(\frac{f\ d}{c}\right)^{2}\left(\frac{1\ kpc}{r}\right) \tag{8}$$

where M_{eff} is the effective mass of the system that is emitting the waves, $M_{\odot}$ is one solar mass, f is the frequency of the source motion, d is the overall diameter of the source, c is the speed of light, and r is the distance from the source to the detector.

First note that h is a dimensionless quantity. This is the strain of space-time

$$h = \frac{2\Delta L}{L} \tag{9}$$

i.e. the amount by which a body has been stretched in one direction and compressed in the other by a gravitational wave with respect to its original length, "h" is the amplitude of the plane wave solutions to the linearized field equations. The factor of two accounts for the symmetry of the strain in space-time and how, if the wave vector is perpendicular to the plane of the test masses, it stretches space along an axis and compresses it in the orthogonal direction. Nothing happens at 45°. This will be seen more clearly in figure 1 which shows the effect of a gravitational wave incident on a ring of test masses.

The strain is a function of the source parameters and not of the measuring stick, L. Multiplying the strain by the length of the measuring stick provides the amplitude of the mechanical signal to be detected.

Next note the coefficient, 10^{-16}. The smallness of this value comes from the small value of Newton's Universal Constant, G. Multiplying by a term with c squared in the denominator causes the strain to be exceedingly small, even for very large massive sources rotating rapidly unless the orbital velocity of the source ($f\ d$) could somehow approach the speed of light.

Note that the magnitude of strain to be detected falls of as

$$h \propto \frac{1}{r} \tag{10}$$

because it is a field to be measured, not power collected as in an optical telescope. The

GW signal, although difficult to detect, weakens much less rapidly with distance than optical, neutrino, or x-, gamma-ray signals and therefore allows detecting events from deeper in the Universe. Only radio telescopes share this interesting peculiarity, if the detector is a RF field detector. As is to be expected for quadrupole radiation it has two polarizations.

Plugging some typical values into (8):

$$\frac{M_{eff}}{M_{\odot}} = 50 \qquad f = 1000\ Hz, \qquad d = 10^5\ m, \qquad r = 500\ Mpc$$

only yields a strain in space-time of ~10^{-21}. That strain, induced by a source of 50 solar masses, spiraling 1000 times a second, would cause a 20-km long rod to change in length by only ~10^{-17} meters. The classical width of a proton is approximately 10^{-15} m.

1.3 Polarization of Gravitational Waves

The plane wave solutions to the linearized field equations may be written as

$$\bar{h}_{\mu\nu} = A_{\mu\nu} \exp(ik_{\alpha}x^{\alpha}) \tag{11}$$

following the treatment laid out in *Gravitation* (Misner, Thorne, Wheeler, 1973), the rank 2 tensor $A_{\mu\nu}$ is symmetric and so it has only 10 (not 16) independent components. Then the condition is applied that the wave vectors, k_{α} are always orthogonal to the amplitude tensor

$$A_{\mu\alpha}k^{\alpha} = 0 \tag{12}$$

and that the wave vectors are null vectors (their dot product is zero, i.e.: they have a total space-time length of zero, remembering that $s^2 = -{x_0}^2 + {x_1}^2 + {x_2}^2 + {x_3}^2$)

$$k_{\alpha}k^{\alpha} = 0 \tag{13}$$

Two more constraints, one defining a four velocity, $\vec{u}$ throughout all of space-time that is always orthogonal to the amplitude tensor

$$A_{\mu\alpha}u^{\alpha} = 0 \tag{14}$$

and, finally a gauge transformation that sets

$$A^{\mu}_{\ \mu} = 0 \tag{15}$$

reduce the, initially 10, independent components of the amplitude tensor to only 2. These two remaining components give rise to the two possible polarization states of the gravitational wave.

Now the polarization states of gravitational waves may be expressed by writing the remaining components of the plane wave solutions as

$$\bar{h}^{xx} = \bar{h}^{xx}(t - z) \tag{16}$$

$$\bar{h}^{yy} = \bar{h}^{yy}(t - z) = -\bar{h}^{xx} \tag{17}$$

$$\bar{h}^{xy} = \bar{h}^{xy}(t - z) = \bar{h}^{yx} \tag{18}$$

$$\bar{h}^{\mu 0} = \bar{h}^{\mu z} = 0 \ \{\mu \ from \ 0 \ to \ 3\} \tag{19}$$

The first two lines state that, as the wave propagates in the z direction, there may be an alternating expansion and contraction of space in the x, then y direction. This is called "Plus" (+) polarization. The third line indicates "Cross" (X) polarization and denotes an alternating expansion and contraction along the y=x and y=-x directions. The final line tells us that there is no strain in the direction of wave propagation, thus gravitational waves are transverse waves, and in fact, the gauge transformation that was used above is the TT, transverse traceless gauge.

It is traditionally useful at this point, in an explanation of how gravitational waves propagate, to show a figure of how the wave will affect a ring of test masses.

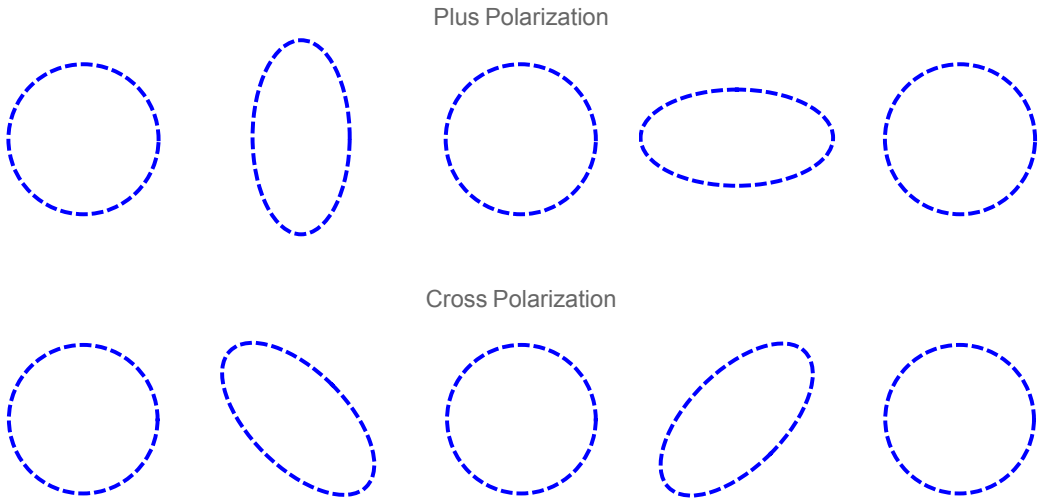


Figure 1. A gravitational wave that is incident on the page will cause the ring of test masses to expand and contract in a linear combination of + and x polarization states. The area inside the ring is conserved. Note from the second row (x polarization) how the vertical (and horizontal) dimensions do not change. Similarly, in the + polarization the diagonal dimensions do not change.

From the figure above, we may now guess a nice way to detect the passage of gravitational waves.

1.4 Detecting Gravitational Waves with a Laser Interferometer

The classical Michelson interferometer splits a laser beam into two orthogonal beams that possess half of the original intensity and travel at right angles with respect to one another. The two beams reflect off of mirrors at the ends of the arms and return to the splitting location to recombine. If the paths that the two beams took after splitting differ in length by $\frac{(2n+1)\,\lambda}{2}$, where n is an integer and λ is the wavelength of the laser, then at the anti-symmetric port (the one at 90^{o} from the symmetric port where the laser beam is injected) the two beams will be out of phase by exactly 180° and will destructively interfere on the detector, leading to no output light. The opposite case is

true for the symmetric port and all light is reflected back to the laser. This configuration can be dialed in by slowly moving the mirrors until no return signal is detected. Once locked into this configuration, the interferometer is able to detect changes in length of the two arms with respect to one another by observing the appearance of light at the anti-symmetric port with a photo detector placed just beyond the recombining plane.

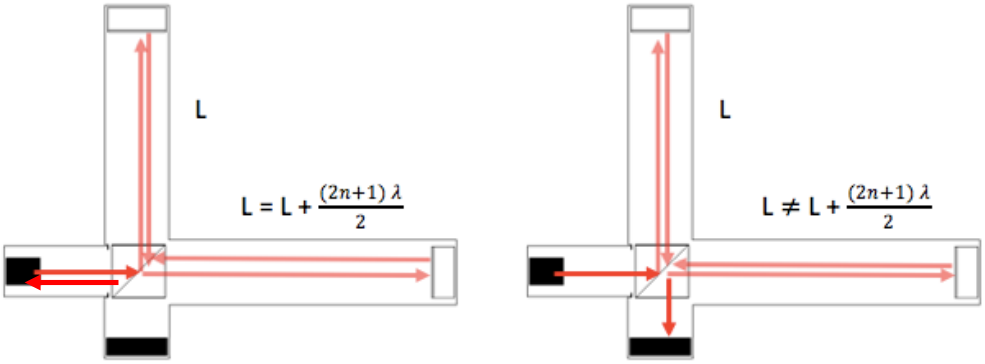


Figure 2. The arm length configuration for the Michelson interferometer on the left has no detected signal because the two beam paths acquire a π phase difference at the symmetric port. The configuration on the right shows that any incurred path length differences will result in light being transmitted and a signal being detected. The intensity of the transmitted light will be at its maximum (100%) when the arms are an integer number of wave lengths in difference. The "L" in the picture above is actually the optical path length, not the length of the arm. The difference in physical arm lengths must be $\frac{(2n+1)\,\lambda}{4}$ to achieve full destructive interference. The extra factor of ½ accounts for the fact that the light travels the same length twice since it is reflected from a mirror. The length difference of the arms for full constructive interference would then be $\frac{n\lambda}{2}$.

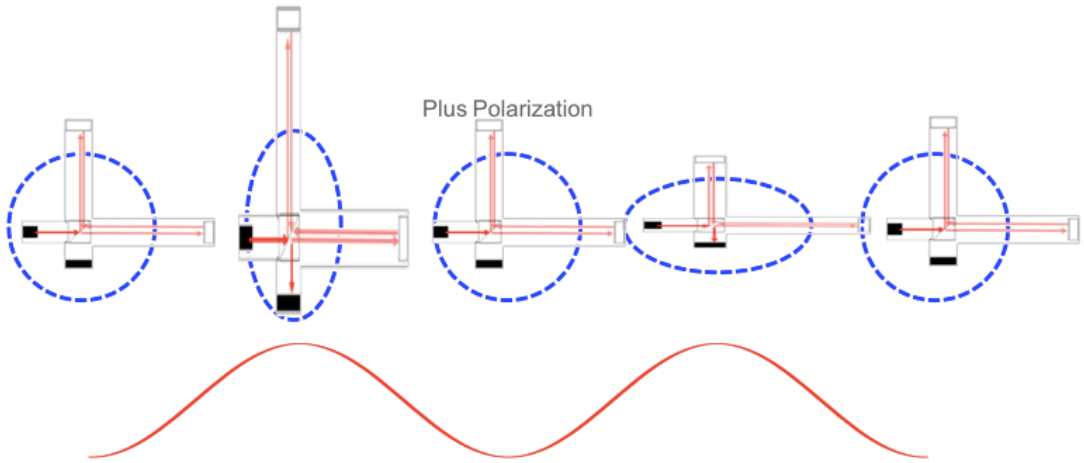


Figure 3. Here I have superimposed the interferometer onto the ring of test masses discussed in the section on polarization states of the gravitational wave. This shows that if a "Plus" polarized wave is incident on an interferometer aligned with the x and y axes, a signal will be detected that oscillates with the frequency of the wave.

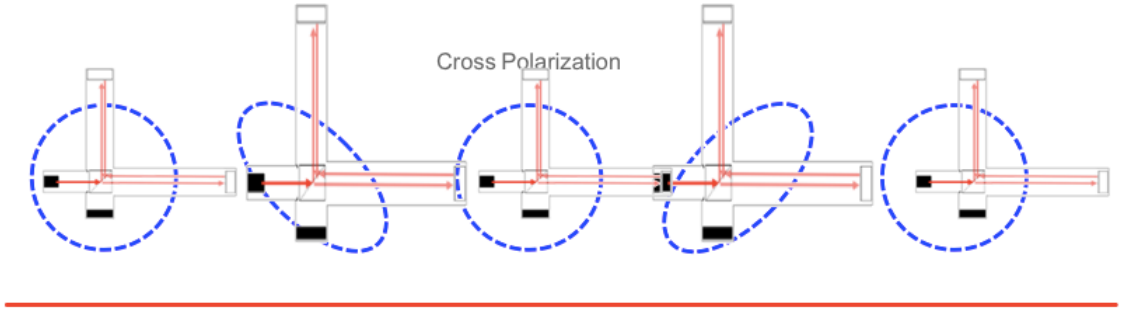


Figure 4. This image shows that when the detector is oriented in the "Plus" configuration, it will not detect a wave that is in the "Cross" polarized state. This is because the arms are not changing in the length.

Figures 3 and 4 above are an illustration of how the "Plus" and "Cross" polarization states of gravitational waves form a complete independent set, even though they are not orthogonal in the typical, 90° sense.

We may now see that a Michelson interferometer is able to detect the passage of a gravitational wave if the following two conditions are met. The first is that the wave must have a propagation vector with some component perpendicular to the plane of the interferometer. The second condition is that some component of the detector's "polarization" must be aligned with the state of the wave.

At least three interferometers located at different points on Earth could be used to "triangulate" the signal to find the direction of the astronomical source as well as the magnitude of the induced strain. Having multiple detectors also reveals information about the polarization state of the wave since only one component of a respective polarization state can be detected by a single detector

Michelson interferometers were recently used to detect and characterize gravitational waves from Black Hole and Binary Neutron Star inspiraling events. Three main detectors, two interferometers belonging to the LIGO collaboration and the Virgo one in Italy, are currently in operation on Earth.

CHAPTER 2

The LIGO and VIRGO Detectors

2.1 Basic Operation of the LIGO Detector

There are two detectors in the United States, the LIGO (Laser Interferometer Gravitational-Wave Observatory) facilities, located in Hanford, Washington and Livingston, Louisiana. The Virgo detector (so named because it was designed to be sensitive enough to detect Neutron Star inspirals as far away as the Virgo cluster of galaxies) is in Santo Stefano a Macerata, Cascina, Italy. The actual operating LIGO and Virgo detectors are much more complicated than the simplified Michelson interferometer described above. Even though they are based on the same principle, these interferometers have added features meant to increase the sensitivity and optimize the detection signal. Since the magnitudes of strain induced by astronomical events far from Earth are predicted to be on the order of ~10^{-21} some tricks must be employed to amplify the effect.

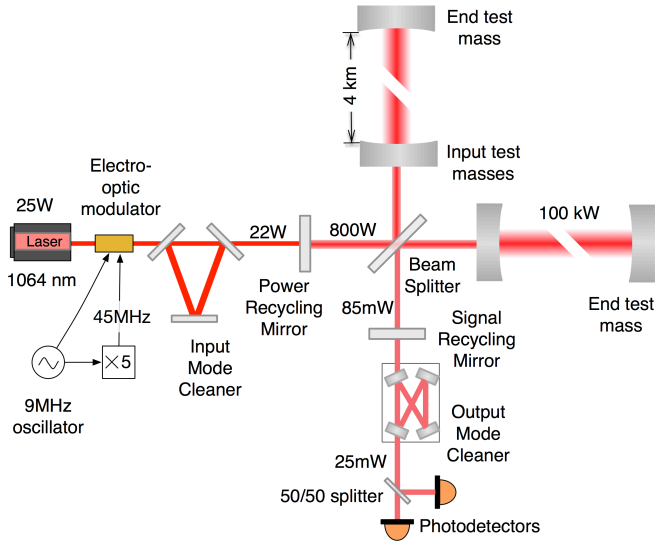


Figure 5. This image is a schematic of the LIGO detectors. As in the simplified version, a laser is still divided by the beam splitter and reflected back to recombine at a detector. However, now there are many optical systems in place to control the beam parameters in order to detect the smallest changes in arm length possible. Refer to the text for details. (taken from www.ligo.org)

One of the most important features is the inclusion of a Fabry Perot cavity in each arm. Originally proposed by Ronald Drever, these are pictured above by the spaces between the two pairs of Input and End Test Masses. Each LIGO arm is physically 4 km in length (the Virgo arms are 3 km long), which, given equations (8) and (9) for the magnitude of strain and the effect that would have on an arm length, would result in length changes on the order of 10^{-18} meters, or $1{,}000^{th}$ the width of a proton. The Fabry Perot cavities allow the beams to make many round trips inside their space before exiting again to recombine back at the beam splitter. This results in an effective length for the arms of 1,120 km and thus boosts the signal by a factor of ~300.

Another important component in the gravitational wave detectors, also introduced by Ronald Drever, is the power recycling mirror. The effect of the power recycling mirror is to increase the injected laser beam power on the Michelson. By increasing the laser power injected into the Michelson, i.e. the number of photons that impinge on the test masses, we also increase the resolution of the signal. This is because of the phenomenon of shot noise which relates number of photons with the signal to noise ratio by

$$SNR = \frac{N}{\sqrt{N}} \tag{20}$$

where N is the number of photons. The determination of the signal amplitude is a statistical process. The fewer the number of photons sampling the test mass position at a given moment, the less precise will be the length determination.

LIGO's diode laser has a wavelength of 1064 nm and enters the interferometer with a power of up to 200 Watts. Using the expression for the energy of a photon

$$E = \frac{2\pi\hbar c}{\lambda} \tag{21}$$

the photon energy is approximately $2\text{x}10^{-19}$ J. This equates to 10^{21} photons injected each second, which gives a signal to noise ratio value of ~$3\text{x}10^{10}$. The power recycling mirror increases the 200 Watts to an effective power rating of 750kW. This is accomplished by tuning the power recycling cavity length so that photons reflected out of the Fabry Perot formed by the test masses will be sent back into it instead of being lost, thus increasing the power of the laser. The boost from 200 W to 750 kW increases the number of photons per second to ~$4\text{x}10^{24}$, and increases the signal to noise ratio by a factor of approximately 100. The Fabry Perot cavities between the input and end test masses further increase the number to almost 10^{27} photons per second increasing the sensitivity by approximately another factor of 100.

By tuning the Michelson, so that the arm length difference is only very slightly off of resonance, LIGO puts a relatively small fraction of the input laser power (25 mW) out of the recombination plane onto the photo-detectors. The 25-mW signal is further halved by a final beam splitter to provide the optimal power loading on the photo-diodes, without saturation. The Michelson working point is set slightly away from zero power so that the change in signal induced by the Gravitational Waves is mostly linear. The photo-diodes function by producing electron hole pairs when a photon is absorbed on their surface. A voltage bias is applied to collect the signal current without electron-hole recombination. The output voltage from these photo-diodes is what is finally digitized

and transduced into a graph of the amplitude of the strain caused by a gravitational wave over time.

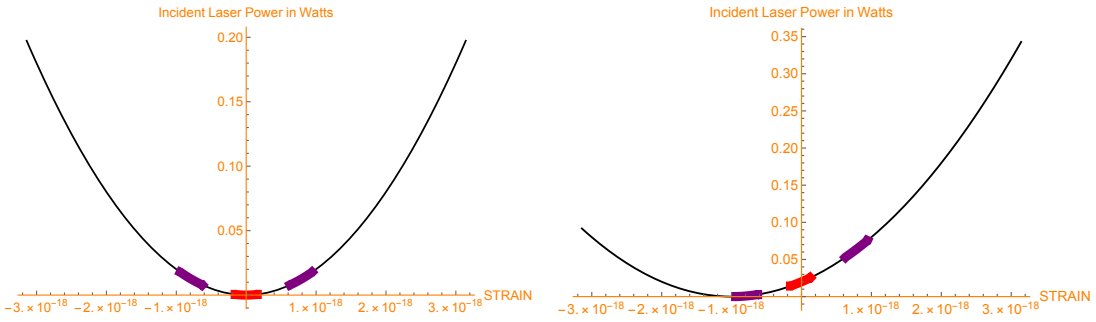


Figure 6. These plots illustrate the detected laser power due to strain induced in the beam path lengths show. On the left, the interferometer is locked in an arm length configuration (the red band) where no power is incident if there is no length change. Both increasing and decreasing the cavity lengths will produce output power on the photodiodes. This makes it impossible to determine the direction of the sign of the length change. However, by locking in a state where there is some laser power incident on the photodetectors at the working point (red band is now around 20 mW), then the sign of the arm length change may be seen.

The input and output mode cleaning optical systems utilize high finesse cavities to filter out laser spatial modes introduced by mirror defects that would bring phase noise.

Once the signal is created and on its way to be delivered to the output port it will have developed higher order modes due to the fact that the test masses are not perfectly spherical mirrors. These modes are then filtered out by the output mode cleaning cavity.

Finesse is a measure of the bandwidth of frequencies that will resonate in an optical cavity. High finesse cavities have a narrow bandwidth and require to be tuned to their own resonant length with high precision. The electro-optic modulator at the input of the interferometer is used to modulate the laser with side bands matching the particular resonant frequencies of the various cavities. By monitoring the amplitude of these side

bands, feed-back controls are used to keep the cavities at the desired resonant conditions with electrostatic and electromagnetic actuators.

2.2 Detections of Gravitational Waves by LIGO and Virgo

On September 14th, 2015, LIGO made the first detection of gravitational waves in history (B. P. Abbott *et al,* 2017 First Detection Paper). The two LIGO observatories were able to extract a signal from a binary Black Hole merger at a distance of 1.4 billion light years from Earth. At the beginning of the detected signal, one Black Hole of approximately 36 solar masses orbited another of about 29, with a rotational frequency of ~35Hz. The Black Holes continued to spiral inwards as more and more energy was radiated in the form of gravitational waves. Their rotational frequency increased to ~250Hz before they finally coalesced into one Black Hole with a total mass of about 62 solar masses. The difference between the sum of the original two Black Holes and the final mass was converted into a very large amount of Gravitational Wave energy in the signal pictured below. The resulting Black Hole then proceeded to "ring-down" like a struck bell in what should theoretically be a superposition of spherical modes. All of the information was extracted from the signal below.

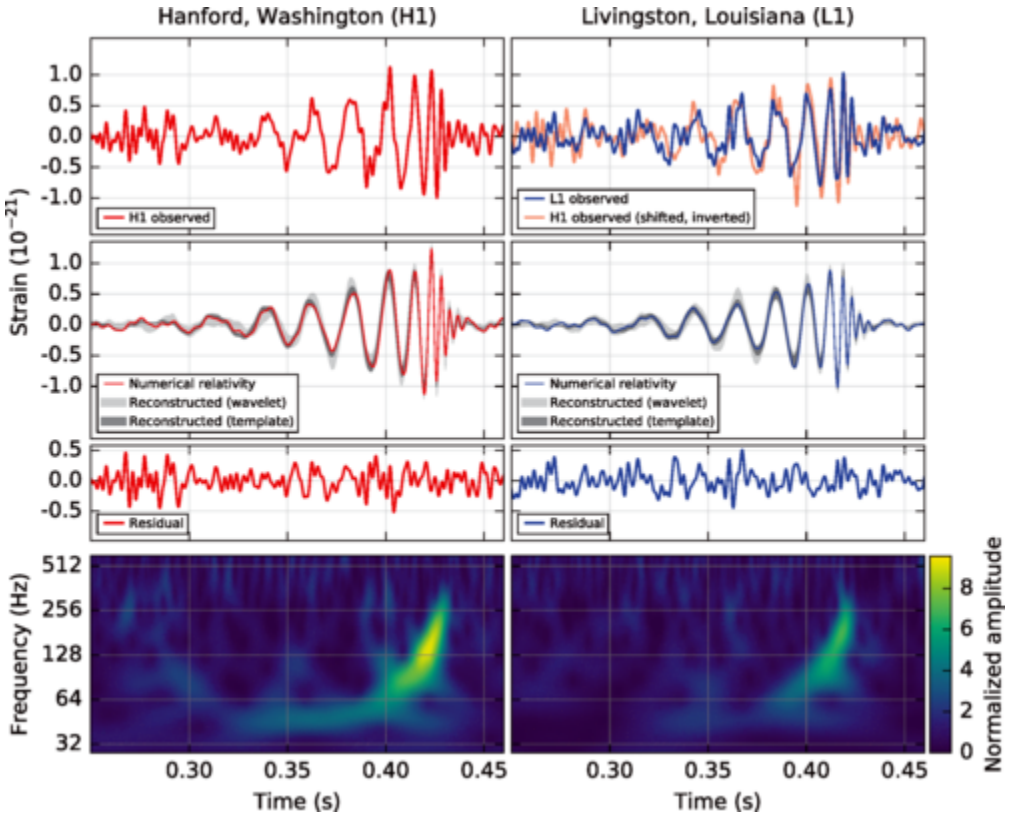


Figure 7. From top to bottom, the two strains in space-time transduced into a signal from the length changes in the LIGO observatories, the signal extracted from the noise by fitting the data to a numerical solution for this specific gravitational wave event, the residual noise after fitted signal subtraction, and finally a frequency versus time plot that illustrates information about the amplitude of the wave as it progresses from low to high frequency. The Livingston data has been shifted to compensate for the amount of time it took for the wave to travel from one detector to the other and inverted to account for differences in the orientation of the two detectors with respect to the wave polarization. (B.P. Abbott et al, 2017 First Detection Paper)

From figure 7, we can see that the level of strain in the residual noise is NOT negligible when compared to the extracted signal's amplitude. At the beginning of the inspiral and during the ring-down (the exponential like decay after the peak amplitude), the noise actually becomes greater than the signal. The signal to noise ratio is only high enough for detection because the signal closely matches the signal foreseen by general relativity. If the signal had come from a smaller or more distant source it may not have been detected at all. The limited SNR limits our ability to precisely determine the parameters of the general relativity calculations (the two masses, their spins and orbital

orientation), which are the quantities of astrophysical interest. For example, there is a lot of information to be gleaned by observing any modulation in the waves. Modulation of the wave-form would tell us about the spins of the black holes on their own axes as well as their precession. Information on this scale is lost in the noise when the SNR is as low as that pictured above. Also lost are the subtle nuances of the ring-down behavior (higher mode excitations of the Black Hole's bell-like behavior) which could potentially hold a tremendous amount of information about the final state of the Black Hole, and how it radiates energy.

Since the first detection, there have been five other gravitational wave observations made by LIGO and Virgo, including a binary Neutron Star merger. The binary Neutron Star merger detection may be the most dramatic illustration of the impact of gravitational wave observation on astronomy, physics and understanding the universe in general. First, it was successfully shown that three interferometers can triangulate the location of a gravitational wave source with sufficient accuracy to allow pointed optical and radio telescopes to detect the source. In this detection, the pointing process was peculiar. The LIGO detectors were able to narrow the location of the event to a thin swath of the sky. Then, since Virgo did not see the event at the same time, crucial information was extracted about the true direction of the gravitational wave's propagation vector. The signal had to come from a direction that was within Virgo's blind spot. Eventually, with the knowledge of the signal shape, a weak signal could be extracted from the Virgo noise, with timing confirming that the source was near the blind spot. The observation was sufficient to alert astronomers in the electromagnetic spectrum of observation, and to motivate them to point their telescopes at an area of the sky of

approximately 28 square degrees in size (B. P. Abbott *et al,* 2017 Binary Neutron Star Paper). Within hours, the electromagnetic observations confirmed an intense event had just occurred at this location. Concurrently, the Fermi satellite detected a burst of gamma rays starting just 2 seconds after the end of the BNS inspiral, coming from roughly the same direction. The optical telescopes determined the presence of a kilonova with an emission spectrum corresponding to the thermal emission from heavy elements.

This was the first time "multi-messenger astronomy" had been employed with Gravitational Waves. Multi-messenger astronomy means recording an event using different physical information delivery systems (multiple electromagnetic signals and Gravitational Waves) at the same time. This observation validated a prediction from researches in the field of high energy particle physics the postulates that the formation of the heavier elements in our universe may happen in these mergers through a sequence of r-process neutron capturing events. It was initially believed that this synthesis occurred in the shockwave of supernova explosions, but then calculations had shown that there is not enough time nor neutron density in the Supernova shockwaves for r-processes to climb all the way up the Periodic Table from Iron to Uranium.

The amount of noise in the detectors limits the amount of information that can be extracted. For example, and important question that will be answered with better SNR is, "what is the actual diameter of a neutron star?". It is therefore of paramount interest to increase the SNR in GW detectors to increase the quality of science that can be performed, as well as to increase the detection depth inside the Universe and, therefore, the rate of detection.

2.3 Characterizing Strain Due to Noise in a GW Detector

A gravitational wave incident on the detector will induce a change in length of the space between the test masses in the arms. Yet, other physical factors could also cause the effective space between the test mass surfaces to change and these will induce a signal that is not differentiable from the one induced by a strain in space-time. This is a fundamental component of the noise in the Gravitational Wave detection.

A gravitational wave that is created by a source of inspiraling masses will grow in amplitude and in frequency as the masses draw nearer to one another. It is necessary to compare the true space-time strain due to a Gravitational Wave (h) with the strain noise (h_n) induced at the various frequencies of detection. A detector is experiencing many sources of noise, and even when there are neither Gravitational Waves, nor transient noise events, white noise is present at the signal port.

Gravitational Waves from an inspiral event will have an expected characteristic form that is given by numerical solutions to the linearized space-time field equations, the amplitude of these being a time changing strain. Because this signal is expected to be somewhat periodic, the amount of strain induced by the wave at various frequencies may be found by performing the equivalent of a Fourier transform of the expected signal. A bank of pre-calculated signals (templates) is continuously compared with the output signal and the corresponding chi-square is calculated. This is considered the optimal extraction method.

The detector output is continuously measured by performing the Fourier transform to obtain an expression for strain noise as a function of frequency. The

function of the squares of amplitudes is defined as the Power Spectral Density (PSD) of the noise.

$$S_n(f) = \lim_{T\to\infty} \frac{1}{T}\left[\int_0^T h_n(t)e^{-i2\pi ft}dt\right]^2 \tag{22}$$

This expression can be understood as a representation of random power in each frequency bin if one imagines monitoring the displacement in space over time of a simple lossless harmonic oscillator. In that case, the observed quantity would be

$$x(t) = A\ Cos[2\pi f\ t] \tag{23}$$

The truncated Fourier transform of this measurement over a finite, but long, time T would be

$$x(f) = \int_0^T x(t)e^{-i2\pi ft}dt \tag{24}$$

where the amplitude, being real, is the amplitude of the transform. The square of (24) would then be, apart from some constant, the energy of the oscillation at that frequency. Averaging the measurement over the time T then turns this into an expression of power.

The PSD of the noise in gravitational wave detection is, by convention (C. J. Moore et al, 2014), defined as

$$S_n(f) = \frac{[h_n(f)]^2}{f} \tag{25}$$

This is the mean square amplitude of the amount of strain induced by noise that is detected at each frequency over the frequency of the signal. Note that this value goes to infinity as the frequencies become lower. The square root of (25) is the amplitude of the strain induced by noise and it has units of $\sqrt{Hz}^{-1}$. A similar expression to (22) can be written for the signal's PSD.

$$S_s(f) = \frac{4\left|\tilde{h}(f)\right|^2}{f} \tag{26}$$

where $\left|\tilde{h}(f)\right|^2$ is the square of the Fourier transform of the actual gravitational wave induced strain with no noise and is related to the calculated characteristic strain, h_c that would be induced by a wave from an inspiraling source by

$$\left|\tilde{h}(f)\right|^2 = \frac{[h_c(f)]^2}{4f^2} \tag{27}$$

With these definitions, the square of the SNR ρ can be written as

$$\rho^2 = \int_0^\infty df \frac{4\left|\tilde{h}(f)\right|^2}{S_n(f)} \tag{28}$$

which just instructs us to integrate the ratio of the squares of the Fourier transforms of the strains from both signal and noise over all positive frequencies. Then, using integration by parts, we can rewrite (28) in the form

$$\rho^2 = \int_0^\infty d\,(\log f)\left[\frac{h_s(f)}{h_n(f)}\right]^2 \tag{29}$$

which enables a log-log plot of curves for the strains due to signal and noise to provide a direct relationship to the SNR. For example, if the signal strain and the noise strain were of the same amplitude at some frequency then the differences between the heights of their curves on a strain versus frequency plot would be zero at that point.
Since log (1) = 0, we get the SNR of 1. If the signal were 10 times the amplitude of the noise then the SNR would be 10 and the spacing between the curves would be 1 unit of the log of the strain axis.

These conventions are used by the gravitational wave detection community to display information about gravitational wave detection amplitudes and sources of noise.

2.4 Sources of Noise

The total noise budget for LIGO is a sum of all of the noise sources. The plot of strain (log [$\sqrt{S_n\,(f)}$])against the log of the frequency is shown below.

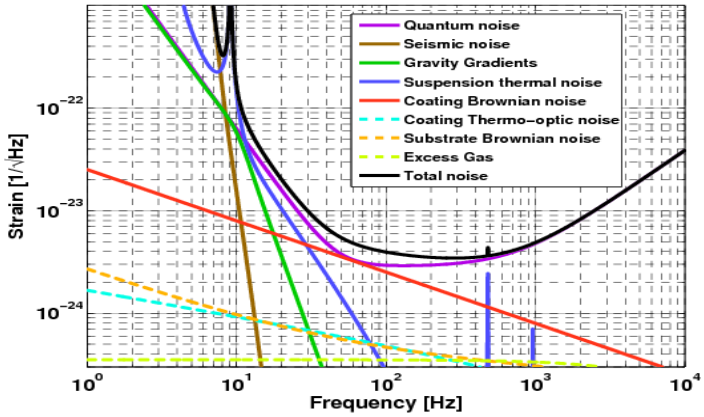


Figure 8. This plot, taken from www.ligo.org, shows all of the physical sources that induce a noise strain in the detection frequency band of the Gravitational Wave detector.

Seismic Noise

Low frequency seismic disturbances such as earthquakes, tidal motion in the Earth's structure, and even trucks passing near the detector will cause the mechanical optics within LIGO to move. This motion will move the test masses and change the overall phase of the detector. This is the called the Seismic noise, and is represented by the brown curve in the Figure 8. To isolate the test masses from external sources of vibration they are suspended from a series of pendulums, and at the bottom by strong fused silica fibers. These pendulum systems very effectively isolate the test masses from all mechanical noise above a threshold frequency, which is why the curve for Seismic noise drops very quickly at around 10 Hz. This noise can theoretically be reduced arbitrarily.

Suspension Thermal Noise

There are processes that cause fundamental noise limits; mechanical losses in the material of the fibers that are suspending the test masses interact with the thermal bath and cause random mechanical fluctuations to be transferred down to the test masses. This is the suspension thermal noise illustrated by the blue curve in figure 8.

The spikes on the blue curve at around 400 and 1000 Hz represent the "violin modes", or the recoil of the test mass against the natural resonant frequencies of the suspension fibers. They get excited in different ways and, unless damped, they cause an inertial reaction on the mirrors.

Newtonian or Gravity Gradient Noise

The green curve, is the Newtonian noise, or "gravity gradient", and shows the amount of noise that is injected due to fluctuations in the gravitational field surrounding the detector. Were the Earth a static spherical mass with no seismic activity there would be no change in the gravity gradient. However, the "solid" material of the Earth is continually subject to micro-seismic activity, whose pressure and shear waves continuously change the density of rock in front and behind the test masses, thus shaking them with a gravitational "force". There are many sources that excite micro-seismic activity of the Earth's crust. The rocky crust floating on molten magma responds to tidal forces with a much greater magnitude than even the oceans on its surface with a continuous change in shape causing the rock to creak. Distant earthquakes will cause this as well. Surf hitting the coasts cause continuous continental recoil, which depends on storm activity, and usually cause the largest component of micro-seismic activity. Continental drift, volcanic activity, storms buffeting mountains and even human

activities, all contribute to micro-seismic activity. Because of this, at the microscopic level the density distribution of the Earth is in constant flux and this change can be detected by an instrument as sensitive as LIGO. This seemingly random gravity noise is indistinguishable from gravitational wave signals. Even the lifting and setting down of a person's leg while walking (Thorne and Winstein, 1998) will distort the gravity gradient if it is done near enough to the detector. To be clear, this is not seismic noise due to the person's walking infiltrating the seismic attenuation filters and "shaking" the detector but actually is a distortion of the local gravitational field itself. This may be one of the greatest examples of just how sensitive the current generation of gravitational wave detectors have become.

Excess Gas Noise

The arms of the detector are housed in tubes that have been evacuated down to the 10^{-9} Torr regime, however there is metal outgassing and not all of the gas can be removed fast enough. The fluctuations of the residual gas cause fluctuations of the residual refraction index inside the pipe and, as a result, in the laser beam propagation. This source of noise is represented by the dashed yellow-green curve and it is quite low as well as being flat across all frequencies.

Coating Thermo-Optic Noise

The dashed blue curve is due to effects that occur when large laser power is incident on the optical coatings of the test masses. When the beam is incident on the coatings there will be thermal fluctuations, which will create a frequency dependent volume around and within the coatings where the indices of refraction fluctuate. This

will, in turn, induce random fluctuations in the phase of the beam as it interacts with these regions.

Finally, we are left with the two fundamental limiting sources of noise in gravitational wave detectors. These are represented in figure 8 by the purple curve (Quantum Noise), and the red curve (Coating Brownian Noise).

Quantum Noise

Quantum Noise is a direct consequence of Heisenberg's Uncertainty Principle. When using a photon to measure the test mass position there will be inherent uncertainties in its position and momentum with the relation between the two given by the familiar

$$\Delta x \, \Delta p \geq \frac{\hbar}{2} \tag{30}$$

In practice, with one photon, one can only have the precision of ¼ wavelength, i.e. ~ ¼ 10^{-6} m, which is grossly insufficient. There is an approximately 10^{12} deficiency in the 10^{-18} m precision needed to make strain detections at 100 Hz. Due to the statistical nature of the process, the length determination improves only with the square root of the number of photons is used. Therefore, to reach the required precision at 100 Hz, one needs to interrogate the mirror position with a number of photons of the order of $(10^{12})^2$ every 10 ms which adds up to about one Mega Watt of standing laser power on the mirror. If the test masses' positions are measured with the required precision then (30) says that there will be a limit on the certainty in the momentum of the test masses. The number of photons available within the period of a given frequency bin decreases like 1/f. At high frequencies, the achievable precision will decrease as $f^{1/2}$. This precision can be improved only by increasing the stored power. At low frequencies though, the

unavoidable $\sqrt{N}$ fluctuations in the number of photons stored in the Fabry Perot cavities cause fluctuations of radiation pressure that, in their own turn, would cause the test masses to move and destroy the precision of the measurement. In this case, increasing the stored power worsens the precision. Increasing the power of the laser decreases the shot noise because the test mass location measurements are averaged over more photons, but then the test masses are pushed by radiation pressure with a broad spectrum of momenta It is not a paradox, just the familiar limitation that Quantum Mechanics places on observation of photons applied on the 40 kg test masses.

Two tricks may be played to optimize the shape of the Quantum Noise curve so that its lowest value is in the ideal detection frequency band. Basically, the separation between the shot noise slope in the high frequency band and the radiation pressure slope in the low frequencies increases if the weight of the test masses is also increased. On the quantum side, "squeezed light" is introduced into the detector. This involves manipulating the phase diagram required by (30). At high frequency, one needs to intentionally widen the Δp component so that the Δx can be reduced, or "squeezed". This has been experimentally achieved. But this is counterproductive at low frequency where the Δx component should be expanded so that Δp can be squeezed. It seems the equivalent of the shot-noise vs. radiation-pressure conundrum but in reverse with respect to frequency dependence. However, the ellipse generated by a squeezed phase diagram of (30) can be rotated as a function of frequency so that, at desired frequencies, the shot noise and the radiation pressure can both effectively be reduced at the same time

The key information as far as this paper is concerned is that there is freedom to shape the Quantum Noise curve to match the Coating Brownian noise curve at one

frequency, and that the Coating Noise is the final fundamental limiting noise source in detecting gravitational waves.

Coating Brownian Noise

Coating Brownian Noise is the noise injected into the detector due to the shape fluctuations induced in the test masses by statistical fluctuations of temperature at thermal equilibrium. These fluctuations exhibit themselves as the microscopic mechanical fluctuations in the mirror surfaces. These random deviations away from flatness are locally large, but averaged over the many atoms on the mirror surface by the incident laser beam interrogating the mass position to give overall phase (length) fluctuations in the Gravitational Wave signal. More detail of this noise source is given in chapter 3.

2.5 The LIGO Sensitivity Standard

Most Gravitational Wave signals sweep across the sensitivity frequency range determined by the noise sources listed above. Detection is achieved when the significance of the signal is detected, integrated over its entire duration, and is eight σ above the noise level of the detector. All neutron stars form with more or less equal mass of about 1.4 solar masses. The standard by which LIGO's sensitivity is measured is the distance at which a binary neutron star (BNS) merger can be detected. The importance of the correlation between lowering the Coating Brownian Noise curve and the increase in BNS detection range is illustrated in the table (Miller et al, 2015 APS) below.

	Quantum	Coating Thermal	Mirror Mass	Suspension Thermal	BNS Range Mpc	BBH Range Gpc
1					220	1.3
2	X				280	1.5
3		X			280	1.7
4			X		260	1.6
5				X	220	1.3
6	X	X			400	2.3
7	X		X		320	1.9
8	X			X	280	1.6
9		X	X		350	2.3
10		X		X	280	1.7
11			X	X	270	1.7
12	X	X	X		470	2.9
13	X	X		X	410	2.3
14	X		X	X	320	1.9
15		X	X	X	350	2.3
16	X	X	X	X	480	3.0

Table 1. The range of a detectable BNS merger and BBH (Binary Black Hole) merger is given when certain parameters of the detector are altered. An X in the first column represents injecting squeezed noise into the detector, one in the second column represents a decrease in the coating noise by a factor of two, the third column would represent increasing the mirror masses by a factor of two to offset radiation pressure effects, and an X in the fourth column represents decreasing the suspension thermal noise by a factor of two.

In line 1, we see the current BNS detection range for LIGO is approximately 220 Mpc. If (line 3) only the Coating Brownian Noise were lowered by a factor of 2, and if nothing else were done to optimize the detector's other noise sources, there would still be a gain in radial detection distance of ~60 Mpc. Since the Quantum Noise (line 6) is brought down to match the Coating Noise curve, improvement there would be a range gain of 180 Mpc.

As will be shown in this paper, there are physical limits to the decrease of detector noise brought by the improvement of the coating noise, which are brought about by the properties of the fused silica substrate of the coatings. A factor of 2 improvement is not obtained by simply addressing the coatings. However, the key takeaway from table 1 is that by addressing the problem of the Brownian motion in the optical coatings that give the test masses their reflectivity, we can directly improve a number of important detector features:

- The detection range of the detectors
- The resolution of the observed gravitational wave forms
- The rate at which detections are made

In fact, since detection rate is a function of the volume of space from which detections can be extracted, an increase in range by a factor of 2 increase in sensitivity essentially equates to an increase in the number of detected signals in any given detector operation run by a factor of 8.

CHAPTER 3

Coating Brownian Noise

3.1 The Fluctuation Dissipation Theorem and Brownian Motion

A fluid, kept at a constant temperature and pressure will, from a macroscopic point of view, appear to be in thermal equilibrium. That is, measured as a closed system the fluid will not lose or absorb any quantifiable amount of energy. However, if we were to zoom in to a microscopic view of the fluid at temperature T, and if we were to insert some very small and low mass test particles within it (like grains of pollen), we would observe that these test particles are jostled about in frenetic and completely random motion, with a random distribution of kinetic energy fluctuating around the value of $k_B T$. A system that appeared to be in thermal equilibrium on a macroscopic level is actually constantly struggling to achieve true equilibrium by distributing its total internal energy evenly to all the possible internal degrees of freedom. However, as long as the tiny test masses are in contact with the fluid, or thermal bath, there will be an interaction that keeps the system from ever fully coming to rest. Observation of this phenomenon was first recorded by Robert Brown in 1827 and is thus called Brownian Motion. The model of the physical mechanism which underlies the interaction between the grains and the fluid in Brownian motion was first devised by Albert Einstein. This fundamental idea formed the foundation from which the Fluctuation Dissipation Theorem (FDT) was later devised by Harry Nyquist in 1928. The "Fluctuation" referring to the random force exerted on the test masses by the fluid, and the "Dissipation" referring to the loss of mechanical energy into heat by a friction-like response of the mass in the fluid. The reflective coatings on the test masses of LIGO can be described as elastically bound

grains in a fluid consisting of a thermal bath of phonons. The FDT is therefore a logical model to explain the noise that will be injected into the gravitational wave detectors due to the thermal-fluctuation induced motion of the coating's surface.

Using the observations of Brownian motion as a starting point, we can begin to create a physical model that will eventually lead to the FDT (Reif, 1965). The grains in the fluid are moving randomly and so there must be a random force acting on them. Confining the model to one dimension, we have

$$m\,\frac{dv}{dt} = \mathcal{F}(t) + F(t) \tag{31}$$

where m is the mass of the test particle in the thermal bath, v is its velocity through the bath, $\mathcal{F}(t)$ are any external forces on the mass (gravity, electric field, elastic restoring force etc.) and $F(t)$ is the mysterious fluctuating "force" causing the observed random jiggling. We can imagine that the fluctuating force is a series of spikes over time that rise and decay over some relatively similar time scale, τ^*.

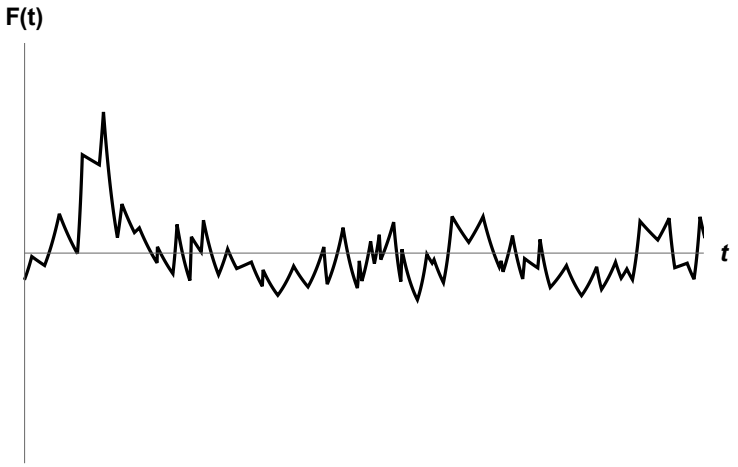


Figure 9. A graph of some external fluctuating force to show how the time for the force to decay is relatively the same from peak to peak. This can be considered the "correlation time" τ^*, of the force.

The time, τ^* is very small on a macroscopic scale. We then define a time, τ that is much larger than the correlation time so that we can experience many peaks and troughs of the

fluctuating force, yet still small enough on a macroscopic scale so that we can use it as an infinitesimal time with which to perform a derivative. Now, (31) can be rewritten as,

$$m[\, v(t+\tau) - v(t)] = \mathcal{F}(t)\tau + \int_t^{t+\tau} F(t')dt' \tag{32}$$

It has been assumed that any external force, $\mathcal{F}(t)$ is varying much more slowly over time than the fluctuating force and so it is essentially constant. The fluctuating force is as likely to be negative as to be positive during the time τ and undergoes many ups and downs in that time, for very long τ this integral could be expected to converge to zero. However, if we did that, we would be left with nothing beyond the applied external forces to explain the motion on the left-hand side of (32), and there would be no mechanism left to explain random motion or for driving the system towards equilibrium if it were ever externally perturbed away from it. Since the fluctuating force arises from the thermodynamic pursuit of the system to reach equilibrium, it must have some "restoring force" attribute that we need to take into account. This motivates us to write the fluctuating force as a pair of two terms

$$F = \bar{F} + F' \tag{33}$$

where $\bar{F}$, a function of the average velocity of the particle, is zero when the particle is not moving, and may grow in response to motion (but not too quickly as to enlarge the integral in (32) by much). This type of behavior implies that $\bar{F}$ is a linear function. And, since it should restore the particle to an equilibrated velocity, it can be written as

$$\bar{F} = -\alpha v \tag{34}$$

This is what is known as the linear response function. Since it is a function of the velocity, and negative, it acts as a viscous dissipation force and is responsible for the dissipation of energy in the system. The other part of (33), F' is the rapidly fluctuating

aspect of the total force, and *its* integral over a large time may indeed go to zero. We then rewrite (31), leaving out the applied force term, $\mathcal{F}(t)$ for simplification.

$$m\,\frac{dv}{dt} = -\alpha v + F'(t) \tag{35}$$

We can then play a mathematical trick, and multiply both sides by x to get

$$m\,x\frac{d\dot{x}}{dt} = m\left[\frac{d}{dt}(x\dot{x}) - \dot{x}^2\right] = -\alpha x\dot{x} + xF'(t) \tag{36}$$

where the product rule was used to obtain the middle expression. The next step is a critical one, and is at the heart of FDT. We understand, from equilibrium thermodynamics that the total energy in a system is distributed equally to all degrees of freedom in an amount $\frac{k_B T}{2}$, so we make the physical realization that the energy of the one-dimensional translational motion in (36) must have this value. So, the leap that must be made here is in understanding that while the system appears to be in equilibrium at the macroscopic level, and is found to not be in equilibrium on the microscopic level, it is still operating with the principles of a thermodynamic system at equilibrium when we examine single particle interactions. With this assumption, we can write the average of (36) as

$$m\,\frac{d}{dt}\langle x\dot{x}\rangle = k_B T - \alpha\langle x\dot{x}\rangle + \langle x\rangle\langle F'\rangle \tag{37}$$

where the last term goes to zero from the explanation about the integral in (32). We are left with

$$m\,\frac{d}{dt}\langle x\dot{x}\rangle = k_B T - \alpha\langle x\dot{x}\rangle \tag{38}$$

and then using the identity

$$\langle x\dot{x}\rangle = \frac{1}{2}\frac{d\langle x^2\rangle}{dt} \tag{39}$$

we get an expression for the mean square amplitude of the deviation of the position of the particle away from where it started.

$$\langle x^2 \rangle = \frac{2k_B T}{\alpha}\left[t - \frac{m}{\alpha}\left(1 - \exp\left[-\frac{\alpha\, t}{m}\right]\right)\right] \tag{40}$$

which for very short time scales may be written as

$$\langle x^2 \rangle = \frac{k_B T}{m} t^2 \tag{41}$$

and for long time scales as

$$\langle x^2 \rangle = \frac{2k_B T}{\alpha} t \tag{42}$$

The result in (42) shows that, a particle exposed to a thermal bath, and untethered by any applied forces, will wander away from its initial position in a manner similar to a "random walk". If the particle were constrained by a restoring spring-like force, since (42) is the square of the displacement away from equilibrium which does not depend on the direction, this would still be an expression of how much energy is dispersed by the particle into the thermal bath.

Following the method laid out in 2.3 and applying the Fourier transform to (42) yields an expression of the thermal fluctuation's spectral density,

$$x^2(\omega) = \frac{4k_B T}{\alpha \omega^2} \tag{43}$$

where we recall that the variable, α originally entered the derivation as a friction coefficient. It must, therefore, be some value that expresses how much the mass allows interactions with the thermal bath. It can be shown (Callen and Greene, 1952) that α is the real part of the complex mechanical admittance, $Y(f)$

$$S_x(f) = \frac{k_B T}{\pi^2 f^2} Re\{Y(f)\} \tag{44}$$

which can be expanded (Harry et al, 2008) as

$$Re\{Y(f)\} = \frac{4\pi\, f\, U(f)}{F^2}\phi \tag{45}$$

where, f is the frequency in question, $U(f)$ is the total elastic energy stored in the mass, F is a cyclic pressure distribution applied to the test mass at the frequency f, and ϕ is the test mass material's loss angle. This last component is an expression of how susceptible a material is to interactions with the thermal bath, and is precisely the parameter that we will want to optimize in order to reduce the thermally induced Coating Brownian Noise.

3.2 Mechanical Quality Factor

An ideal harmonic oscillator continuously transfers potential energy into kinetic energy with no losses. However, a real system will lose energy due to many factors. For example, a mass and rod pendulum that is mechanically connected to a pivot point, will lose energy as it oscillates due to collisions with the air as well as from friction around the pivot point. The pendulum will then damp down to a state that appears, at least macroscopically, to be completely quiescent; in reality, it is only in thermal equilibrium. As was shown above in section 3.1, the thermal bath surrounding the pendulum will interact with the material's many internal degrees of freedom through an energy exchange. The Fluctuation Dissipation Theorem, outlined above, shows that some of this energy will be dissipated and that that dissipation is related to the quantity ϕ, the Loss Angle of the material. The oscillator never reaches a state of true equilibrium, and suffers constant fluctuations that cause the system to mechanically "jiggle" microscopically.

A simple, one dimensional harmonic oscillator has two degrees of freedom that can each store $\frac{k_B T}{2}$, of energy, and so the total energy made available to the oscillator from the thermal bath is $k_B T$.

Qualitative Explanation of the Fluctuating Force Causing Thermal Noise

The amount of energy that is dissipated at each instant by an oscillator is related to the instantaneously stored energy by the friction coefficient, α the same in the linear response term in (35). As shown in (43) through (45) this term has the parameter ϕ embedded within it.

As a consequence, the amount of energy dissipated by the oscillator within one full cycle of oscillation is roughly given by this relation

$$W_{Dispersed} \sim \frac{k_B T\, f}{Q} \tag{46.1}$$

where $W_{Dispersed}$ is the power instantaneously dumped into the thermal bath and Q is the mechanical Quality Factor of the material related to the Loss Angle by

$$Q = \frac{1}{\phi} \tag{47}$$

The Q of a resonant system is a dimensionless quantity that is defined as the ratio of how much energy is stored over how much energy is dissipated per cycle of oscillation.

$$Q \equiv \frac{E_{Stored}}{\Delta E_{PerCycle}} \tag{48}$$

This value (48) can be measured by counting the number of oscillations that occur in the time it takes for an oscillator to damp down to 1/e of its initial amplitude. A material with a very high Q will oscillate many times before its amplitude decreases by that factor.

The key point of (46) is that, in average, at thermal equilibrium there should be no net exchange of energy, therefore the power dissipated by the oscillator into the thermal bath must be equal to the power returned by the thermal bath to the oscillator, therefore

$$W_{Dispersed} \sim \frac{k_B T f}{Q} \sim W_{FromThermalBath} \tag{46.2}$$

The energy returned by the thermal bath $W_{FromThermalBath}$ is obviously completely random and represents the source of the random force of (36).

The amplitude of the random force that causes fluctuations in an oscillator is a property of the material's dissipation, not of the shape and mass of the system that produces a resonance. Therefore, the random force causing thermal motion remains effective at all frequencies, even out of resonance.

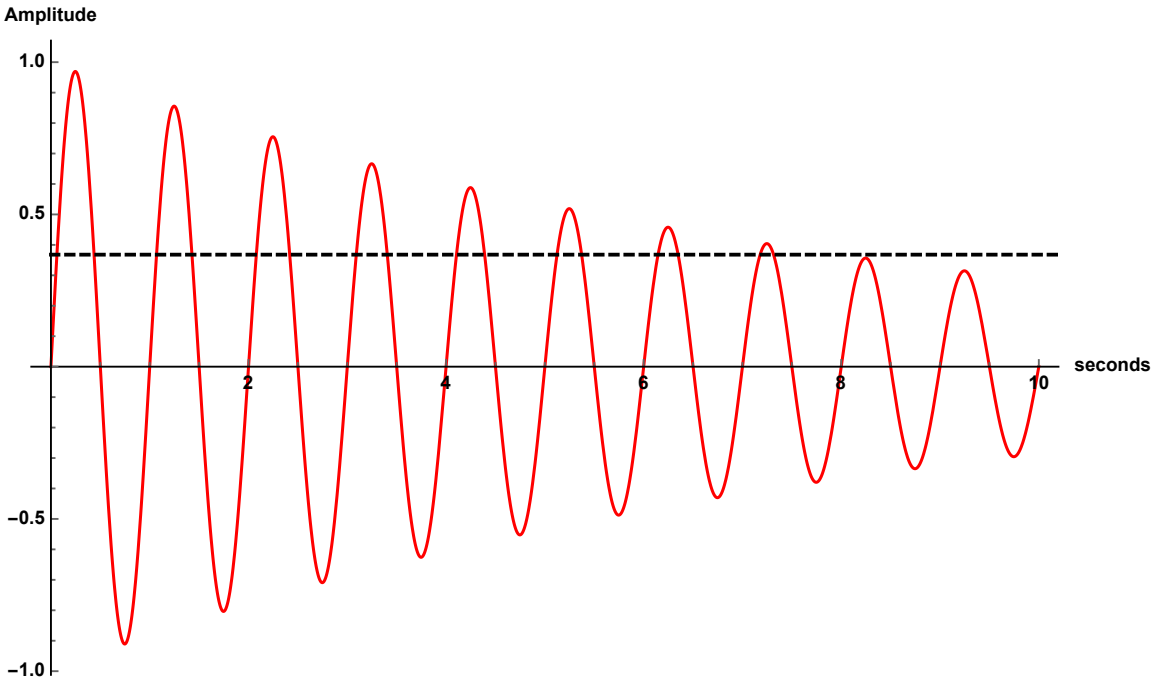


Figure 10. This is the plot of the amplitude of a system that is damping down as it oscillates at 1Hz. It makes approximately 8 cycles before damping to 1/e of its initial amplitude (the black line) in 8 seconds. This system possesses a very low Q Factor of ~8.

From this discussion, we see that materials with large Q or, equivalently, low ϕ will dissipate less energy than materials with larger ϕ i.e. will suffer less mechanical losses and smaller random forces. In a mirror, mechanical losses show up as fluctuations

in the shape of the reflecting surface. If that mirror is being used as the surface of a test mass in a highly sensitive interferometric Gravitational Wave detector, those fluctuations will inject length noise indistinguishable from the gravitational wave signal. More detail will be given on this in the next few sections.

Resonance Width and Amplitude

Materials with very low Q will damp down quickly. A bell made of rubber, once struck, would almost immediately cease resonating with large amplitudes, yet from (46) a microscopic view of the bell's surface would show it constantly fluctuating at very low amplitudes in a linear superposition of the bell's many possible modes. On the other hand, a bell with the same resonant frequency, made of very fine crystal will ring for a long time before damping down. This material has a large Q, and will then be much more stable at equilibrium. This leads us to another definition of the Quality factor, that it is the bandwidth around the resonant frequencies of the system

$$Q \equiv \frac{f_{Res}}{\Delta f} \tag{49}$$

This expresses the Q as a parameter of the material that gives the range of frequencies that can be used to excite it into resonance. A system with low Q has a wide bandwidth around its resonant frequencies and so may be excited into resonance by a wide range of frequencies. Returning to the images of the rubber and crystal bells, any loudly sung note would excite the rubber bell into vibrating at a low amplitude while the crystal bell would require the voice of a highly trained singer to hit just the right note but could then be excited to such large amplitudes that the material could shatter.

Quality Factor Versus Frequency

It has been observed experimentally that Quality factor is generally not constant vs. frequency. The measurement of a material's Quality factor can be performed only at resonant frequencies, which depend on the system shape and material elastic constant. Many factors can affect the measurement of an oscillator's quality factor, including the ambient pressure, clamping mode, the stress state of the material, as well as the temperature at which the elastic components were made and annealed. In addition, actual oscillators are made of many materials, each with its own quality factor. All of these contributions will affect and potentially degrade the precision of the determination of a given material's quality factor.

The Loss Angle of a material has both a shear and a compression component, generally having different values, affecting the observed oscillation quality factor depending on the details of each resonant mode. Determining the Q of a material is still very much an experimental procedure, and much care must be taken to account for all of the factors, including material choice, shapes and measurement techniques.

Examples of Quality Factor Frequency Dependence

In a measurement of the mechanical Quality factors of Poly-Phenylene Sulfide (PPS), and Poly-Ether-Ether Ketone (PEEK), (Jiang Wu et al, 2016) performed with thin bars clamped at one end, the researchers found that the materials' Quality factors decreased as the frequency of the oscillations increased. These materials also exhibited Quality factor vs frequency curves significantly lower when forced to oscillate at greater amplitudes (figure 11).

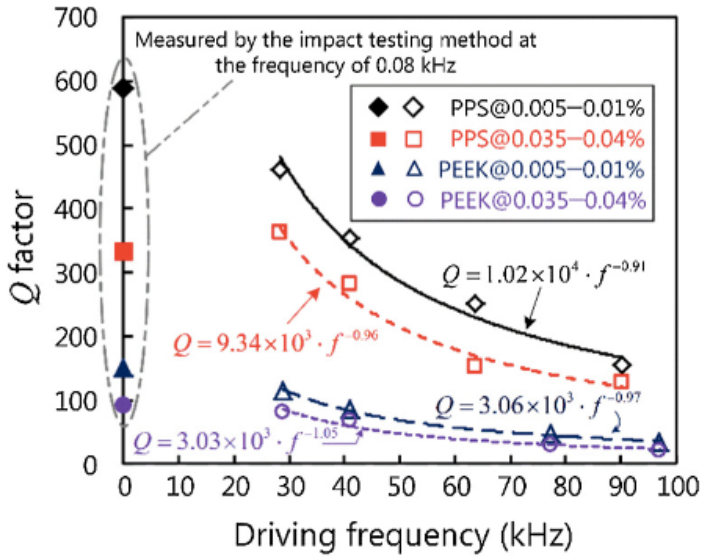


Figure 11. Results of an experiment performed to measure the Quality factor of two different polymers. The two samples were measured at two different driving amplitudes, one inducing a strain of ~0.005 and the other a strain of ~0.035. The Quality factors for the two materials was much lower when forced to larger oscillation amplitudes. We also see the Quality factor falling as a function of frequency, with the approximate slope values near linear regions labeled. Figure is from Jian Wu et al, Ultrasonics 69, 2016.

Measurements of the Quality factor for Maraging Steel, a precipitation-hardened alloy with a very high tensile stress, have shown a wide range of values that appear to depend on the frequency of resonance. The data of table 2 (S. Braccini et al, 2000) shows that the Q increased (Loss Angle, Q^{-1} decreases) with an increase in frequency, a completely different behavior than that exhibited by the polymer measurements.

Specimen	h (μm)	ν_1 (Hz)	Q_1^{-1}	ν_5 (Hz)	Q_5^{-1}	E (N m^{-2})
2	150	440.7	7.7×10^{-4}	5880	1.9×10^{-4}	1.65×10^{11}
3	270	819	2.6×10^{-4}	11 000	6.4×10^{-5}	1.75×10^{11}
4	270	821.2	3.4×10^{-4}	11 030	7.4×10^{-5}	1.76×10^{11}
5	106	445	8.0×10^{-4}	6000	2.0×10^{-4}	1.47×10^{11}
6	160	463	6.1×10^{-4}	6220	2.2×10^{-4}	1.65×10^{11}

Table 2. Data for Q^{-1} (loss angle) measurements of 5 different samples of Maraging Steel, each with different thickness (h).

There may also be complicated relationships between the Quality factor value and the mode shape at the resonant frequency. In measurements of the Q for ~50 nm thick,

1mm by 1mm square Silicon Nitride membranes (Zwickl et al, 2008) the value goes up when the frequency rises with some mode shapes but down when it rises in other shapes.

Mode	$i=1$	$i=2$	$i=3$	$i=4$
$j=1$	$\nu_{1,1}=133\,784$	$\Delta\nu_{1,2}=168$ Hz	301 Hz	247 Hz
	$Q=1.1\times10^6$	1.1×10^6	2.2×10^6	1.5×10^6
$j=2$	−82 Hz	154 Hz	380 Hz	⋯
	1.6×10^6	0.8×10^6	1.8×10^6	⋯
$j=3$	⋯	17 Hz	177 Hz	⋯
	⋯	1.8×10^6	1.9×10^6	⋯
$j=4$	−244 Hz	⋯	⋯	⋯
	1.5×10^6	⋯	⋯	⋯

Table 3. In this table from the measurements of Q for Silicon Nitride membranes held at 293 K it is illustrated that the frequency dependence for the value is complicated and does not always follow a consistently increasing or decreasing trend-line. The first frequency listed, 133 784 Hz, is the actual value measured for that mode. The other values listed are deviations from the calculated frequencies for those modes.

Quality factors are measured using resonances, but to determine the mechanical thermal noise of the mirrors we are interested in knowing the quality factor of all the constituent materials outside resonance. Therefore, we have to measure the quality factors at as many resonant frequencies as possible, identify the quality factors of individual materials, and then interpolate, or extrapolate the measured values to the frequency range of interest. We need to identify candidate coating materials and methods that will have a large Q so as not to make the Q for the entire test mass suffer. The substrates of the test masses are annealed fused silica and possess a very high Q. Large values for Q of ~ $2\text{x}10^8$ have been measured in amorphous materials like annealed Fused Silica (Ageev et al, 2008). Yet analysis is performed in this thesis to show that poor Q factor coatings can significantly affect these values, even if the substrates are much thicker than the coating layers.

3.3 LIGO's Optical Coatings

The test masses within LIGO are mirrors that consist of layers of alternating index of refraction coatings that have been deposited onto cylindrical fused silica substrates.



Figure 12. On the left are pictured two of LIGO's 40 kg test masses before installation. The optical coatings are hidden on the undersides. There are 4 total test masses in LIGO, two input mirrors and two end mirrors, the space between which form the two Fabry Perot cavities of the detector arms. On the right is an image of one of the installed test masses and the optical coating is now visible.
(Credit: Caltech/MIT/LIGO Lab)

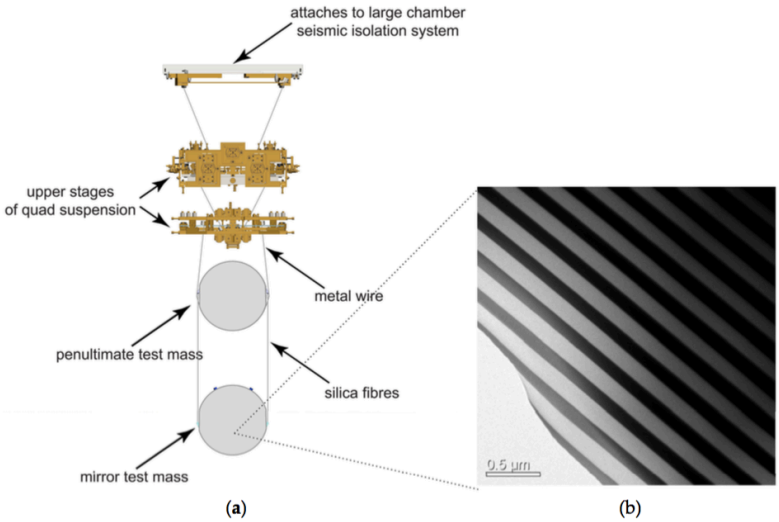


Figure 13. (a) Basic illustration of how the test mass is mounted (b) SEM image of the cross section of an optical coating stack formed by alternating $\lambda/4$ layers of SiO_2 (light bands, low index of refraction) and the TiO_2 doped Ta_2O_5 (dark bands, high index of refraction). (Abernathy, Harry et al 2017)

In common dielectric mirrors, the alternating layers of high and low index of refraction coatings are each $\frac{\lambda}{4n}$ wavelength in thickness, where n is the index of refraction of the material and λ is the wavelength of the laser that LIGO uses to interrogate the test masses. The laser wavelength is 1064 nm, the TiO_2 doped Ta_2O_5 material (figure 13) has an index of refraction of 2.119 when the doping is ~25% Titania (Abernathy, Harry et al 2017) and so the high index layers have a thickness of ~125 nm. The SiO_2 layers have an index of refraction of 1.4585 and so have a thickness closer to 185 nm. LIGO and Virgo use optimized coatings in which each high-low pair has an optical thickness of ½ λ but the high refraction index layers are thinner, to reduce thermal noise. It has been found that the high index layers have significantly lower Q than the low index layers and are the main contributors to the overall loss angle for the stack of coatings. The reflectivity of these stacks of coatings comes from the phenomenon of thin film interference. A propagating photon that encounters a change in index of refraction will incur a partial reflection with a π radian phase shift if the change is to higher refraction index, 0 phase shift if going from high to low. The reflected fields add constructively, and the transmitted fields destructively if the layers are all ¼ wavelength, or if the high-low pair is ½ wavelength. Below is an illustration of the process when multiple layers of $\frac{\lambda}{4n}$ are involved. Transmission of less than 1 ppm can be engineered. Power absorption in the material of less than ¼ ppm can be obtained by using very pure deposition materials. A few ppm of light is scattered on defects, the rest is reflected.

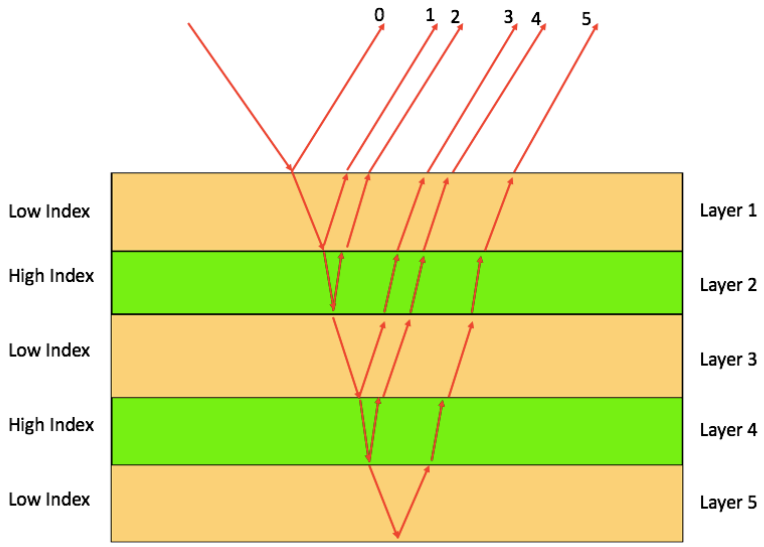


Figure 14. Schematic of thin film interference for many layers of alternating index of refraction materials. In this image light is incident at an angle; in a n interferometer incoming and reflected light is perpendicular to the mirror's surface.

Figure 14 illustrates some possible paths that a photon, incident on the surface of optical coating stacks, may take.

The end test masses in LIGO are cylindrical fused silica substrates that are 20 cm thick, with a radius of 17 cm. The coatings deposited on the substrate have 13 doublets of high and low index of refraction material layers forming a total thickness of ~4 microns, designed for a transmission of few ppm. The input test masses use the same coatings but fewer layers designed for the transmission of ~ 0.1% necessary to obtain the required Fabry Perot finesse.

The Loss Angle for the fused silica substrate has been measured as low as ~10^{-8} while the coatings' mechanical losses are of the order of 10^{-3}, dominated by the high index of refraction material. The best coatings measured (Abernathy, Harry et al, 2017) have (in a frequency independent model) $\phi_{Shear} = (8.3 \pm 1.1) \times 10^{-4}$ and

$\phi_{Bulk} = (6.6 \pm 3.8) \times 10^{-4}$. Even though the coatings comprise a much smaller portion of the overall thickness of the test masses, 4 μm compared to 20 cm, they dominate the overall Loss Angle of the test mass.

Mechanical Losses in Actual Mirrors

What counts in calculating mechanical thermal noise are the mechanical losses of the system in the frequency range of interest.

Using the definition for Quality factor from (48) we can build an idealized multi component system model, useful to find an order of magnitude value for the total Loss Angle due to the coatings and the substrate.

$$\phi_{Total} = \frac{\Delta E_{Total}}{E_{Total}} = \frac{\Delta E_{Coating} + \Delta E_{Substrate}}{E_{Coating} + E_{Substrate}} \tag{50}$$

The total Loss Angle is given by the total energy dissipated by each component divided by the total energy stored within each component. Then (50) can be rewritten

$$\phi_{Total} = \frac{\phi_{Coating} E_{Coating} + \phi_{Substrate} E_{Substrate}}{E_{Coating} + E_{Substrate}} \tag{51}$$

As a simplification, we can model all of the components as springs connected in series, each with its own "spring constant", k.

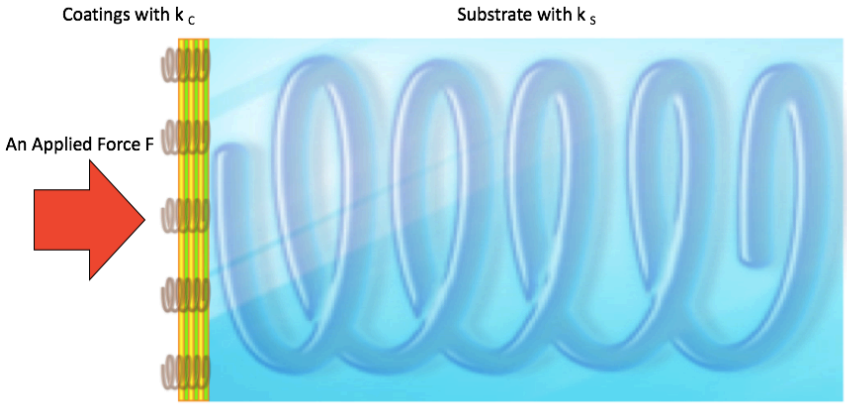


Figure 15. Simplified model of the multicomponent system consisting of the stacks of optical coatings deposited onto a cylindrical fused silica substrate. An arbitrary force is applied to calculate the amount of energy stored in the components of the system.

The Force is equal on both components, therefore

$$F = -k_s \Delta x_s = -k_C \Delta x_C \tag{52}$$

from simple springs:

$$E_S = \frac{1}{2} k_s {\Delta x_s}^2 \tag{53}$$

$$E_C = \frac{1}{2} k_C {\Delta x_C}^2 \tag{54}$$

the energy stored in each component is given by

$$E_S = \frac{F^2}{2k_s} \tag{55}$$

$$E_c = \frac{F^2}{2k_c} \tag{56}$$

substituting (55) and (56) back into (51) the applied force cancels and we have

$$\phi_{Total} = \frac{\frac{\phi_{Coating}}{k_c} + \frac{\phi_{Substrate}}{k_S}}{\frac{1}{k_c} + \frac{1}{k_S}} \tag{57}$$

In the simplified model the spring constants, or "stiffness" of the two materials is approximated with the expression

$$k_i = \frac{Y_i A_i}{T_i} \tag{58}$$

where Y_i is the material's Young's Modulus, A_i is the surface area and T_i is the thickness. Since the coatings cover the entire surface of the substrate they share the same value for A, which cancels. The thicknesses are mentioned above, $4\text{x}10^{-6}$ m for the coatings and $20\text{x}10^{-2}$ m for the substrate. The Young's modulus for Titania doped Tantala is ~ 132 - 177 GPa (Abernathy, Harry et al, 2017) and for fused silica it is ~ 73 GPa. Substituting, we end up with the expression

$$\phi_{Total} = \frac{\frac{\phi_{Coating} T_C}{Y_C} + \frac{\phi_{Substrate} T_S}{Y_S}}{\frac{T_C}{Y_C} + \frac{T_S}{Y_S}} \tag{59}$$

which, when the material values above are plugged in, gives us a total Loss Angle of approximately $\phi_{Total} = 2\text{x}10^{-8}$ (recall that ϕ of the fused silica substrate alone is ~ 10^{-8}). The very thin layer of poor Quality factor optical coatings was able to increase the Loss Angle of the substrate alone by a factor of 2. But in figure 16, it is shown that improving the Loss Angle of the coatings can only help to a point. Eventually, the Loss Angle of the substrate begins to dominate and no further improvements can be made unless higher Quality factor substrates can be implemented.

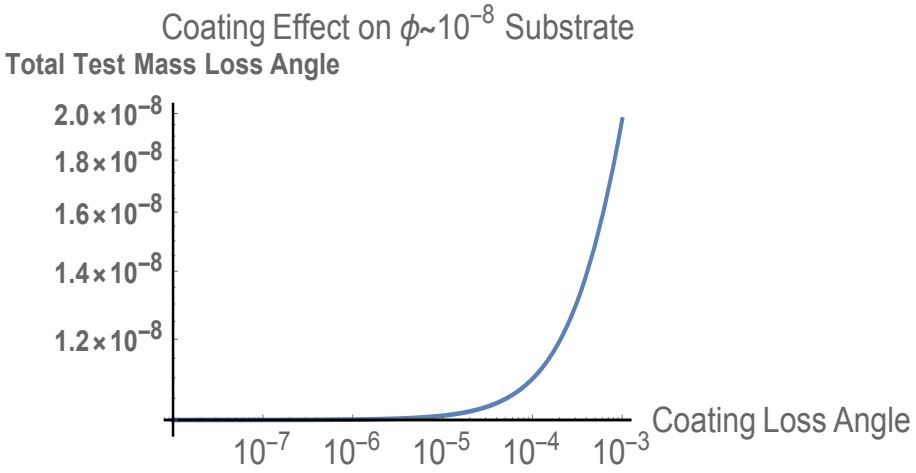


Figure 16. Log-Log plot of total Loss Angle for the system of substrate and coatings as a function of the Loss Angle of the Optical Coatings, that there is a benefit to improving the Loss Angle of the coatings to a point, and then the relationship flattens out as the large substrate dominates the energy losses.

The above was just a rough estimate to illustrate the ill effect of the coatings on the overall potential for the test masses to dissipate energy and induce noise. The next section will show the more rigorous treatment that models how much the Coating Brownian motion injects noise into an actual Gravitational Wave detector.

3.4 Levin's Formula for Coating Noise

In 1998, Yuri Levin, then at the California Institute of Technology, published a paper (Levin, 1998) outlining a simple yet powerful way to calculate the amount of strain noise injected into the power spectrum of a Gravitational Wave detection due to the energy dissipated in the optical coatings and substrate that form the test mass. This method has become the standard within the Gravitational Wave detection community with which to model the Coating Brownian Noise.

The Fluctuation Dissipation theorem given in (44), gives an expression relating the spectral density of the fluctuations in one degree of freedom to the temperature of the thermal bath and the real part of a term called the complex admittance associated with that degree of freedom. Levin focuses on the specific degree of freedom causing a phase

change in the laser signal from motion (back or forth) in the direction of the laser beam propagation. He names this $x(t)$

$$S_x(f) = \frac{k_B T}{\pi^2 f^2} Re\{Y(f)\} \tag{44}$$

I have included (44) again for ease of reading, but also because it now has a more precise definition. Previously, the $x(t)$ of the spectral density referred to any single degree of freedom but now it is literally detected motion in the x direction.

To determine the effect on the relevant degree of freedom, Levin suggests placing an imaginary oscillating pressure onto the surface of the coated test mass with a distribution matching the power intensity of the light beam that interrogates the position of the surface (figure 17). The force resulting from the application of the pressure is made to oscillate at the frequency f at which the noise is to be calculated. It is important to remember that this applied pressure is purely a thought experiment, that the applied force eventually cancels out, and that it does not imply that the laser pressure is driving the fluctuations. The fluctuations are going to occur as long as the test mass is in contact with a thermal bath. The purpose of the *gedanken* pressure is to serve as a device that will calculate the specific surface fluctuations affecting the length measurement just as the light beam would.

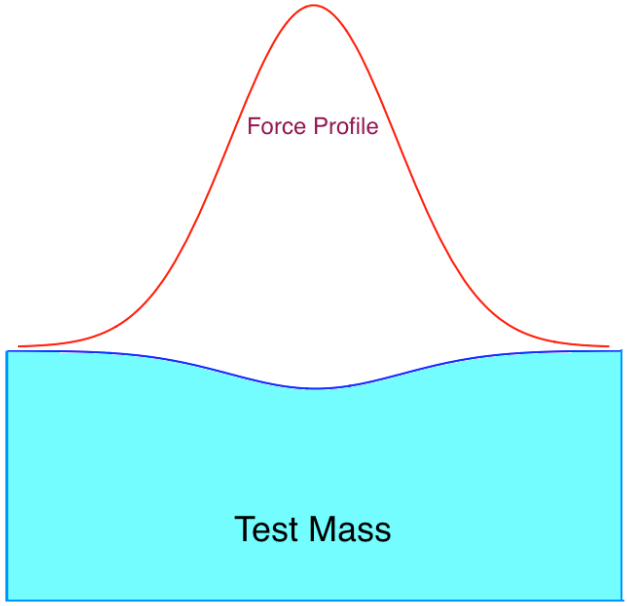


Figure 17. Illustration of the pressure profile that Levin proposes placing over the surface of the test mass so that the relevant fluctuations of the surface can be "detected" by his mathematical formalism. The low amplitude Gaussian response of the test mass, (blue curve mirroring the red one) is the deformation induced by the force. The deformation is then used to calculate the elastic energy stored in the different components of the test mass, which would be dissipated according to the loss angle specific of each material and each frequency. These are the only fluctuations that would cause the mechanical thermal noise fluctuations of the surface detected by the stored light beam.

The Levin approach defines $Y(f)$ in such a way so that it is the only component of the system composed of coatings and substrate that will affect (44) when interrogated by a laser. The imagined force will drive the momentum of the system in the x direction and so will imbue the test mass with energy in the form of an interaction term in the total Hamiltonian.

$$H_{int} = -F(t)x \tag{60}$$

The admittance, Y, is defined as the amount with which a structure allows itself to be moved given a unit of oscillatory force

$$Y \propto \frac{\Delta x}{F_{osc}} \tag{61}$$

Levin uses this relation and expresses the complex admittance as a function of frequency where the applied force and the position response are acted on with the Fourier transform

$$Y(f) = 2\pi i f \frac{x(f)}{F_{osc}(f)} \tag{62}$$

which has units of power over the square of force. Since this should be an expression that relates the dissipation properties of the material to the noise in the spectral density, the power should be the power dissipated by the coated test mass and the force is the imagined force on the test mass which has the form,

$$F(t) = F_0 Cos[2\pi\, f\, t] \tag{63}$$

He is then able to state that the real part of (60) is given by

$$|Re[Y(f)]| = \frac{2W_{diss}}{F^2} \tag{64}$$

where W_{diss} is the power dissipated by the test mass and F is the oscillating force. This allows (44) to be rewritten as

$$S_x(f) = \frac{2k_B T}{\pi^2 f^2} \frac{W_{diss}}{F^2} \tag{65}$$

We must now find the amount of power dissipated by the coatings. From the definition for Loss Angle in (50) we can write the power dissipation by

$$W_{diss} = 2\pi f U_{max} \phi(f) \tag{66}$$

where U_{max} is the total amount of strain energy (the blue, response curve in figure 17) stored in the test mass during one cycle of oscillation and the system's Loss Angle as a function of frequency has returned. Levin then uses elasticity theory to derive an expression for U_{max}. His mathematical steps are beyond the scope of this thesis, but it suffices to write the final expression which is comprised of the material's mechanical properties, and parameters of the applied oscillating force.

In the expression below, E is the Young's modulus for the optical coating, σ is its Poisson ratio, r is the beam spot size (which may be thought of as the FWHM radius of the applied Gaussian pressure distribution), R is the full radius of the test mass surface, and I is a Gaussian beam parameter, $I \cong 1.87322$.

$$U_{max} = \frac{F^2}{\pi^2 E\, r}(1-\sigma^2) I \left[1 + \mathcal{O}\left(\frac{r}{R}\right)\right] \tag{67}$$

where the higher order terms on the right of the brackets disappear when the beam spot size is much smaller than the size of the test mass surface. Plugging (66) into (65) and then that into (64) gives the final form for the amount of Coating Brownian Noise injected into the spectral density of the signal. Note that the force that was imagined to be applied to the test mass has completely dropped out of the expression, and that all that remains to cause the contact with the thermal bath is the material's dissipative response, $\phi(f)$.

$$S_x(f) = \frac{4k_B T(1-\sigma^2)}{f\, \pi^3 E\, r} I\, \phi(f) \tag{68}$$

In an elastic system, the stored energy is given by the Hook's law, U = ½ k x^2, therefore the strain limit imposed by thermal noise is proportional to the square root of (68). The behavior of the square root of this expression can then be visualized as a linear function with slope -0.5 in a log-log plot of strain as a function of frequency (as seen in the LIGO noise plot).

Plugging in all the numbers, this limit is dominated by the losses in the thin coatings, while the substrate's contribution is a parallel line a factor of 2 or 3 lower.

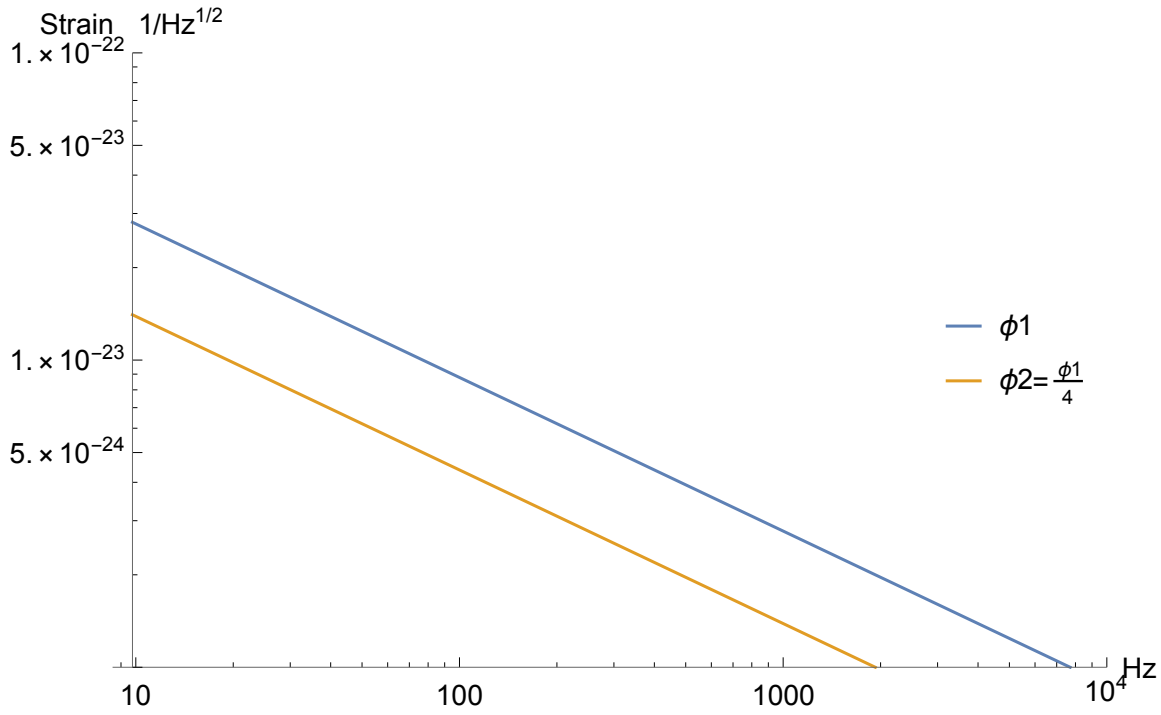


Figure 18. Plot of the Levin formula predicts a decrease in the noise by a factor of ~2 at the 100 Hz detection frequency if the Loss Angle of the test mass was improved by a factor of 4.

3.5 Methods for Measurements of the Loss Angle of Optical Coatings

The typical experimental procedure for measuring the Quality factor for a material is to isolate it as much as possible from the environment, excite it into its resonant modes and observe the ring down. The Q is then extracted by counting the number of cycles that occur in the time it takes for the amplitude of the oscillation to damp down to 1/e of its initial value. Or, equivalently, if the resonant frequency is known with acceptable precision, the experimenter can measure the amount of time in which the ring down occurs, Δt and extract the number of cycles from

$$N = \frac{\Delta t\, f}{2} \tag{69}$$

According to Yuri Levin's model, the frequency (69) is that of the applied theoretical oscillating force that allows calculation of the energy stored in the system, which will

eventually be dissipated. If we applied a force with frequency f to the system it would never ring down and we could not measure (69). The only frequencies at which the system can oscillate freely are the frequencies of the natural modes. If the material system does not possess well defined modes then the Q cannot be measured using (69).

Optical coatings are thin films, which in and of themselves do not possess well defined mechanical resonant modes. To measure their Q, they are deposited onto objects that do have well defined modes. The coatings then share the same mode shapes as the underlying substrate and the Q of the coating material can be extracted through a method of subtraction that will be explained in detail in the subsection "Extracting the Loss Angle by Subtraction".

Coating a Substrate

It is desirable to deposit the coatings using the same method that is employed when the test masses are manufactured. Variations in coating tension, annealing temperature, and impurities due to the coating process will all affect the Quality factor and these parameters are specific to the coating method. It is also important to coat onto a substrate that shares similar mechanical loss properties with the fused silica substrates that are used in the test masses. Even the mass of the substrate is relevant, because larger masses will heat up less, possibly resulting in different states, but obviously it is only feasible to use small test samples in development.

Two methods for depositing coatings onto a substrate are Electron Beam Induced Deposition (EBID) and Ion Beam Sputtering (IBS). Both methods may utilize Ion Beam Assist (IBA) which adds further control to the procedure.

With EBID, the coating material is heated in a crucible by a beam of electrons. The molecules of the material are sublimated from the surface of the puck, each with kinetic energy substantially smaller than the material's melting temperature, which is of the order of ~.1 eV. A plume of the material is ejected outwards away from the target. The entire line of sight interior of the chamber is coated with the material including the substrates, which are held in a rotating carousel to provide even coating. A Quartz Crystal Rate Monitor is used to determine when the appropriate thickness of coating has been applied. The resonant frequency of the Quartz will decrease as more coating is deposited on its surface, monitoring the decreasing frequency gives a measure of the deposited thickness. The material that lands on the target substrate arrives with little energy and immediately set in place.

The IBS method is similar in all respects except that the target is physically bombarded by ions at several hundred of eV of energy, which force ejection of the target material through collisions rather than through the thermally induced sublimation of EBID. The result is a much more energetic material depositing onto the substrate. The deposited atoms can have energies of many tens or even hundreds of eV. This is desirable if one wishes coating layers that are uniform with few voids (see figure 19). The low energies of the EBID ejected molecules allow them to freeze into place almost immediately after contact with the substrate, as they do not have thermal energy to move and re-arrange pre-existing atoms. There will be a high likelihood that holes form, which are then covered by a new layer. The results are often milky-looking, somewhat spongy coatings.

On the other hand, the higher energies (~100 eV per ejected molecule) of the IBS sputtered atoms is sufficient to melt the atoms in the immediate vicinity of the landing spot and yield an effective melting radius on the order of 10 atoms (typical melting energy is 0.1 eV per atom). This causes the surrounding volume to stay in a liquid state for a very short time on the order of picoseconds, yet sufficient to allow surface tension to come into play. The coated material will smooth itself out through the action of the surface tension before new material is added.

In both EBID and IBS, the use of a second ion beam (IAD) directed at the substrate during coating will deliver additional energy that will further drive the desired smoothing effect mentioned above.

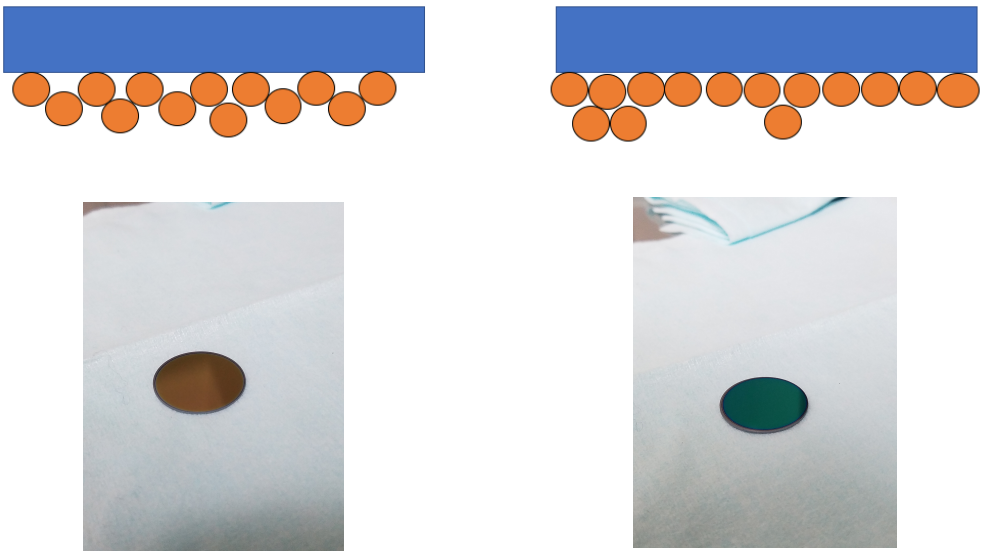


Figure 19. Different arrangements of deposited coating layers that will emerge due to the different coating methods. On the left, the molecules (orange) have been thermally ejected from the target by the electron beam with low enough energy so that they "freeze" into place on the substrate (blue). As a result, new material will arrange itself in a way to cause voids to form between the coating molecules. On the right side is an illustration of the layers that form due to ion beam sputtering. The much larger energies allow the surface of the substrate to melt and the coating material to benefit from surface tension which pulls the molecules into line. Less voids form. Ion Beam Assist can also be used in both cases to keep the surface of the deposited coating energetic enough to keep from freezing into place before the most organized configuration can be achieved. Below the illustration are two photographs from our coating facility at University of Sannio. On the left, no ion assist was used. On the right, the ion assist beam was used, which provided higher optical density and thus the green color.

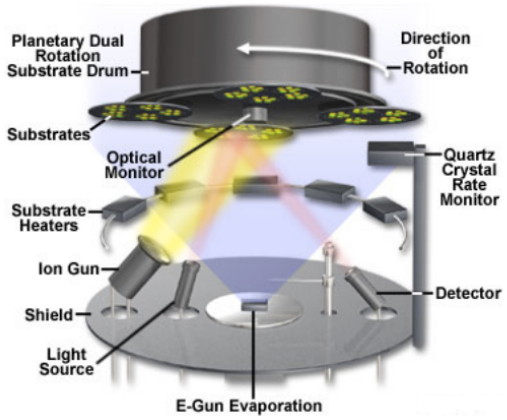


Figure 20. Simplified schematic of a typical EBID coating chamber. The target is sublimated by the electron beam into a cone of vapor (blue) that covers all surfaces within the line of sight. The ion gun (yellow beam on the left) is providing the IAD so that the deposited material is continually smoothed out and few voids form. The substrates are held in a carousel at the top of the chamber, which rotates to aid producing an even coating distribution. A quartz crystal, serving as the "canary in the coal mine", is positioned in the chamber near the substrate during the coating and its resonant frequency is constantly monitored. When the quartz's frequency decreases to a certain point it indicates that the desired deposition thickness for the process is achieved. Image from www.olympus-lifescience.com.

Extracting the Loss Angle by Subtraction

Once the substrates have been coated, the total Quality factor of the system needs to be measured. The samples are set in mechanical vibration and then the ring-down is observed. The coating-substrate system will lose an extra amount of oscillation energy per cycle due to the mechanical losses in the coating in addition to that due to the substrate. If the amount of energy that is lost due to the substrate is subtracted then the difference will be related to the Quality factor of the coating. The general procedure (Tianjun Li et al, 2014) is as follows.

The naked substrate's Q is measured (using eq. 69) prior to coating in order to establish a value for its Loss Angle, $\phi_{Substrate}$. After deposition, the Q for the coated substrate is obtained with the same method, giving a value for the total Loss Angle of the system, ϕ_{Total} . From (51), the two values are related to the Loss Angle of the coating

itself, and that expression can be re-written to define a new term known as the Dilution Factor.

$$\phi_{Total} = \phi_{Coating} D + \phi_{Substrate}(1 - D) \tag{70}$$

where the Dilution Factor is

$$D = \frac{E_{Coating}}{E_{Total}} \tag{71}$$

where $E_{Coating}$ is the instantaneous energy stored in the coating and E_{Total} is the instantaneous energy stored in the composite system. The Dilution Factor describes the magnitude of the effect that the coating has on the losses of the system. A small Dilution Factor equates to more energy being stored in the substrate during the oscillations.

The Loss Angle of the coating is then given by

$$\phi_{Coating} = \frac{\phi_{Total} - \phi_{Substrate}(1 - D)}{D} \tag{72}$$

The problem is that the substrate is usually much thicker than the thin coating and contains much more energy, resulting in very small dilution factor. Examining (70) first, if the value for Dilution Factor is very small then

$$\phi_{Total} \sim \phi_{Substrate} \tag{73}$$

and if that is the case, then (72) will involve the subtraction of two very similar values, each with their own amount of uncertainty, which leads to a large relative uncertainty in the calculated value for $\phi_{Coating}$. It is therefore important to devise a setup that will yield the largest possible value for D.

A more detailed expression for the Dilution Factor based on (71) which relates to the thickness and mechanical properties of the coating and the substrate can be written as

$$D = \frac{Y_{Coating} I_{Coating}}{Y_{Coating} I_{Coating} + Y_{substrate} I_{CoatedSubstrate}} \tag{74}$$

where the Y values denote the Young's moduli of the materials and the I values express the moment of inertia tensors of the layers calculated with respect to the neutral plane of the flexing. Since the coatings cover the entire surface of the substrate, the moment of inertia will depend on the thicknesses of the two constituents. Therefore, if we take the Young's moduli to be relatively similar for both the coatings and the substrate, then the Dilution Factor will be largest when the thickness of the coating is on the order of the thickness of the substrate.

The Cantilever Method

Measurements of the Quality factors of the optical coatings that are used on the test masses in LIGO have been performed (Granata et al, 2018) by observing the ring down of fused silica cantilever blades coated using the IBS method. The thicknesses of the blades were approximately 100 microns, and the coatings were deposited in monolayers of either the high index TiO_2 doped Ta_2O_5 or the low index Silica material, each with thicknesses ranging from approximately 100 to 500 nm.

The fused silica blades were spot welded on one end to a thicker slab of fused silica to give the blade a clamping point. The cantilever blade was excited into resonance through electrostatic actuation, which exploits the dielectric properties of the coated system so that an applied electric field induces a mechanical force on the cantilever.

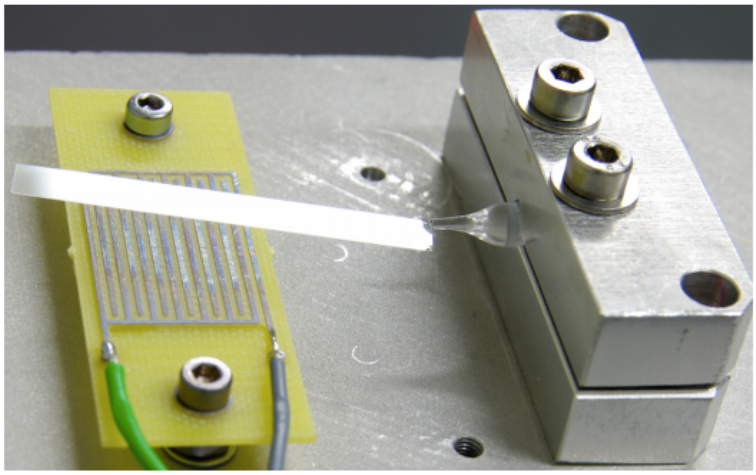


Figure 21. Photograph of a fused silica blade that has been welded to a larger mass of fused silica that has been clamped. The electrostatic actuating comb beneath the blade is used to excite the coated cantilever into its resonant modes.

Once the blade is excited into resonance the electric field is cut and a HeNe laser reflected off the blade surface, onto a Quadrant Position Sensing Photodiode monitor the oscillations. This optical lever system allows the frequency and amplitude of the oscillations to be measured to extract the ring down time, and thus the Quality factor, may be observed.

Table 4 gives the analytically calculated and Finite Element Analysis Dilution Factors for the coated cantilever samples. Please note that the table lists a reciprocal definition for the Dilution Factor than that defined above, so that a large Dilution factor corresponds to the *substrate* dominating the measurement.

sample[a]	coating	t [nm]	D	D_{an}	$\langle\phi_m\rangle$
w8	$TiO_2Ta_2O_5$	513		37.7	2.4 ± 0.2
151	$TiO_2Ta_2O_5$	514		37.7	2.7 ± 0.3
190	$TiO_2Ta_2O_5$	502		38.6	2.2 ± 0.1
GH-A1	$TiO_2Ta_2O_5$	512		37.8	2.7 ± 0.1
GH-A4	$TiO_2Ta_2O_5$	512		37.8	2.3 ± 0.2
GH-A5	$TiO_2Ta_2O_5$	127	149.6	149.1	2.7 ± 0.2
GH-A6	$TiO_2Ta_2O_5$	129		147.0	2.4 ± 0.3
GH-A7	$TiO_2Ta_2O_5$	250	77.7	74.8	2.3 ± 0.1
GH-A8	$TiO_2Ta_2O_5$	250		74.8	2.2 ± 0.1
GH-A7	$2 \times TiO_2Ta_2O_5$ [b]	250/254		38.3	2.3 ± 0.1
GH-A8	$2 \times TiO_2Ta_2O_5$ [b]	250/254		38.3	2.2 ± 0.1
H-1	SiO_2	483	78.0	80.4	0.48
H-2	SiO_2	483		80.4	0.41
GH-A9	SiO_2	385	97.3	96.3	0.47 ± 0.08
GH-A10	SiO_2	385		96.3	0.46 ± 0.05

[a] samples with the same coating specifications have been coated together, by pairs.

[b] both surfaces have been coated.

Table 4. The Dilution Factors above, (defined as the inverse of the definition described in this paper so that small dilution factor is desirable and represents substrate contribution as opposed to coating) have values on the order of 10^{-2}, are shown for different coated samples along with the average Loss Angle across frequencies that was measured for that sample. The units for loss angle here are in 10^{-4} radians. Note that the Dilution factor improves by a factor of 2 (goes down) when the coatings are applied to both sides of the blade as was done for samples GH-A7 and GH-A8, but that the measurement of the Loss Angle remains consistent with that measured for single sided coating, demonstrating a relatively low uncertainty in the measurement, indicating that the value for the Dilution Factor is sufficient.

Although the fused silica cantilever blades are 1000 times thicker than the coatings a reasonably good Dilution Factor comes from the fact that the coatings are the farthest from the bending neutral plane and thus have geometrically larger moments of inertia. The high precision determination of the mode lifetimes yields single sample measurements with reasonably low uncertainty (the results of which can be seen in table 4). Unfortunately, the measurement is sensitive to systematic errors from the clamping method. It has been observed (Martin et al, 2008) that in particular the lowest frequency, first mode of resonance for the cantilever shape suffers much higher clamping losses than the other modes. This is due to the low frequency motion resulting in friction of the blade at the clamping location. The losses are significant enough to give significantly different Q values for the same sample if it is unclamped and re-clamped for subsequent

measurements. This is true for all modes, but especially for the first mode, which is usually the one closest to the frequency region of interest for GW detection.

Since the noise in the GW detectors due to Coating Brownian effects is a function of frequency and Loss Angle is frequency dependent, it is imperative to have an accurate measurement of the Loss Angle at the various mode frequencies.

Gentle Nodal Suspension

Another method for measuring the Loss Angles of optical coatings, and one which suffers much less from frictional clamping losses, is the Gentle Nodal Suspension method or GeNS. With GeNS, the substrate is a polished fused silica disc approximately 1 mm in thickness and 7.5 cm in diameter. The coated disc is balanced on a silicon convex lens with a radius of curvature of ~ 60 mm (Vajente et al, 2017). When this system is excited the resonant modes that exhibit a nodal point around the center of the disc where it is balanced have very little motion at this point and thus are mostly unaffected by contact dissipation.

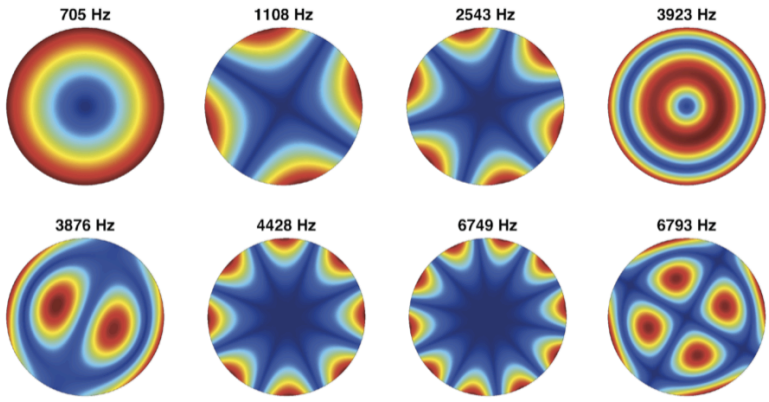


Figure 22. First 8 mode shapes for an oscillating disc. The amplitude of oscillation is signified by the color with red being the largest and dark blue being the smallest. The disc is balanced at the center, so that modes that oscillate very little there will lose very little energy due to friction on the contact point. The modes corresponding to 705 Hz, 3876 Hz and 3923 Hz lose a sizeable portion of energy due to friction because of larger amplitude motion near the center node. Image taken from (Vajente et al, 2017).

The frequency and amplitude observations are made with an optical lever similarly to those in the cantilever experiment previously outlined. The entire system is kept in high vacuum so that air will not damp the motion. The oscillations are induced by a white noise signal fed into the electrostatic actuating comb for about 3 seconds, then the disc is allowed to ring down for hours.

Figure 23 illustrates sample data that taken in a measurement of the Quality factor of an uncoated fused silica disc. Note the larger uncertainty and lower measured values in the measurements when losses are present at the support point. Also note the large, and yet frequency dependent, measured values for Quality factor of fused silica.

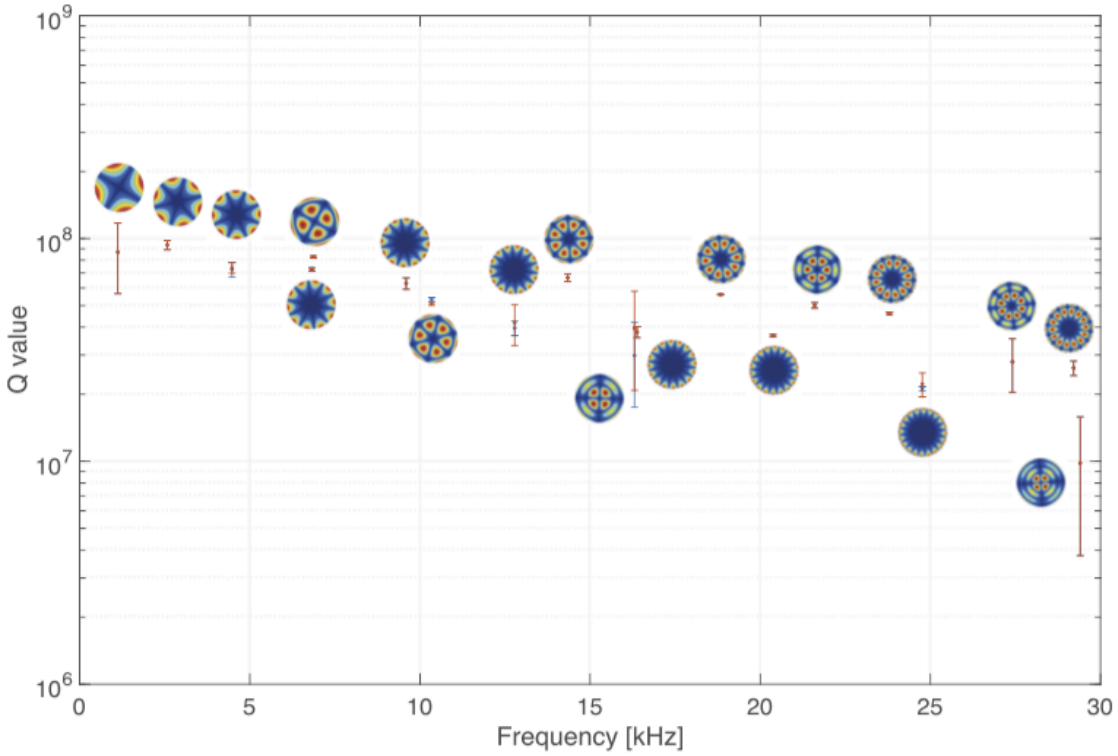


Figure 23. Data extracted by (Vajente et al, 2017) using the GeNS method on an uncoated fused silica disc

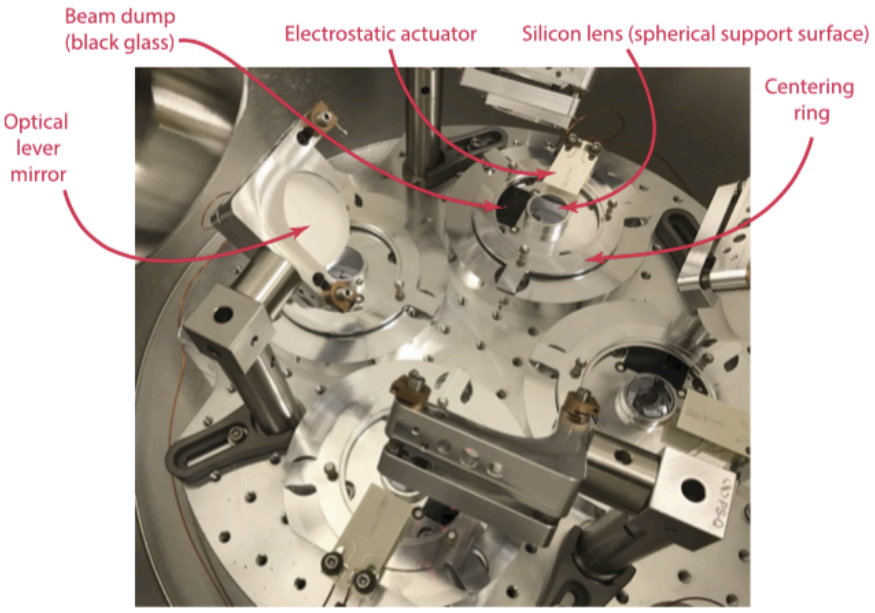


Figure 24. View inside the vacuum chamber where the holding and actuating sections of the GeNS apparatus are stored. Note the 4 silicon lenses, this setup is able to measure up to 4 samples at the same time. Image taken from (Vajente et al, 2017).

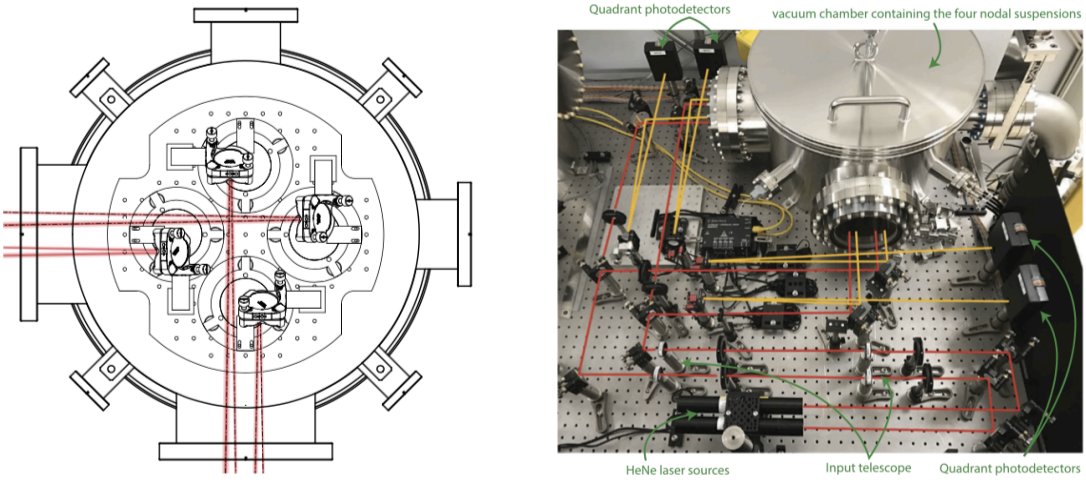


Figure 25. Beam paths for the various optical levers that are used to measure the frequency and amplitude of the discs' motion. Also pictured are the Quadrant Position Sensing Photodiodes. The red beams are the input and the yellow are the return paths which contain the discs' mechanical oscillation information. The vacuum chamber (upper part of image on right) keeps the system at ~10^{-6} Torr. Image taken from (Vajente et al, 2017)

Although the GeNS method for measuring Quality factor suffers less losses due to friction than the clamped cantilever method, the disc substrates are 10,000 times

thicker than the coatings which is worse than the Dilution Factor achieved in the cantilever method by a factor of 10. The GeNS yields more reliable results because it is mostly free of the systematic clamping error, but is still limited by its unfavorable dilution factor.

Clearly, quality factor measurements for coatings on thinner substrates would enjoy advantages from improved dilution factors.

Summary of Dilution Factor and Nano-Layer Motivation

It is shown above that precision in a Quality factor measurement of an optical coating is affected by the ratio in thicknesses of the coating to the substrate. The coatings LIGO is currently using are on the order of ¼ λ optical thickness, ~100 nm actual thickness, and they have Loss Angles that are significantly impairing the sensitivity of the GW detections due to their Brownian Noise. It has been observed (Glover et al, 2017) in images taken of the test masses off axis and while the laser is incident upon them, that there are many visible point scatterers.

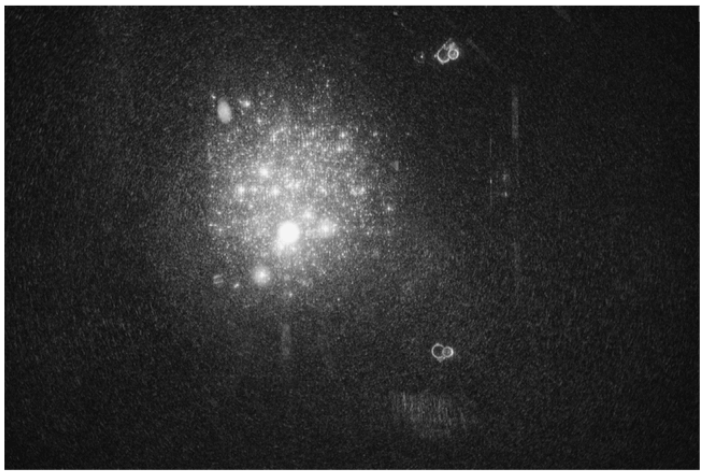


Figure 26. Photograph of one of the LIGO end test masses which exhibits many scatterers. This image was taken from (Glover et al, 2017).

The cause of these apparent scatterers is not yet known, and the theories range from an optical effect due to laser speckle, to crystallites or voids that either form during the deposition of the coatings. Microscope observations by researchers at California State University, Los Angeles have been made that rule out the laser speckle explanation. Scatterers were observed at increasing depths into coatings of witness samples.

If these scatterers are crystallites that have formed in the high or low index optical coating layers, then their growth may be inhibited by segmenting the thickness of individual coatings layers in what are termed "nano-layers". With nano-layers, the ¼ λ thick layer condition for reflection is achieved by stacking multiple alternating index of refraction layers. Each nano-layer may have thickness on the order of 1 nm, together adding up to the ¼ λ. The measurement of the Quality factor of these nano-layers is even more difficult, the Dilution Factor will play an even bigger role in the measurement of Loss Angles. This is the main motivation to seek out thinner substrates that can be deposited onto for measurement.

Method	Coating Thickness	Substrate Thickness	Dilution Factor
Coated Cantilever	$\sim 10^{-7}$ m	$\sim 10^{-4}$ m	$\sim 10^{-3}$
GeNS	$\sim 10^{-7}$ m	$\sim 10^{-3}$ m	$\sim 10^{-4}$
Coated Cantilever	$\sim 10^{-9}$ m (nano-layer)	$\sim 10^{-4}$ m	$\sim 10^{-5}$
GeNS	$\sim 10^{-9}$ m (nano-layer)	$\sim 10^{-3}$ m	$\sim 10^{-6}$

Table 5. Various Dilution Factors that are yielded as a function of substrate and coating thicknesses. If it is found that nano-layers inhibit the growth of crystallites then there will be a need to perform Loss Angle measurements on them. From the values in the last two rows it is shown that the Dilution Factor will suffer greatly if the parameters of the measuring substrate are not changed to compensate for the much thinner coating layers.

CHAPTER 4

Our Method

4.1 Silicon Nitride Membranes as Substrates

Large dilution factors, i.e. a large fraction of the vibrational energy being stored in the substrates, are a problem when measuring coating Q factors. It is expected to become a daunting problem when attempting to measure the performance of the nano-coatings proposed to reduce scattering and possibly thermal noise in future mirrors (Cole, et al. 2013) We are attempting to use Silicon Nitride (Si_3N_4) in membrane form as a substrate to reduce the Dilution Factor of the Q measurements and, at the same time, avoid energy losses due to friction at the contact point of the system as well as minimizing suspension recoil losses.

The membranes we started with are produced as windows in x-ray microscopy but these membranes can be fabricated with various thicknesses and sizes.

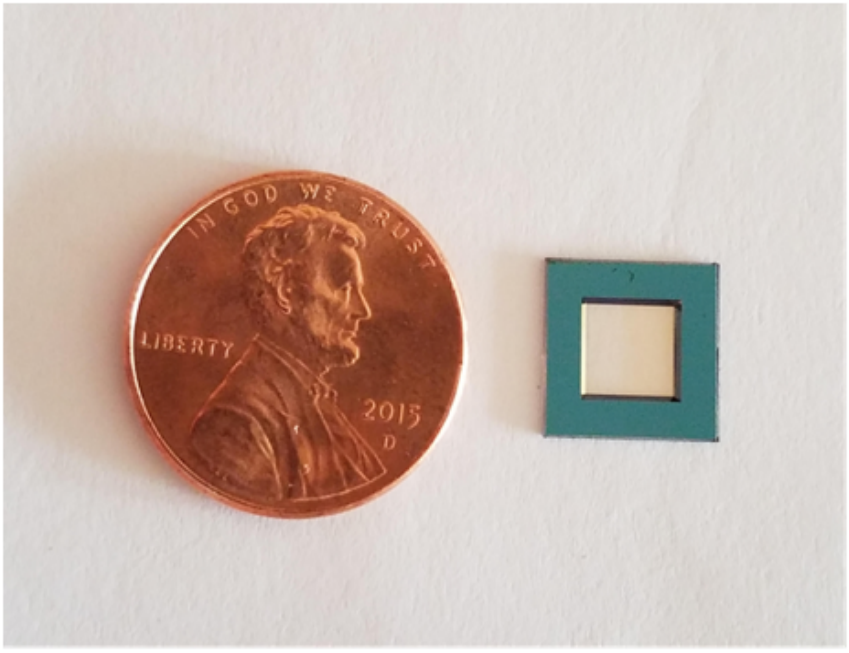


Figure 27. A Silicon Nitride membrane pictured next to a penny for scale. This membrane is on a 10mm x 10mm Silicon frame which has a window 5 mm square. This membrane is 100 nm thick.

The fabrication process of the membranes involves depositing Silicon Nitride, using IBS or EBID, onto a crystalline Silicon wafer. Once deposited, a photo-resist mask and a Potassium Hydroxide solution are used to etch away the window. The etching stops at the Silicon Nitride and what remains is the membrane attached to the frame. This procedure can be used to create a variety of shapes as well as membranes that have island masses of Silicon wafer in the center.

The idea of an island mass to lower the resonant frequency of the membrane was invented for this work, and realized specifically for us by Shiuh Chao and Sung En at the National Tsing Hua University in Taiwan. More detail for this will be given within the next section.

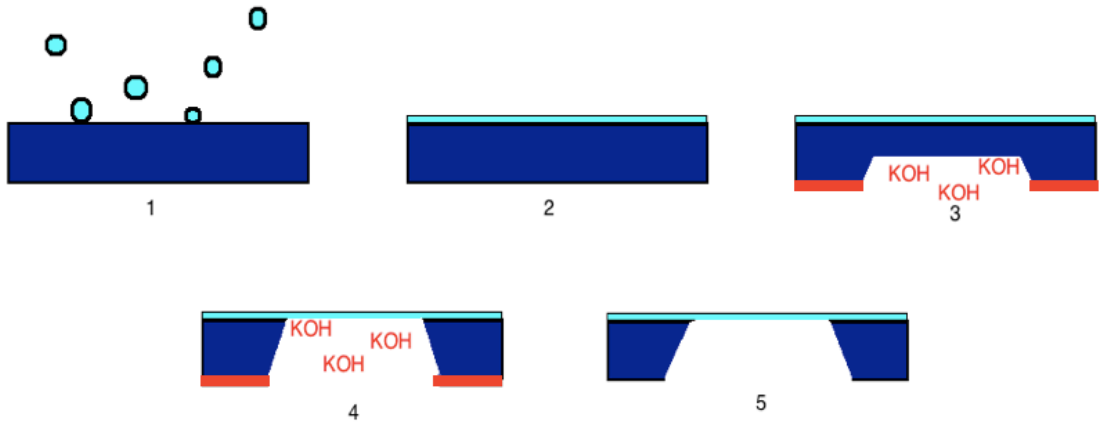


Figure 28. Side view Illustrating the fabrication process for a Silicon Nitride membrane. 1) The Silicon Nitride is evaporated and deposited, 2) onto a crystalline silicon wafer. 3) A mask (red) is applied and a solution of Potassium Hydroxide is used to etch away the unmasked Silicon. 4) The solvent stops at the Silicon Nitride. 5) What remains after washing out the mask is the Silicon Nitride membrane held to the rigid Silicon Frame.

To accurately characterize low Loss Angle coating materials that will be used in the GW detector it is essential to perform the Q measurement for a system of coatings and substrate that is as physically similar to that of the LIGO test masses as possible. The substrates do not need to be 20 cm thick fused silica cylinders as in the detectors, yet

should have similar loss properties. It has been observed that Silicon Nitride membranes can possess Loss Angles as low as 10^{-7} (Zwickl, 2008) at very low temperatures and typically around 10^{-6} at room temperature (Table 3). While not as low as the Q of annealed fused silica, these are relatively low values for loss angle compared with the expected coating values, and the membranes are so thin that the substrate would be far from dominating the energy losses during a Q measurement of the coatings.

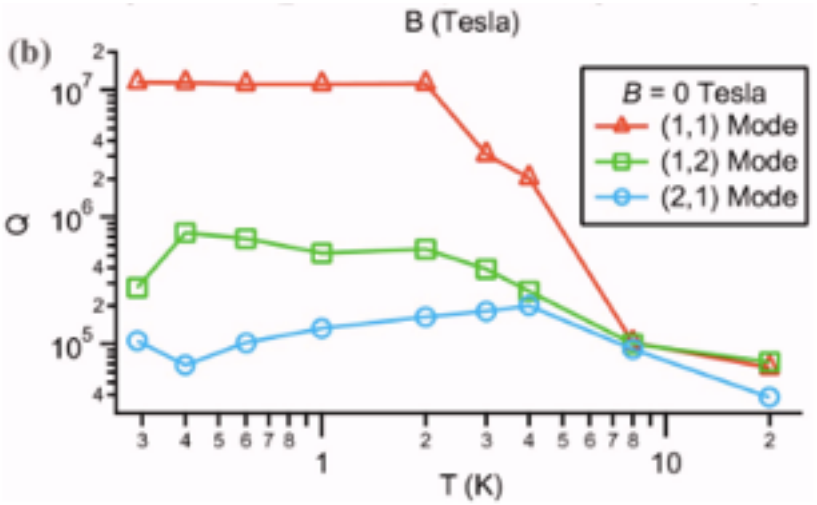


Figure 29. Graph from the Zwickl paper that show the very high Q factor (low loss angle) for Silicon Nitride membranes held at 300 mK. Note the steep drop in order of magnitude Q when the temperature reaches ~10 K.

A very important benefit of using the membranes as substrates is that they come pre-attached to the very rigid Silicon frames. This makes them easy to handle, (although they are still extremely fragile) and provides a relatively wide surface that can be used to glue the frame to a massive glass stage. The gluing method proposed for attaching the frame to a stage will mitigate the type of frictional losses due to low frequency vibrations around the contact points that plague the cantilever method.

The last benefit and chief motivation for using the membranes as substrates is their similarity in thickness to that of the coatings, therefore during vibration the elastic energy stored in the substrate is not dominating and the dilution factor is much improved.

Method	Coating Thickness	Substrate Thickness	Dilution Factor
Coated Cantilever	$\sim 10^{-7}$ m	$\sim 10^{-4}$ m	$\sim 10^{-3}$
GeNS	$\sim 10^{-7}$ m	$\sim 10^{-3}$ m	$\sim 10^{-4}$
Coated Cantilever	$\sim 10^{-9}$ m (nano-layer)	$\sim 10^{-4}$ m	$\sim 10^{-5}$
GeNS	$\sim 10^{-9}$ m (nano-layer)	$\sim 10^{-3}$ m	$\sim 10^{-6}$
Membrane	$\sim 10^{-7}$ m	$\sim 10^{-7}$ m	~1
Membrane	$\sim 10^{-9}$ m (nano-layer)	$\sim 10^{-7}$ m	$\sim 10^{-2}$

Table 6. Comparison of dilution factors. Significantly larger Dilution Factor is obtained using 100 nm membranes as substrates as opposed to any other method.

The thin membrane is the only option that can yield a decent Dilution Factor when measuring single "nano-layer" coatings, orders of magnitude better than the cantilever (table 6). The Dilution Factor for the membrane-coating system can be improved by depositing onto both sides of the membrane. When coating on both sides, the substrate remains in the neutral plane between compression and tension during oscillation. This further decreases the energy losses in the substrate thus minimizing the measurement errors when the coating losses are extracted through subtraction from the overall losses.

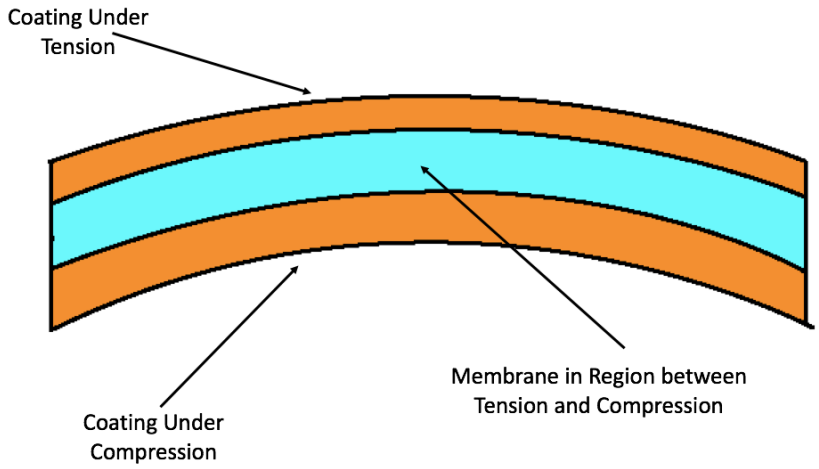


Figure 30. During oscillation, the coatings on the surfaces will be predominantly in tension or compression while the substrate is less stressed. Since mechanical losses occur when the material is stressed this arrangement minimizes the mechanical losses in the substrate.

As shown in table 3, Silicon Nitride membranes with 1 mm square windows and 50 nm thickness have 1st mode resonant frequencies around 134 kHz. It has also been shown that the Loss Angle is frequency dependent and that the functional form of this frequency dependence is not very predictable. It is therefore not possible to accurately extrapolate what a system's Quality factor will be at frequencies far from those measured. We need to characterize the loss properties of Optical coatings in the detection frequency band between 10 and 100 Hz, where they are relevant. Measurements of the Q of the coatings need to be made as close to those frequencies as possible. The uncoated resonant frequency for the 1mm square, 50 nm thick membrane of 134 kHz is far from that range. A solution is proposed in the next section.

The Finite Element Analysis software package COMSOL was used to determine the eigenfrequencies of the membrane, given the design, material's parameters and boundary conditions for how it is held. We have been able to simulate the range of natural modes for some membranes, and have found good agreement with the

experimental values found in table 3. COMSOL numerically solves the differential equations for the displacement from equilibrium across the membrane's surface at all points where the applied "mesh" intersects. The finer the mesh that is wrapped around the object, the greater the precision of the simulation. A problem is that fine details like membranes often require extra-fine meshes that are computationally forbidding. Simple membrane geometries do not require a very fine mesh in COMSOL when using the "Membrane Package" included in the COMSOL Multi-Physics library. Some results of these simulations are included. Finite Element Analysis software model the behavior of existing membranes and therefore will be adequate to predict the behavior of future geometries such as thicker and larger membranes that we want to develop to lower resonant frequencies and thus be more useful to measure the Q for candidate coatings and coating methods.

The calculated modes for a square membrane constrained on all edges is given by

$$f_{i,j} = f_{1,1}\sqrt{\frac{(i^2 + j^2)}{2}} \tag{75}$$

where $f_{1,1}$ is the frequency of the first mode and i and j are integers. From this we can make a table of the higher mode structure from the observed value for the first mode given in table 3.

Table of Frequencies in kHz Calculated from (75) with Experimental (Zwickl et al) 1,1 value 1mm square, 50 nm thick Silicon Nitride Membrane				
	j=1	j=2	j=3	j=4
i=1	133.7	211.398	298.962	389.799
i=2	211.398	267.4	340.869	422.797
i=3	298.962	340.869	401.1	472.701
i=4	389.799	422.797	472.701	534.8

Table 7. Frequencies calculated using the formula (75) and the measured first frequency in kHz from the experiment of Zwickl et al. of the resonant modes for a 1mm square, 50 nm thick Silicon Nitride membrane.

Table of Frequencies in kHz Observed by Experiment (Zwickl et al) 1mm square, 50 nm thick Silicon Nitride Membrane				
	j=1	j=2	j=3	j=4
i=1	133.7	211.316		389.555
i=2	211.566	267.554	340.886	
i=3	299.263	341.249	401.277	
i=4	390.036			

Table 8. Measured values performed by Zwickl et al in kHz for the same membrane dimensions as those in table 3, yet in a format that allows for easier comparison between experimental and calculated values than table 3 since that table gives the results beyond the first mode in the form of deviations away from the expected values.

COMSOL Simulation Values for Resonant Frequencies in kHz 1mm square, 50 nm thick Silicon Nitride Membrane				
	j=1	j=2	j=3	j=4
i=1	133.7	211.53	299.18	390.17
i=2	211.53	267.58	341.14	423.25
i=3	299.18	341.14	401.5	473.34
i=4	390.17	423.25	473.34	535.77

Table 9. COMSOL simulation (50 nm thick, 1mm square SiN membrane) values for the resonant modes in kHz. Note the agreement with the experimental values from table 8 within ~.2 kHz.

To obtain a first resonant mode frequency that agreed with the experimental data of table 8 we adjusted the membrane tension in COMSOL in small steps. The Young's Modulus, Poisson's Ratio and material density were all set to match the measured values for Silicon Nitride membranes. The tension at which the membrane is deposited is shown to have a significant effect on the resonant frequencies.

In plane force N/m Membrane Tension	1st mode frequency kHz	Computed 2nd mode frequency kHz	Experimentally Measured 2nd mode frequency kHz	COMSOL 2nd mode frequency kHz
5.6	134.41			
5.5	133.2			
5.55	133.8			
5.54	133.68			
5.545	133.74			
5.546	133.76			
5.547	133.77			
5.548	133.78	211.398	211.316	211.53 (Δ *from experiment* ~130 *Hz*)

Table 10. Values in the first column are the small steps in membrane tension leading to an acceptable value (matching the experiment of table 3) with which to run the simulation. The 2nd mode found by simulation is given to show that the value for tension we used leads to viable results for higher order modes. Higher modes than the 2nd also agree well as is shown in comparisons between table 8 and table 9 above.

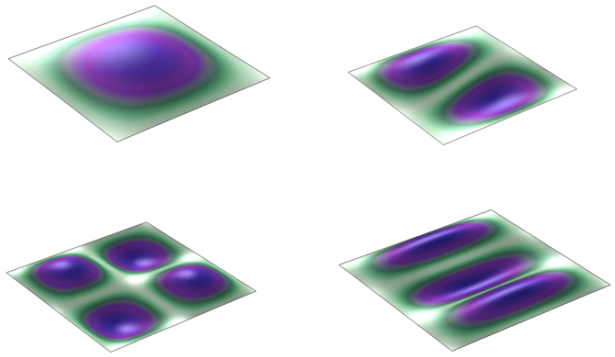


Figure 31. First 4 non-degenerate modes for the 1mm square, 50 nm thick membrane fixed on all edges modeled with COMSOL. The simulated values are given clockwise from the top left:
i=1, j=1 (133.78 kHz), i=1, j=2 (211.53 kHz), i=2, j=2 (267.58 kHz), i=1, j=3 (299.18 kHz)

More simulations were performed of membranes with the same material and tension parameters as for the 50-nm thick Silicon Nitride membranes, varying the size and thickness to predict the changes of resonant frequencies and design resonators closer to the detection band of the LIGO detectors (~1 to 1000Hz). The results are listed in table 11.

Side Length mm	Thickness nm	Surface Tension N/m^2	1st Mode Frequency kHz	Dilution Factor Standard Coating	Dilution Factor Nano-Coating
1	50	5.548	134	~ 0.4	~ 0.02
1	100	5.548	94.6	~ 0.3	~ 0.01
1	500	5.548	42.3	~ 0.1	~ 0.002
1	1000	5.548	29.9	~ 0.1	~ 0.001
5	50	5.548	26.8	~ 0.4	~ 0.02
5	100	5.548	18.9	~ 0.3	~ 0.01
5	500	5.548	8.46	~ 0.1	~ 0.002
5	1000	5.548	5.98	~ 0.1	~ 0.001
10	50	5.548	13.4	~ 0.4	~ 0.02
10	100	5.548	9.45	~ 0.3	~ 0.01
10	500	5.548	4.23	~ 0.1	~ 0.002
10	1000	5.548	2.99	~ 0.1	~ 0.001

Table 11. COMSOL simulations of 1st mode resonant frequency for different geometries of square Silicon Nitride membranes with no island mass. An assumption was made that the surface tension in the membrane is the same as that observed in the experimental data of tables 3 and 8, which may not be the case in actuality.

4.2 The Evolution of Our Proposed Method

As of this writing, we have not yet successfully measured the Quality factor of membranes because we do not have a suitable vacuum chamber in which to make precise Q measurements. Progress has been made in advancing our current experimental setup, while observations of the what happens to membranes when coated have somewhat changed our research directions. What follows is a description of the experimental approach and the observations made in our progression towards a Quality factor measurement.

The Michelson

Our initial idea for measuring the Q factor of the coated membranes utilized a miniature Michelson Interferometer. The method replaces one of the end mirrors with a coated membrane that could be actuated into resonance either with a fast piezo supporting the membrane frame or, externally, with an electrostatic actuation pin. The

oscillating membrane would cause the interference pattern to vary with the same frequency. A photodiode placed at the output port would detect the change in intensity over time as a result of the membrane motion. The FFT, and the ring-down time of the amplitude give us the Quality factor of the coated system.

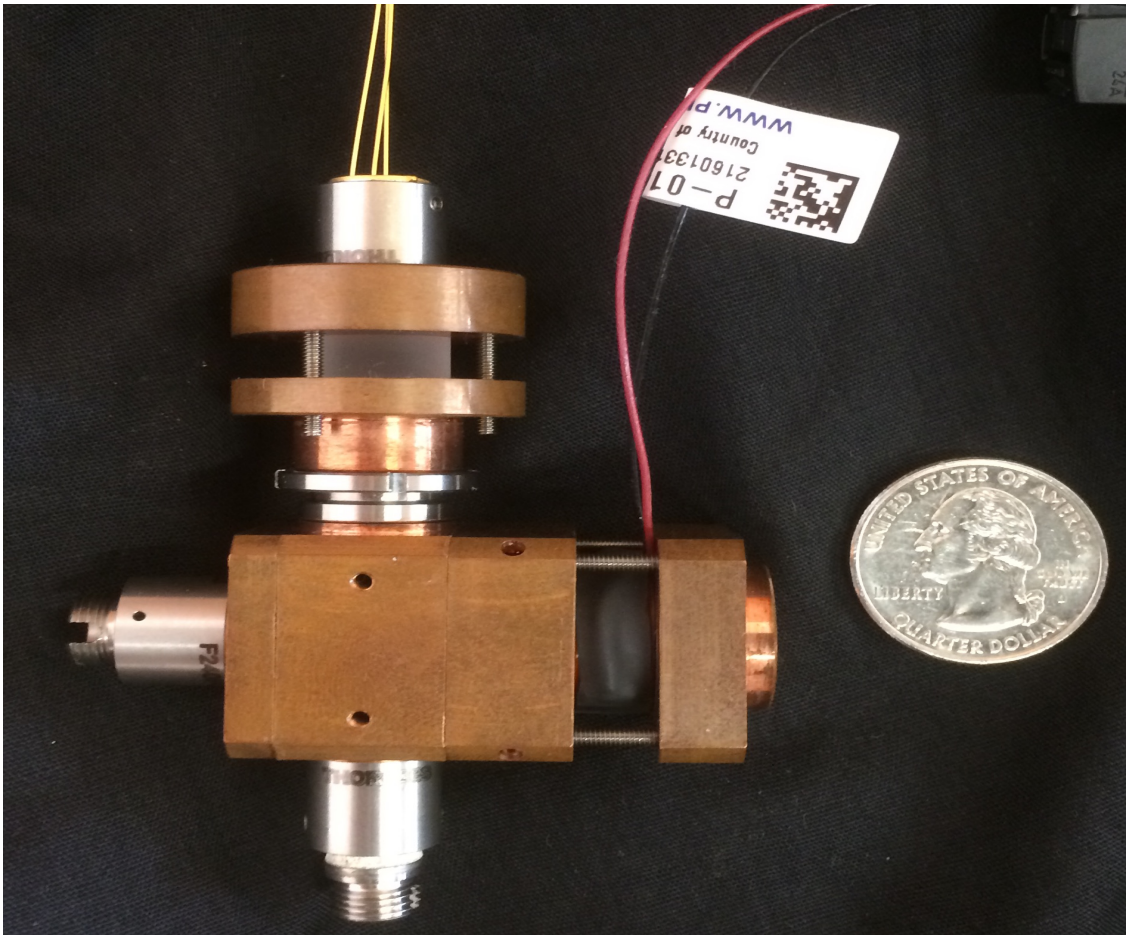


Figure 32. Photograph of the miniature Michelson Interferometer we initially planned for the Q measurements of membranes. Note the piezo in place (red and black wires lead to it) to actuate the motion of the membrane.

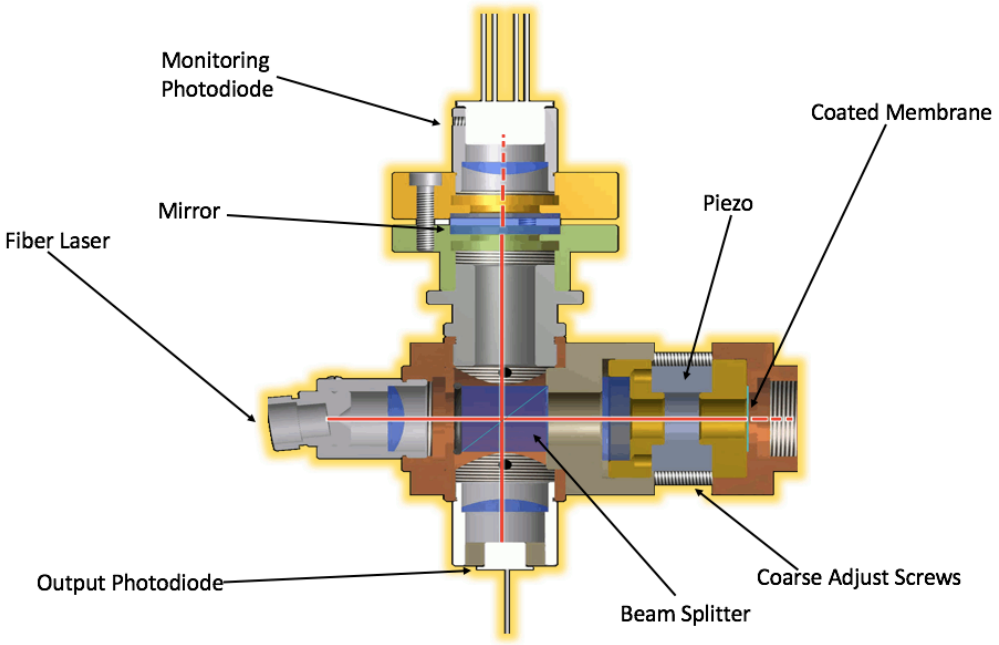


Figure 33. Schematic drawing of our miniature Michelson Interferometer. A fiber laser is attached on the left side to supply the beam that will be split at the center and diverted to the two ends. On one end is the coated membrane and on the other is a partially silvered mirror with reflectivity matching that of the coated membrane so that a good interference pattern will form at the output port where there is a photodiode. The coarse adjust screws can be used to change the length and axial orientation of the coated membrane arm.

The Weighted Membrane

We soon realized that the resonant frequencies for the Silicon Nitride membranes fabricated in the traditional way (figure 28) were too far out of the detection band. That led us to look for ways to lower them. The idea was to add a rigid mass to the membrane that would add inertia to the oscillation and lower the frequency. The effect can be seen using a simplified model of the mass and membrane as a mass held between two springs fixed at the ends.

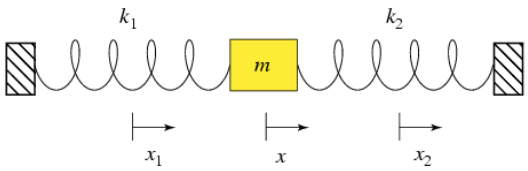


Figure 34. Simplified model to show how adding rigid mass to the membrane will lower the resonant frequency.

Here, the springs represent the membrane, the walls represent the rigid frame and the rigid mass is held in the middle. The system in figure 34 has a resonant frequency, (for equal spring constants) given by

$$f = \frac{2}{\pi}\sqrt{\frac{k}{m}} \tag{76}$$

A rough estimate of the mass required to bring a 1mm square 50 nm thick Silicon Nitride membrane into the frequency band of the detector to ~1000 Hz can be done as follows. The density of deposited Silicon Nitride is approximately 2.5 kg/m^3 and the volume that is deposited on the Silicon wafer is roughly (5mm x 5mm x 50nm) 1.25x10^{-12} m^3, which gives adds an inertial mass to the membrane of 3x10^{-12} kg. Assuming a first mode at 134 kHz, solving (76) for k we can approximate the membrane stiffness as ~ 0.13 kg/s^2. Setting the desired *f* to 1000 Hz, a mass of 5x10^{-8} kg is required. Considering that the density of Silicon is 2328 kg/m^3 a volume of ~2x10^{-11} m^3 is required. Assuming that the mass will have the same height (~100 micron) as the frame, we need an island that is ~2x10^{-7} m^2 area, roughly ½ mm on the side.

It has been difficult to make a reliable simulation in COMSOL of the membrane with embedded island mass. The difficulty presents itself in coordinating the two "Multi-physics" modules: *Membrane* and *Solid Mechanics*. The assumptions made for a membrane to remove the need for a very fine mesh disappear when the membrane is

joined to a larger rigid object. One attempted method to circumvent this problem was to use only the Membrane physics module and apply a square boundary in the center with dimensions equal to the island mass. We then instructed COMSOL to treat this region as rigid and with the mass value that would be present with the Silicon island. We arrive at a 1.5 mm Square window of Silicon Nitride membrane (with thickness 400 nm) and a 1.2 mm square Silicon island. 100 microns thick. The resonant frequencies for the first 4 modes are:

1^{st} mode 2.319 kHz

2^{nd} mode 3.723 kHz

3^{rd} mode 4.772.1 kHz

4^{th} mode 5.3667 kHz

which all closely follow the form above (75) in the mathematical expression relating the frequencies of a square membrane to the mode numbers. These results are not likely to be physically valid for our situation with a rigid island mass that does not store elastic energy. The resonant frequencies should not follow the same form as a function of mode number of a simple square membrane. The results found in the simulation, for the membrane with island mass much cannot be verified until further progress is made with a more accurate COMSOL model. For now, we rely on the observations made measuring the island membrane samples.

Weighted Membrane Prototypes

An island mass membrane has been manufactured by the team led by Shiuh Chao at National Tsing Hua University.

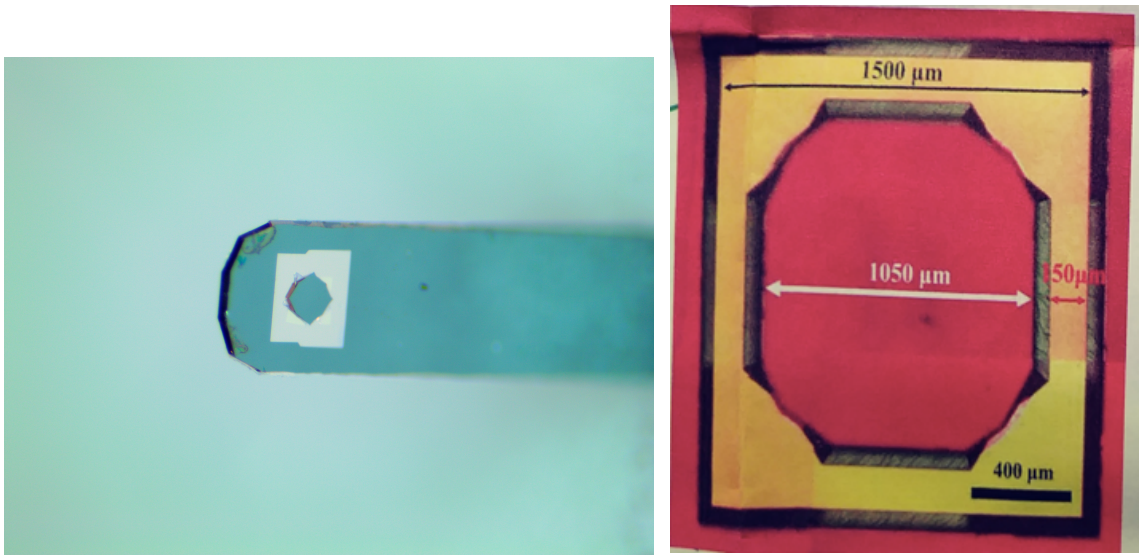


Figure 35. Photographs of two samples fabricated by National Tsing Hua University in Taiwan. The membrane on the left is 100 nm thick and holds an island mass of approximately 0.3 mm on the side, 100 µm thick. The membrane is framed within the "popsicle" shape made of silicon. On the right second membrane sample, 400 nm thick, designed to further decrease the resonant frequency with a larger island mass of approximately 1mm square.

Optical Lever Readout

While the addition of the island mass to the membrane may allow us to make Q measurements in the detection frequency band (10 to 1000 Hz) it makes the Michelson Interferometer technique less useful. We also need to measure the tilt mode that cannot be done in a Michelson Interferometer.

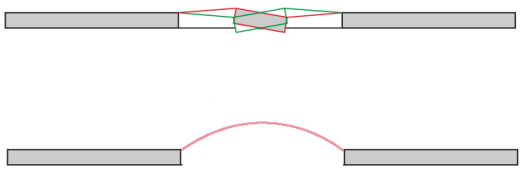


Figure 36. Differences between membrane response to actuation. The top image shows the island mass rocking back and forth. This mode cannot be measured in the. The lower image is the simple first mode shape of a membrane with no island mass.

Because of the complicated motion of the membrane with an embedded island mass we decided to use the optical lever technique to identify the resonances and measure ring-down of the samples. The setup will be very similar to that used in the GeNS technique pictured in figure 25. The details of this experimental technique are given in the following sections. See the figure below (figure 37) for a general setup overview.

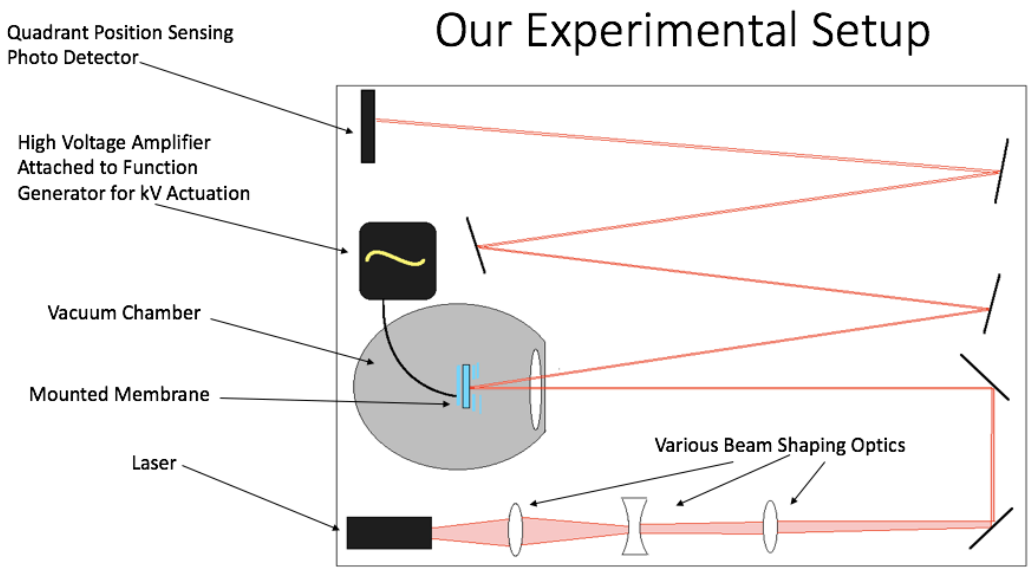


Figure 37. Schematics of the experiment. A laser beam is collimated into the narrowest and least diverging shape possible. The beam is incident on the sample ideally mounted in an ultra-high vacuum chamber. Feasibility studies are in air. The membrane is actuated by a strong electric field either in the form of white noise, a frequency scan or an ultra-fast pulse. Information on the motion of the sample resides in the motion of the reflected beam which is detected by a quadrant position sensing photodiode (QPSPD). The QPSPD voltage is measured in an oscilloscope with software that performs the FFT to obtain the spectrum of resonant frequencies.

4.3 Gluing the Membrane to a Stage

The coated membrane and frame must be held during the Q measurement in a way that reduces the amount of frictional losses between the sample and the holding stage as well as the support recoil losses. For low frequency measurements, the stage

should then be isolated as much as possible from the seismic environment possibly on an optical bench.

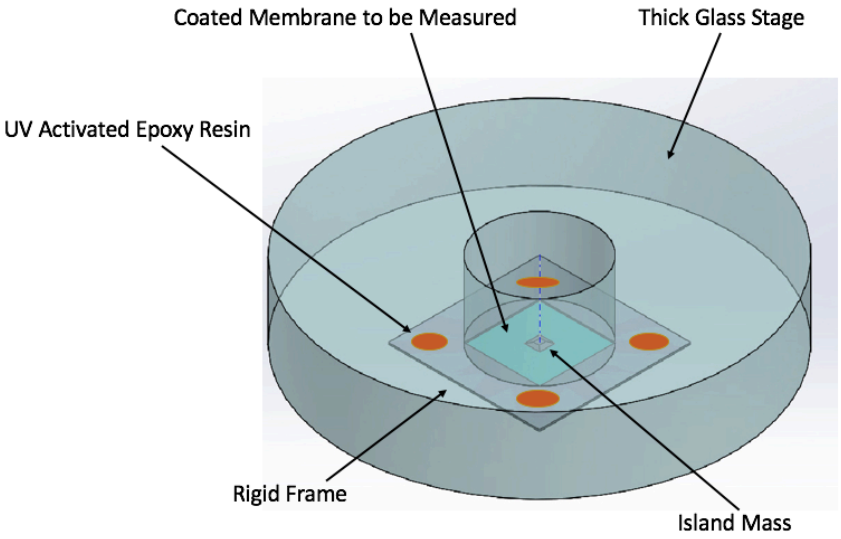


Figure 38. View of the glass stage and the framed membrane sample. This view shows where glue connects the sample to the stage. The gluing to the stage will not lead to the same losses as in the clamped cantilever because much of the membrane recoil is already absorbed by the rigid frame, the glue is very thin and stores an extremely small amount of elastic energy. The glass is much thicker than the sample and can be safely clamped on the bench without fear of oscillation energy losses.

One could be worried that we are just passing the buck from clamping to gluing to the stage, but an estimate of the amount of elastic energy that, due to recoil, can be stored in the glue between the frame and the stage shows that it is negligible. The stage itself is much more massive and will receive very little impulse and it cannot cause frictional losses even if simply clamped to the bench.

Using the same kind of analysis as in (50) through (57) which illustrated how a very thin layer of poor Loss Angle Optical Coating was able to affect the overall Loss Angle of the entire mirror, we can treat the membrane, frame and glue as a series of coupled oscillators and show that the energy lost outside the coating is negligible. The expression for the total stored elastic energy of the combined system

is given by

$$E_{Total=}\frac{F^2}{2}\left[\frac{1}{k_{Membrane}}+\frac{1}{k_{Frame}}+\frac{1}{k_{Glue}}\right] \quad (77)$$

where F is the force applied on the coated membrane by the electrostatic actuator. We have already seen that the stiffness of the membrane, from the rough estimate following (76), is on the order of 10^{-1} kg/s^2. The spring constant of the frame, which is a crystalline Silicon wafer is very high and can be gathered from the expression in (58). The area of the frame is approximately 8 mm square, the thickness around 100 microns and the Young's modulus for Silicon is ~170 GPa. This yields a k_{Frame} on the order of $7x10^9$kg/s^2. The expression for stiffness of (58) suggests the use of a glue with very low viscosity so that the layer will be as thin as possible. We also want the largest Young's modulus. A good balance is found in the ultra-violet activated epoxy resins that are used in dental practices. These adhesives may have thickness layers as little as 10^{-6} m and possess a Young's modulus ~1 GPa. Applying the resin to the entire area between the frame and the stage will give k_{Glue}~$4x10^9$. From this analysis, we can see that the ratio of elastic energy stored in the membrane compared with that in the glue is approximately 10^9 to 1, and therefore we need not worry about "clamping" losses in this configuration. Similarly, it can be shown that clamping of the stage to an optical mount causes no problems.

Glue Tests

We performed preliminary tests with samples of the UV activated epoxy resins and found that it is difficult to achieve a cure when the UV light is shined through the glass. in the long term, we want to procure fused silica substrates that readily transmit

UV. We must also be careful to keep the glue from overflowing. With such low viscosity, this may be difficult.

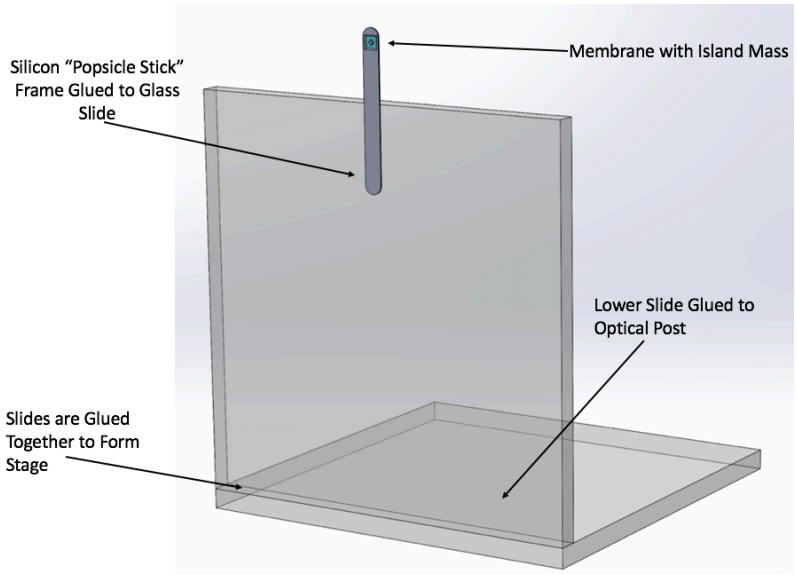


Figure 39. Illustration of the setup for the "popsicle stick" shape of the first sample. The length of stick that is not glued is exaggerated in the picture. We want to keep the length short to minimize cantilever modes in the response. This geometry is not ideal, it is used to practice with the UV activated epoxy resin.

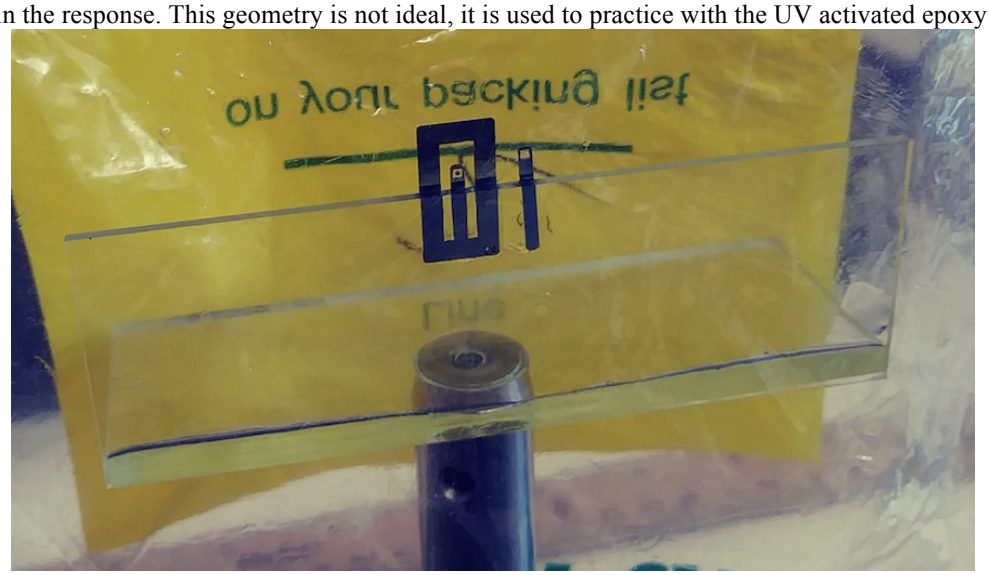


Figure 40. photograph of two "popsicle stick" samples mounted with UV activated resin to a thick glass slide. Note the island mass in the sample on the left, and none in the sample on the right. The membranes are extremely fragile and can be shattered easily. The sample on the right was damaged by the electrostatic actuation pin that was brought too close and punctured the membrane.

4.4 The Vacuum Chamber

Oscillators are damped by air, leading to underestimation of the actual Q factor. The oscillator must be isolated in high vacuum.

We will be employing a turbo pump connected to an ultra-high vacuum chamber. We have not been able to procure all the components for a satisfactory chamber but tested a turbo pump, and its roughing pump.

Without a fully operational vacuum chamber we are not able to make accurate measurements for the Q of coated membranes. However, we may still test the basics of our experiment as well as validate the simulations made to predict the resonant frequencies. These observations will help find the frequencies to be studied with the system in vacuum.

4.5 Electrostatic Actuation

Exciting the coated membrane into its resonant modes will be achieved by creating an oscillating electric field near the sample. Since both the coating and the membrane are dielectric materials they will respond to the electric field with a force proportional to the area over which the field is applied. This field will drop in magnitude rapidly as we move the sample away from the source. We plan to use a localized point source in the form of a spherical metallic pin head connected to a high voltage amplifier to “pluck” the membrane into excitation.

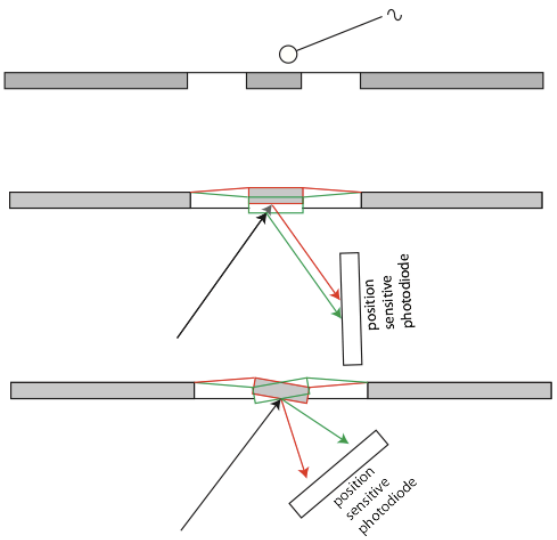


Figure 41. Illustration of the membrane with island mass being excited into resonance by an electrostatic actuating pin (wand at the top) and the resulting motion of the system that would be captured by a photodiode. The different orientations of the photodiode are just to show that we will have control over this parameter and that different orientations will give a greater amplitude for this or that detected signal.

In the GeNS technique for measuring the Q of a coating deposited onto an approximately 1mm thick fused silica disc, an electrostatic field produced by an electrode at ~1kV/m is used to excite the disc into its resonant modes. The actuation is related quadraticaly to the field, which from a pin, decreases with the square of the distance, as well as from the dielectric constant. Silicon Nitride has dielectric constant ~7 while fused silica's dielectric constant is ~ 4 which may help for a naked membrane. As an indication of the force the membrane will feel due to actuation (yet differently shaped actuators will give different forms for the field), the derivation of the force on a dielectric slab within a parallel plate capacitor (Griffiths, *Introduction to Electrodynamics,4th ed.*) is given as

$$F = -\frac{\epsilon_0(\epsilon_r - 1)w}{2d}V^2 \tag{78}$$

where ϵ_0 is the permittivity of free space, w is the width of the dielectric slab, d is the thickness of the slab as well as the spacing between the plates, V is the applied electric potential across the capacitor and ϵ_r is the dielectric constant.

The function generator that we are using has a maximum output amplitude of 10 Volts (20 V peak to peak) which we boost with a transformer. To measure the gain of the ignition coil transformer, we placed a 20,000:1 voltage divider between the output and ground and probed the resulting voltage on an oscilloscope.

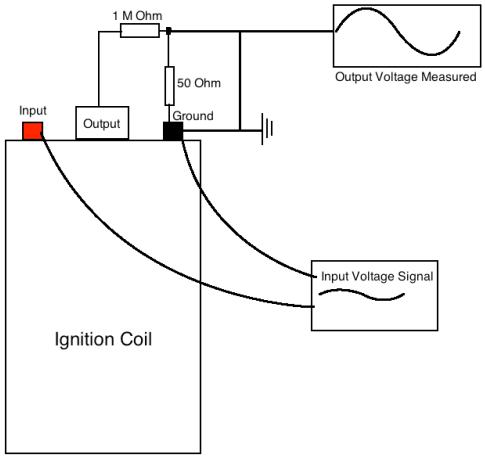


Figure 42. The voltage divider that was used to reduce the output of the coil roughly by a factor of $\frac{50\ \Omega}{1{,}000{,}000\ \Omega}$ or $5\text{x}10^{-5}$ to avoid damaging the oscilloscope when testing the gain.

Using Kirchhoff's law for voltage drops around a loop we have that

$$V_{Output} - I\ (1M\ \Omega) - I(50\ \Omega) = 0 \tag{79}$$

and since the current is constant, the voltage measured by the oscilloscope across the 50 Ohm resistor is the output voltage from the coil multiplied by $5\text{x}10^{-5}$. Below, is the gain data for this ignition coil as a function of frequency.

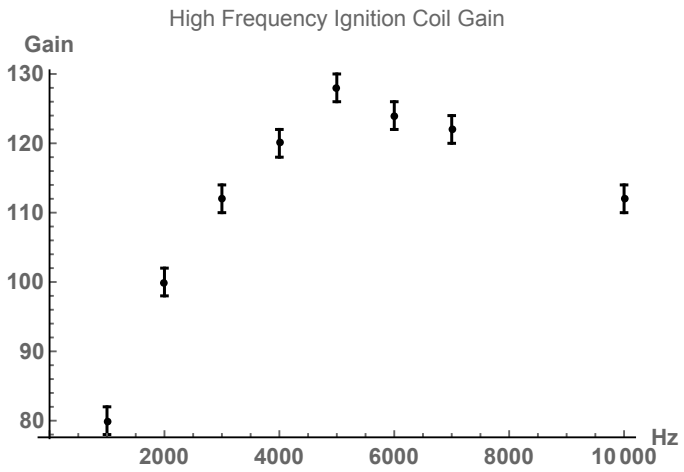


Figure 43. Plot of Gain versus frequency for the ignition coil. The function generator was delivering 20 volts peak to peak the error bars on the Gain are +/- 2.5. The ignition coil is capable of generating ~1 kV in the frequency range of ~2 to 10 kHz which corresponds to oscillation frequencies ~4 to 20 kHz, about the range at which we expect the membranes with the rigid island masses to resonate.

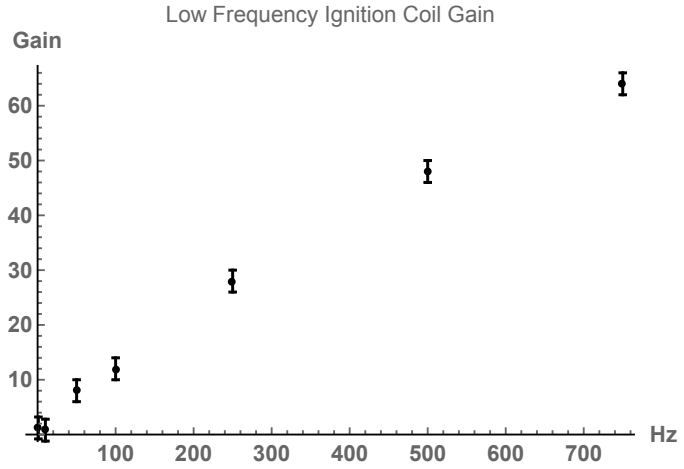


Figure 44. In the low range of frequencies, the amplification of the ignition coil drops off steeply. A ~500Hz signal excites a resonant mode ~1000Hz. At that frequency, the output will be amplified by a factor of ~50.

The effect of an oscillating electric field on a dielectric material is always attractive, therefore an electric excitation frequency will induce a mechanical response at twice that frequency.

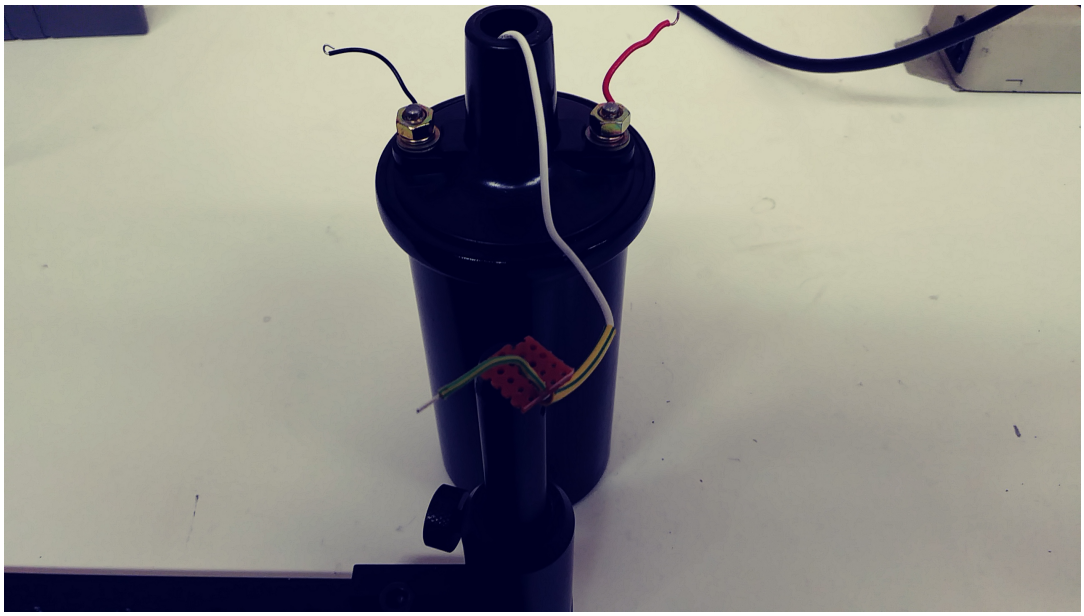


Figure 45. The transformer used, an automobile ignition coil. The two leads, red and black, will be connected to a function generator to receive the input signal. The output voltage is collected across the white wire and ground.

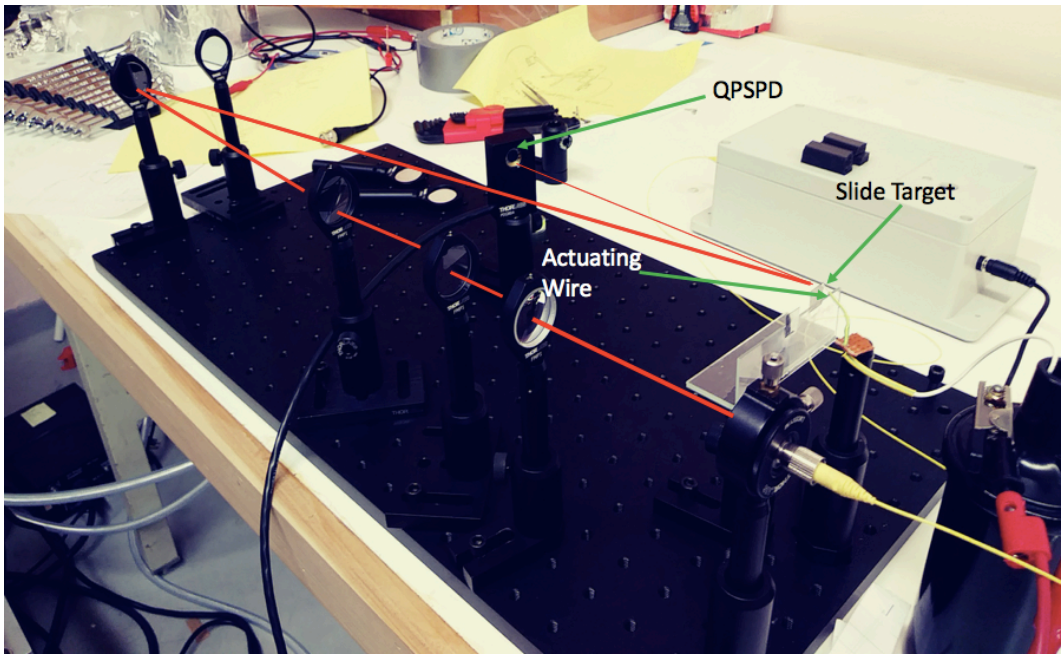


Figure 46. Optical setup used to test the optical lever with the ignition coil actuator acting on a thin glass slide mounted on a stage. The beam path is drawn in red.

The Quadrant Position Sensitive Photodetector

The QPSPD we are using to detect the motion of the optical lever light spot is a ThorLabs PDQ80-A Segmented Quadrant PD. It consists of four photodiodes arranged in quadrants and wired to a trans-impedance amplifier circuit. The relative intensity changes on each quadrant is used to determine the motion of the light spot if it is centered to the crosshair. Smaller spots give more signal/ mm, with the drawback of more baseline drift. The detector is recommended to be used with spot sizes in the range of ~1 to 4 mm and we have found that this agrees with our observations.

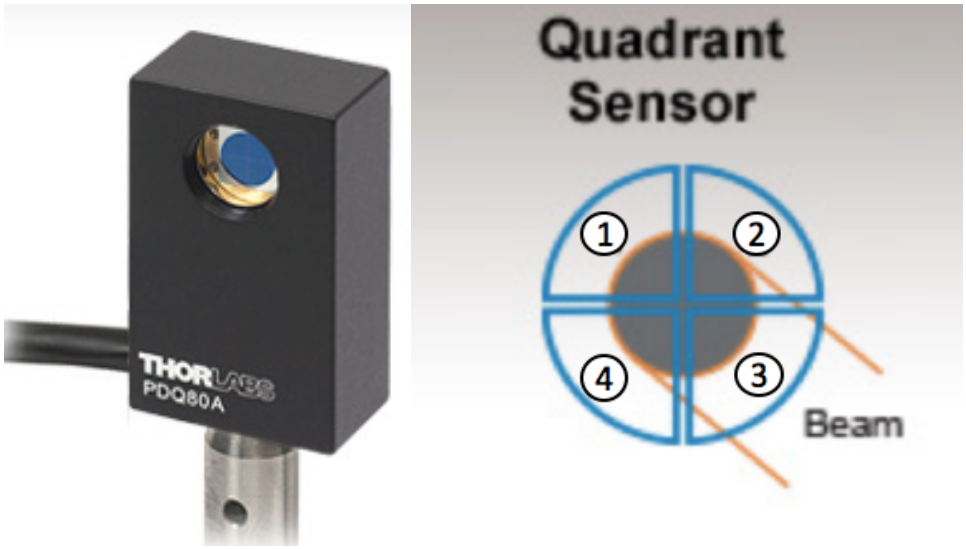


Figure 47. The QPSPD used as well as a diagram showing the four photodiode quadrants the make the "face" of the detector. Images from thorlabs.com

$$X = \frac{(Q2 + Q3) - (Q1 + Q4)}{(Q1 + Q2 + Q3 + Q4)} = \frac{X_{Diff}}{SUM}$$

$$Y = \frac{(Q1 + Q2) - (Q3 + Q4)}{(Q1 + Q2 + Q3 + Q4)} = \frac{Y_{Diff}}{SUM}$$

Figure 48. Equations used to extract the position signal. Qi is the measured current from the i' th quadrant face at an instant in time.

We observed in our characterization measurements that the detections of actuated oscillatory motion in the samples have the largest magnitude when the spot on the detector is centered. We also observed that if the spot on the detector face is too large, it will not yield a large signal when the spot moves.

If the spot size incident on the detector changes size dramatically during a measurement, the amplitude of the peak will oscillate. This will add further uncertainty to the ring-down Q measurements and should be avoided. We will arrange the orientation of the detector to be perpendicular to the incident beam. We will also use the smallest spot on the sample as possible since a large spot on the sample will result in a time changing spot size with respect to the change in curvature of the various oscillatory modes (figures 49 and 50).

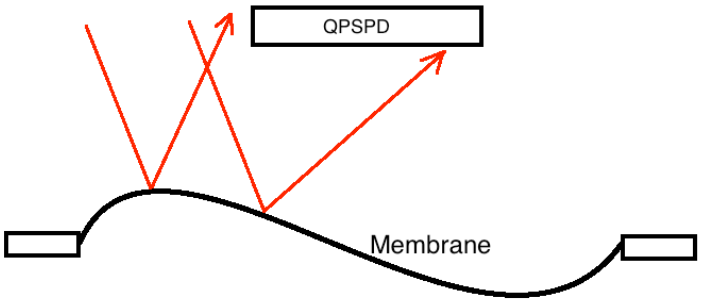


Figure 49. Drawing of a curved mode for a square membrane being measured by an incident beam. The large incident spot on a changing curved surface will diverge making the spot shrink and grow more on the detector.

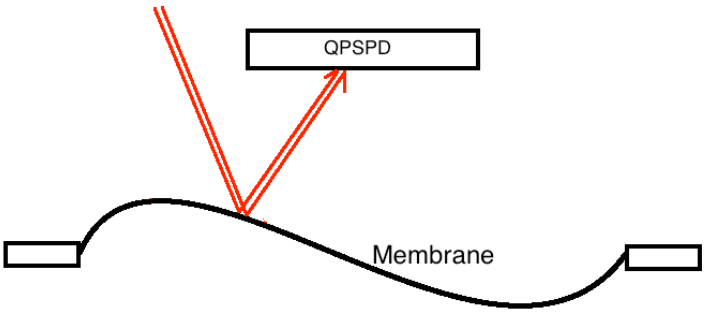


Figure 50. A small spot size, ~ 2mm in width, is also best for the position sensitive photo-detector to capture the motion.

While we have observed that changing the spot size on the detector has a greater effect on the amplitude of the peak detected by the QPSPD than the related change in the lever arm length due to moving the detector to the smaller spot size location, we may need a lever arm at least ~1 meter in length to amplify small oscillation amplitudes. The requirement of a minimum lever arm length and small beam spot sizes on both the sample and the detector complicates the choice and configuration of lenses that will be used. The lenses that are put in place to achieve the requirements must be arranged between the laser and the sample to be measured. Placing them after the sample will greatly decrease the sample's motion that is registered by the axial motion of the beam. Ideally, we would use one lens with a very long focal length to obtain a beam profile that diverges very slowly, giving us a wide range of lengths at which we can obtain a small

spot size. Very long focal length lenses (longer than 2000mm) are quite expensive and so it is desirable to find a configuration of multiple more affordable, smaller focal length lenses that can achieve the same result.

Experimental Characterization of the Excitation System

To characterize our electrostatic actuating system, we performed a series of experiments using two glass microscope covers coated with Aluminum. The glass samples are much more robust and cheap than the membrane samples and this allows many adjustments without fear of destroying them. Experiments were performed to measure the glass slides' responses to the electric field at multiple frequencies. An optical lever was constructed to make the measurements (figure 45). We used a 635-nm laser focused by a series of lenses. The laser was incident on the sample being measured and then reflected to the QPSPD approximately 0.6 meters away. The two samples were measured separately and constructed with different geometries (figure 50) so that we could measure different first mode resonant frequency values.

We optimized the detection amplitude as a function of beam spot size, lever arm length and distance of the actuator from the samples. All of this information is important for the next researchers to carry on the Q measurements in vacuum.

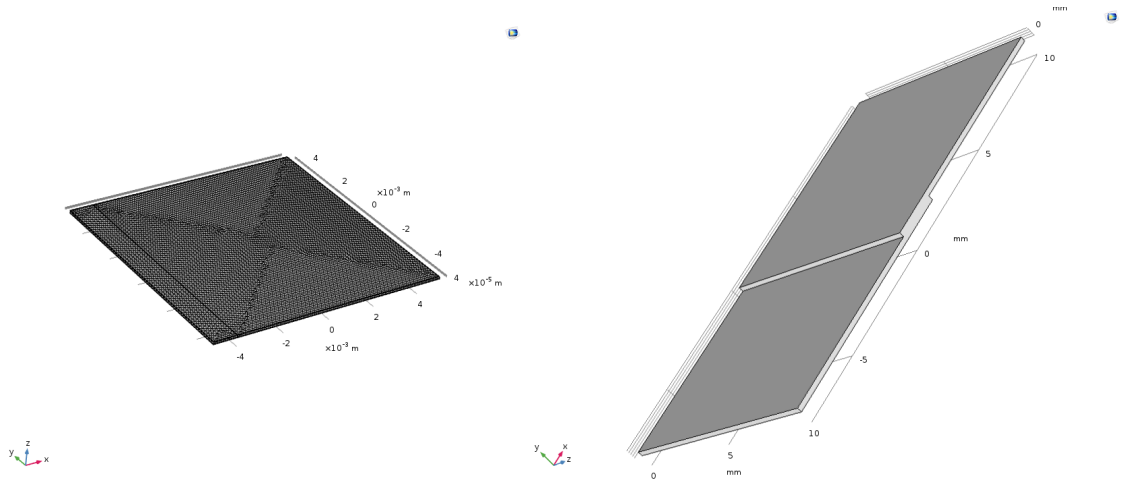


Figure 51. COMSOL models constructed to represent the two glass samples used to characterize the electrostatic actuating system. On the left is the mesh covered model for the 10mm square, .2 mm thick slide glued to the stage along a rectangular area 1mm by 10mm. On the right side is the "double slide" model which represents a sample with two slides glued to each other and then glued to the stage on a rectangular area of 5mm by 10mm.

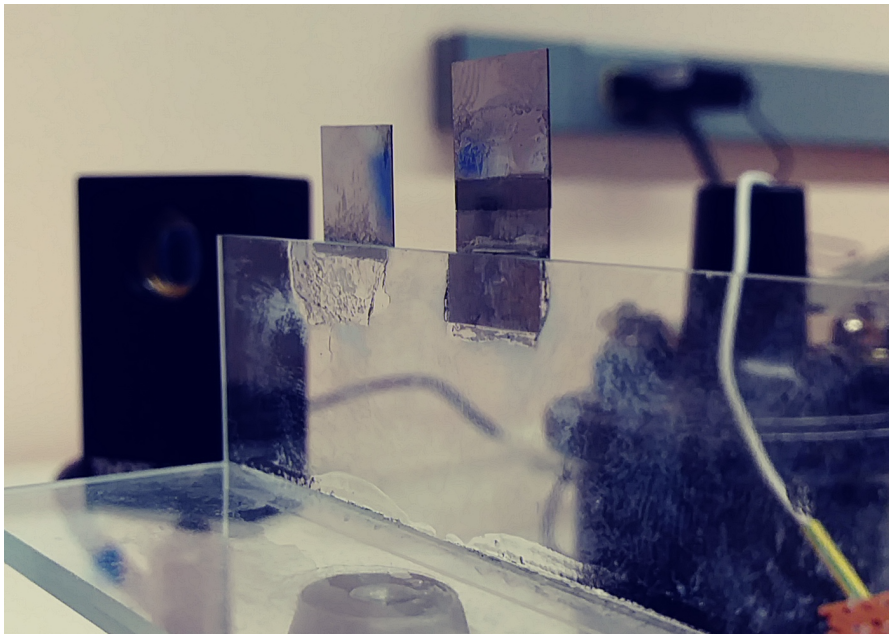


Figure 52. Photograph of the two glass samples. The "single slide" is on the left and the "double slide" is on the right. Both are glued with low viscosity adhesive to a 2mm thick glass stage. The samples are not pristine and are only being used to make rough characterization statements about our apparatus.

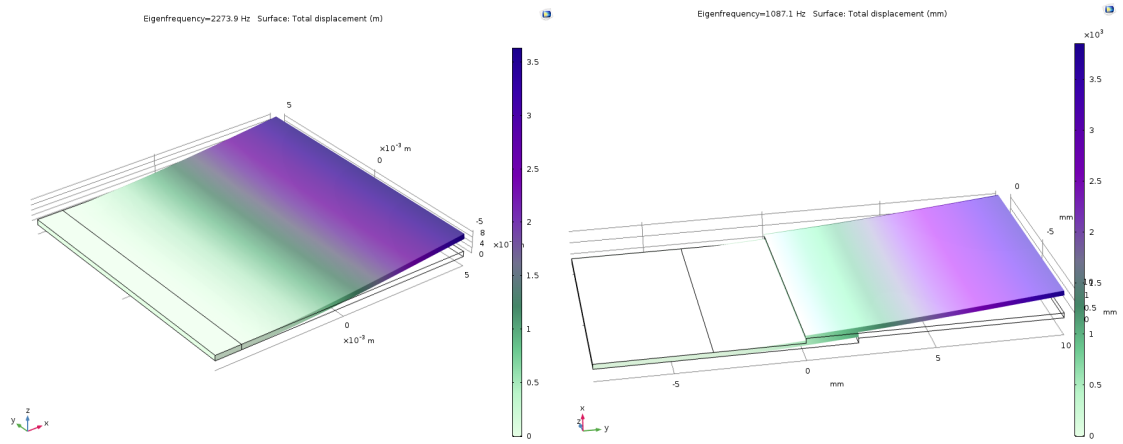


Figure 53. The first mode shapes for the two glass samples modeled in COMSOL. The "single slide" on the left has a theorized 1st mode frequency 2273.9 Hz and the double slide has an expected 1st mode frequency of 1087.1 Hz.

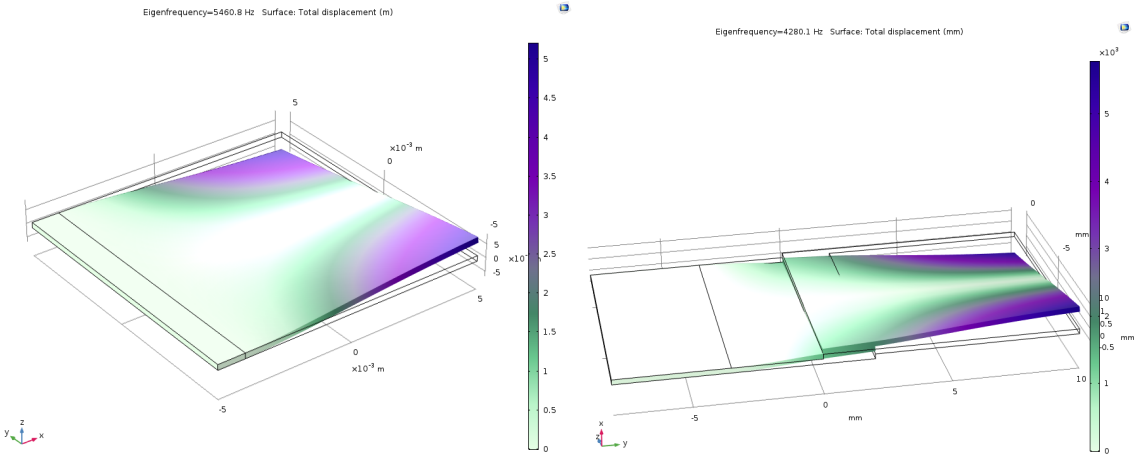


Figure 54. The COMSOL simulated 2nd mode frequency shapes and values for the two samples. The 2nd mode for the "single slide" has a simulated value 5460.8 Hz and the "double slide" has a value 4280.1 Hz.

The actuating wire was placed as close as possible to the sample without touching, approximately a distance of .2 mm. As expected the response is optimized when the wire is as close as possible to the material to be excited and in the location of largest oscillation amplitude. In figure 54 we show the orientation optimized for the first mode of this sample.



Figure 55. photograph of the actuating wire placed just along the top edge of the "double slide" sample. This orientation is ideal to excite the first mode and provided large amplitude oscillation response.

The data acquisition was made with a Picoscope model 2000B digital oscilloscope connected to a laptop computer. We analyzed the measurements using the FFT function of the program. It was observed that interference from the fluorescent lights in the laboratory affected the measurements. Lights were kept off during data runs.

To locate the frequency values for the first mode of the samples we thumped the stage and watched the broad peaks emerge. The peaks are broad because the air is reducing the quality factor.

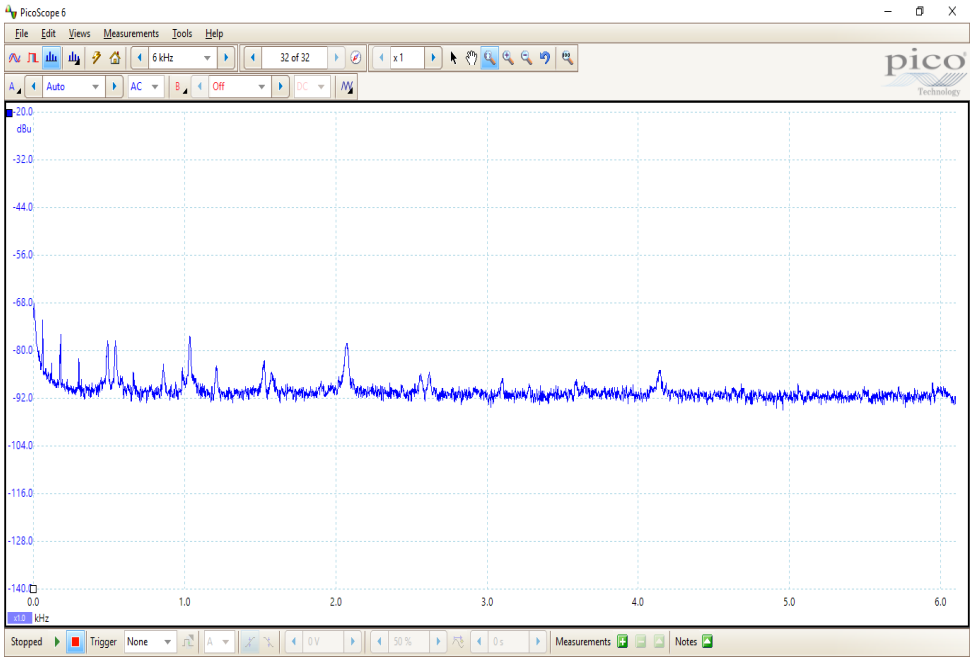


Figure 56. The graph shows the "double slide" sample being mechanically excited by a quick series of thumps on the stand with a wooden stick. Note the width of the peaks and the first mode around 1080 Hz which is close to what expected from the COMSOL simulation in figure 48. Many mechanical setup resonances also show up, but those will not be excitable electrostatically.

Once the range of frequencies was found for the 1st mode, the electrostatic actuator was used to excite individual resonances.

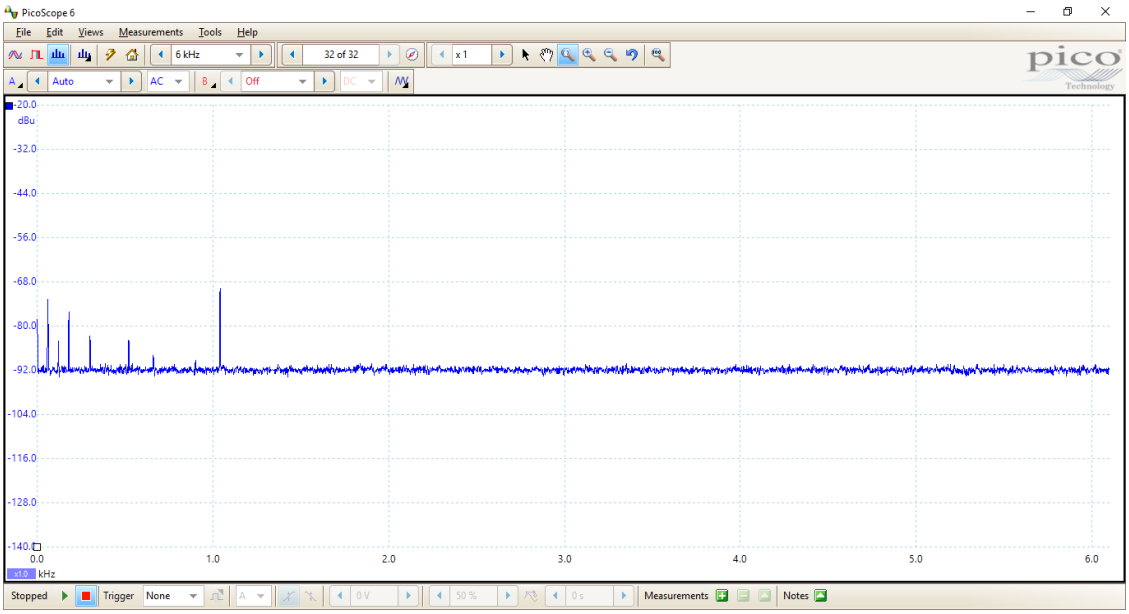


Figure 57. The FFT data that shows the ~1kHz peak for the first mode of the "double slide" sample actuated electrostatically.

In figure 56, the electrical actuation frequency being used is 520 Hz. From the plot in figure 44 of the amplification due to the coil is ~ 50, the electric voltage on the electrode is ~ 500V. This is half the value we expected we would need, based on what is used in the GeNS measurements.

An attempt was also made to excite the second mode for the "double slide" sample which should be around 4000 Hz according to the simulation and the "thump" driven data in figure 55. Yet, we were not able to excite that mode with the actuating wire. We moved the actuating wire to an orientation that would be more conducive to exciting that mode shape but still proved unsuccessful.

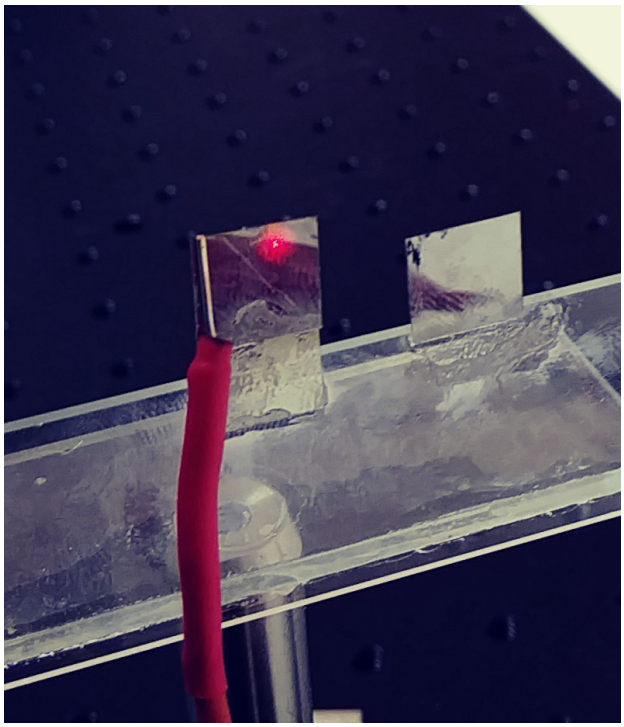


Figure 58. Photograph of the electrode orientation attempted, unsuccessfully, to drive the second resonance in the "double slide" sample. It should be noted that the laser spot was directed to the corner to increase the detected amplitude of oscillation.

To prove that we detected the actuation of the sample and no other resonances, we performed controlled tests with the laser, actuation signal, and target in various combinations. The results of which are given below.

The FFT data of the QPD shows no signal when the laser is turned on but blocked from the detector, both with a 520 Hz actuation signal on the oscillator and without actuation signal. Figure 58 shows the mechanical modes of the stand, excited by seismic and acoustic noise, as seen by the laser beam bouncing off the unexcited mirror.

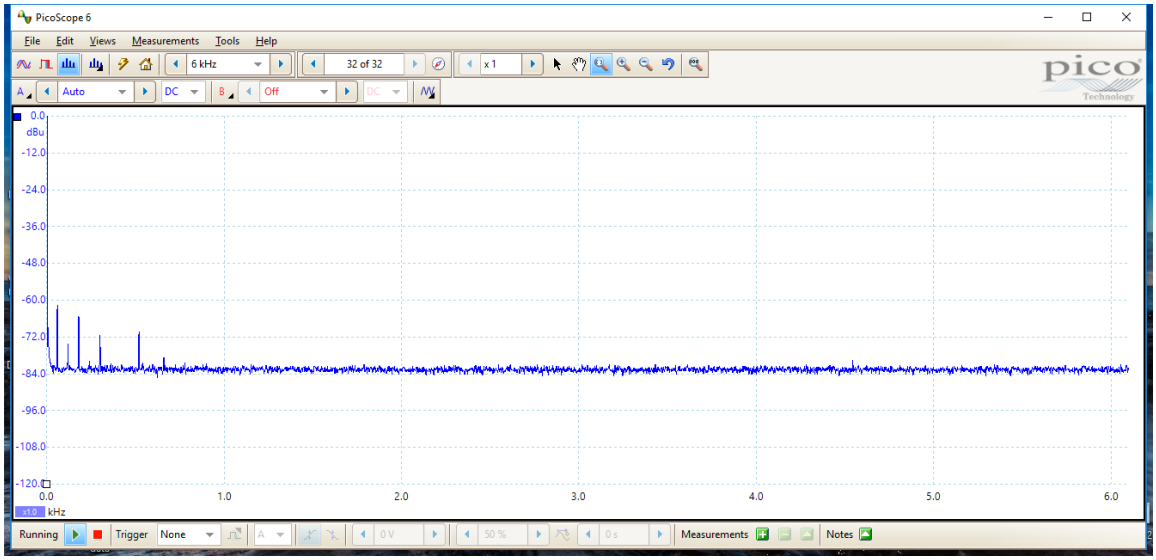


Figure 59. The FFT data when the laser beam is incident on the sample and reflecting the laser onto the detector but the actuator is moved away from it. The actuator signal is at 520 Hz. Note the peaks of the mechanical vibration mode of the stands in the low frequency when there is laser light on the detector as well as the peak at 520 Hz which is an electrical signal picked up from the cables of the actuation signal. Not being at twice the excitation signal, the 520 Hz peak cannot be a resonance signal.

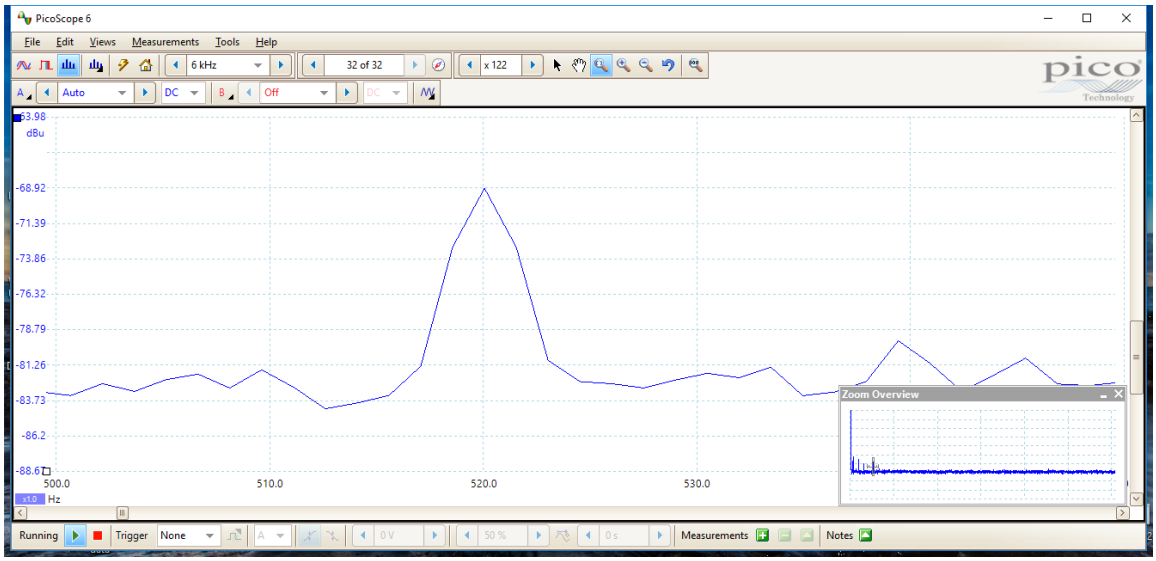


Figure 60. Zoom in to the data of figure 59 showing that the electrostatic signal is precisely at 520 Hz which the frequency of the signal being amplified by the ignition coil.

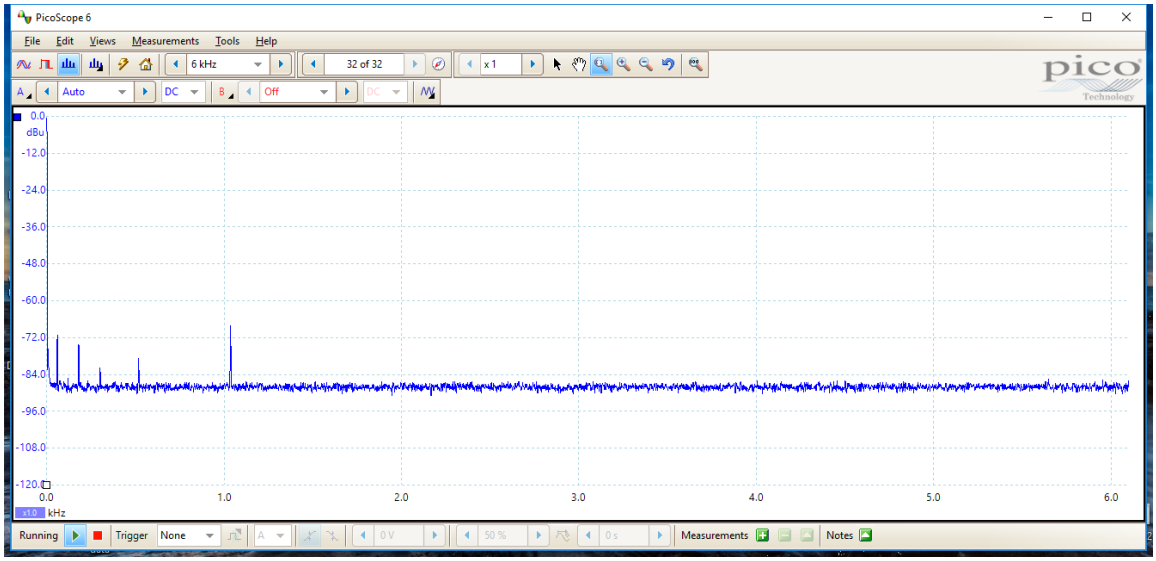


Figure 61. Peak at 1040 Hz when the laser is incident on the glass sample being electrostatically actuated with a Voltage at 520 Hz. At the beginning of each ring-down measurements, the electric field signal is cut off. Compare this figure with 54 when there is no actuation on the sample.

We also measured the 1st mode frequency range for the "single slide" sample. To characterize the "sweeping" capabilities of our function generator to locate a frequency range for a material's resonant modes, we swept through a range around the center of the "single slide" sample's peak.

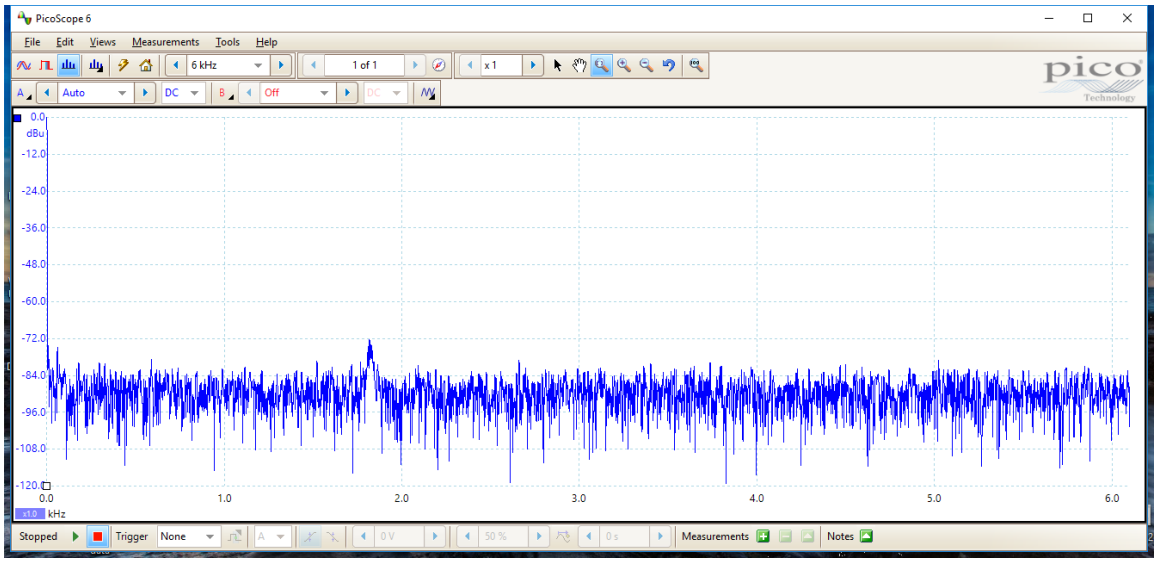


Figure 62. Broad peak detected when sweeping through a range of frequencies. This data is for the "single slide" with a sweep from 870 to 950 Hz in 330 ms. The data was averaged over ~5 minutes. The broadness of the peak is due to sweeping too quickly through the frequency range. The damping time in air for these samples was found to be around 50 ms. Sweeping through a 100 Hz range in 330 ms means we are only on resonance for .3 ms. This is not enough time to drive the oscillation to the full amplitude.

Data was collected to make a rough measurement of the "single slide's" Quality factor in air. This is, of course a very rough measurement because the sample is suffering many losses due to the air, yet it shows that we will be able to carry out much better measurements once we put the samples in a vacuum chamber.

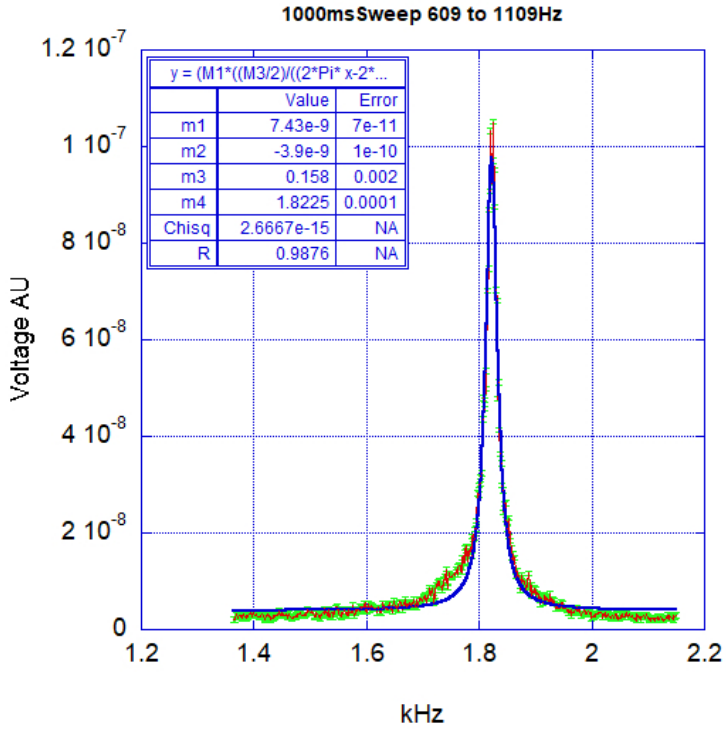


Figure 63. FFT data from the Picoscope, brought into KaleidaGraph and fitted with a Lorentzian curve. The blue curve is the fit to the data in red. The size of the green error bars was based on the plot of the residual between the fit and the data. The parameters of the fit, m1-m4, are related to the parameters of the Lorentzian curve that is used to calculate the Q.

$$Fit = A\,\frac{\frac{\Gamma}{2}}{(2\pi f - 2\pi f_0)^2 + \left(\frac{\Gamma}{2}\right)^2} - d \tag{80}$$

Equation 80 is the Lorentzian curve used to fit to the data taken during a 1000 ms sweep from 609 Hz to 1009 Hz actuation frequency which resulted in a peak around the response frequency of ~1820 Hz. The parameters, A, Γ, f_0 and d correspond to the found fit parameters in figure 63. The parameters used to determine the Q are Γ~0.158, and f_0~1.8225. The Q can be extracted from the data by calculating the width of the curve and dividing that from the peak's central frequency. The width was calculated solving

$$\frac{1}{2} = \frac{\frac{0.158}{2}}{\left(2\pi f - 2\pi\,(1.8225)\right)^2 + \left(\frac{0.158}{2}\right)^2} \tag{81}$$

for the frequencies, f which were found to be 1.7605 and 1.8845 kHz. These are the boundaries of the width, which therefore has a value of 0.124 kHz. Then, using equation 49, this gives $\frac{1.8225}{0.124} = 14.7$ for the measured Q value. This is very low compared with the Q ~ 10^7 for glass and is due to the fact that our samples are being damped down by air and the glue.

The sweep time for this type of measurement is very important. During ring-down measurements we observed the damping occurring in a time scale of ~50 ms. Sweeping 1000 ms across a range of 500 Hz only allows us to spend .5 ms at each frequency. We will need to extend the sweep time by a factor of ~100.

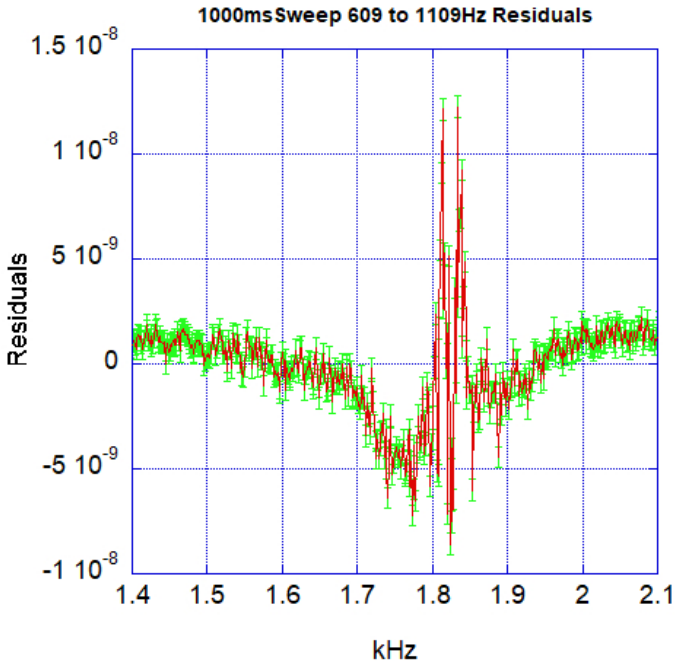


Figure 64. Plot of the residuals between the data of the 1000 ms sweep through frequencies around the first mode of the glass sample and the fitted curve. The residual plot was used to determine the value for the error bars in figure 63.

It is important to measure as many modes as possible for our samples because the Quality factor is frequency dependent. We need to establish a trend of Q versus frequency as near to the frequency range of interest for the GW detectors so that we extrapolate or interpolate as little as possible to make accurate characterization of the detector's thermal noise. This requirement motivated us to construct a weighted membrane with low-frequency first mode, and a more effective actuation system to excite and measure excited modes.

An actuating comb is a more effective electrostatic actuator than a bare wire. The observed resonances have a much better signal to noise ratio.

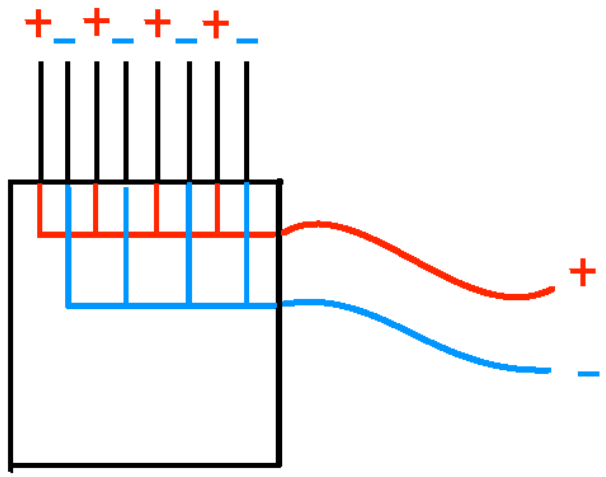


Figure 65. The electrostatic comb creates a much larger force at the same voltage than a single wire. The teeth are set at plus and minus potential in alternating series. It extends the area over which the force is applied. The strength falls off, rapidly if the distance of the comb from the dielectric is greater than the periodic space between the comb's teeth.

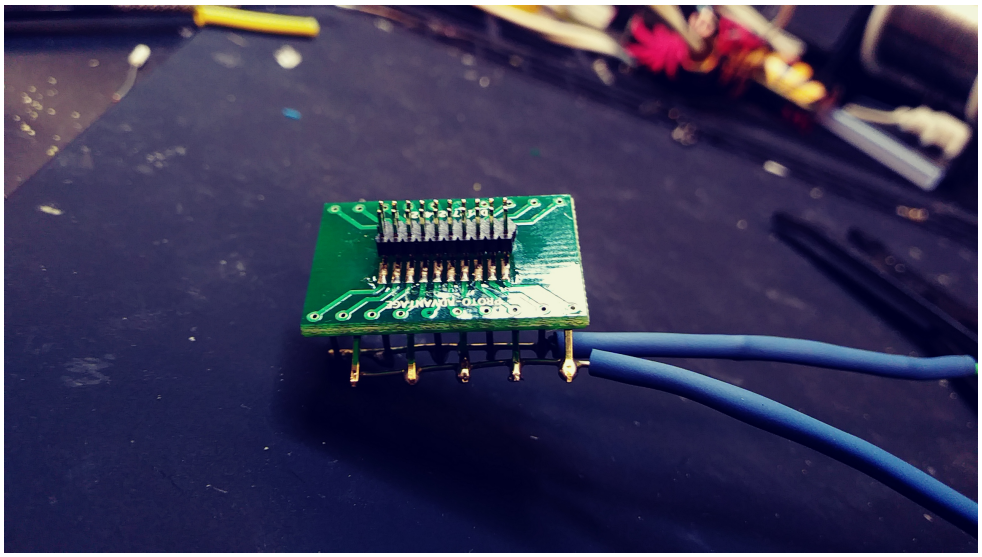


Figure 66. Photograph of the actual electrostatic comb we built to excite the samples.

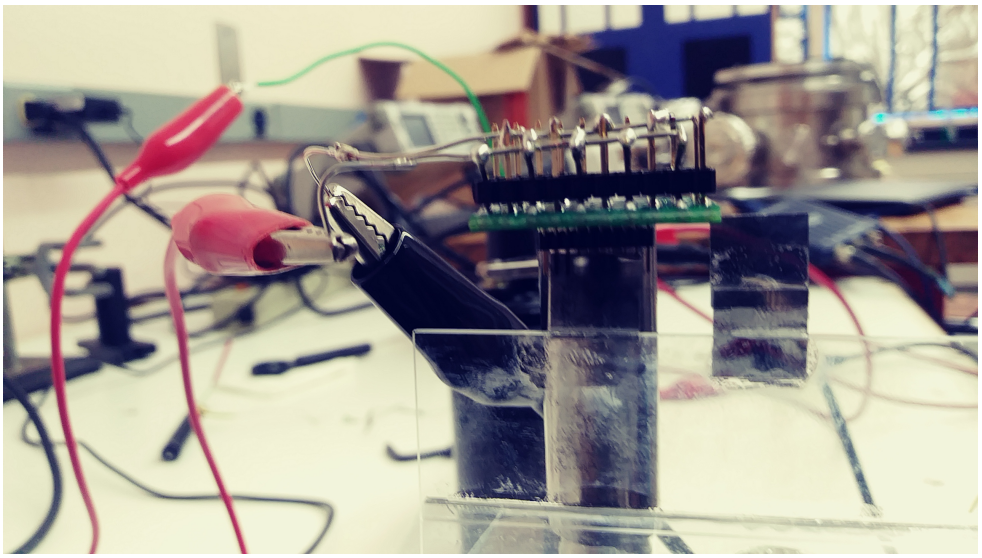


Figure 67. Comb positioned just behind the "single slide" aluminum coated glass sample. This comb drives oscillation with amplitudes that are ~2 times greater than what achieved with the wire. In the photograph, the teeth are barely visible through the slide. The space between the plane of the comb's teeth and the slide is approximately 0.1 mm, difficult to achieve with the current setup. The spacing between the teeth themselves is ~.5 mm.

With the frequency comb in place and activating our sample, we were able to drive a higher order resonant mode for the "single slide" sample. We were also able to perform a "ring-down" measurement on both the first and one higher order mode of the same sample.

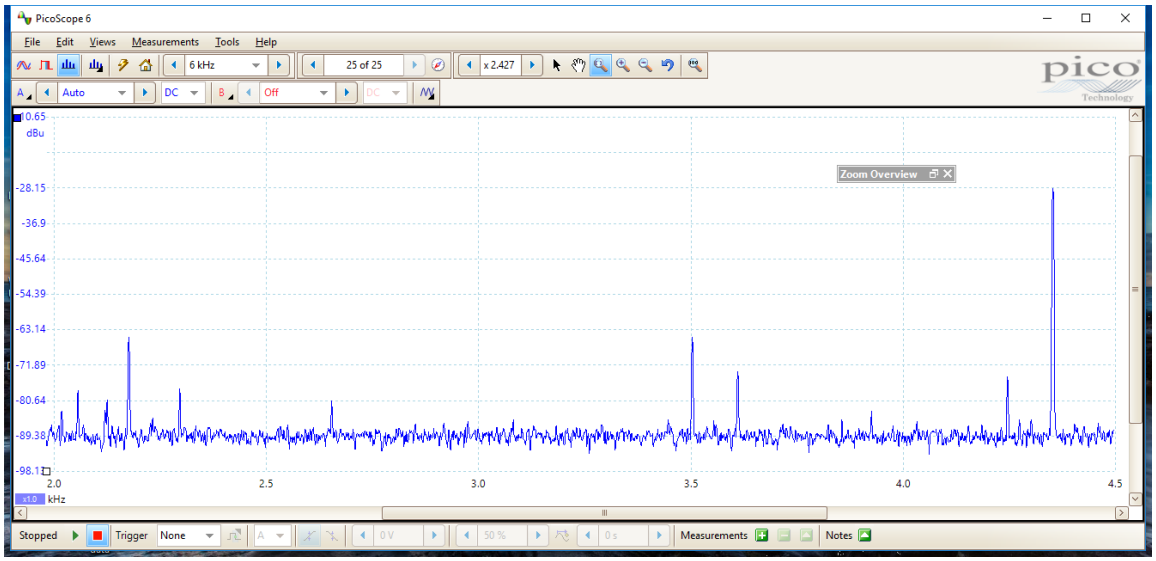


Figure 68. Excited higher order mode of the square glass slide. Note the -28.15 dBu peak near 4300 Hz at twice the amplitude of the wire actuated, first mode peak. It is not yet clear which mode it is, since it is ~1000Hz from the simulated value for the second mode. The geometry of this glass samples is not well defined.

The two definitions given for Q in this thesis (the number of cycles the system oscillates through before damping down to 1/e of the initial amplitude, and the frequency over bandwidth) correspond to two different methods for measuring the Q but they are equivalent. The Q value for the system should not change depending on which method is used. Therefore, the Q value found measuring the resonant width, figure 63, at 1818 Hz should be compatible with the Q measured from the time to ring down by 1/e. Measurements were performed to do this comparison, laying the groundwork for future Q determinations of the coated membrane samples in a vacuum chamber.

Resonance width measurements are generally better to measure low Q resonances, or resonances in high mechanical noise environments, while the ring-down method yields more precision for very high Q systems where the noise environment is good enough to fit the oscillation amplitude over many periods.

Ring-down Measurements of Q

To perform ring-down, or equivalently ring-up measurements it is necessary to excite the oscillator for some time at its resonant frequency and then let it ring down for a similar time. The ring-up and ring-down times should last for a time (ideally at least 3 times) longer than Q oscillations.

We used a square wave output from a function generator to gate the sine wave actuation frequency output from a second function generator. With this setup, we were able to control the amount of time the sample would be subjected to ring-up or ring-down, turning it on and off for set intervals. We then captured the data the QPSPD delivered on the oscilloscope. We observed "ring-up" to the highest amplitude of oscillation during actuation, then exponential decay when the actuation was turned off. The data were fit to curves in Mathematica. The steps are pictured, and described below.

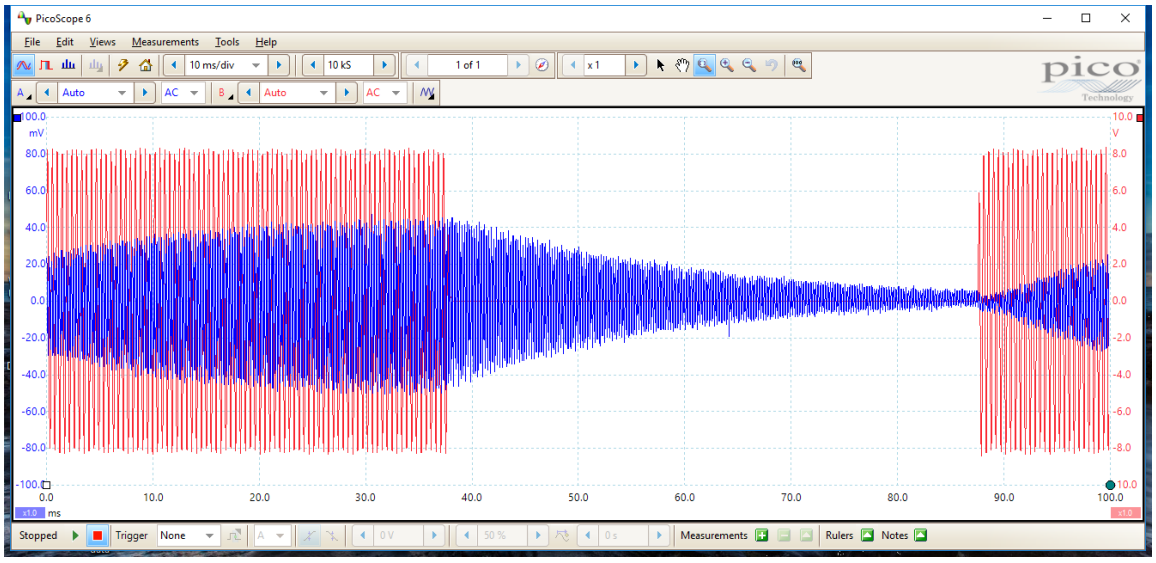


Figure 69. Captured data for a ring-down measurement. The red wave form is the actuation signal being pulsed once every 50 ms. The blue waveform is from the QPSPD. The sample "rings up" as it is driven until the driving is cut off. Note the very clear ring-down when the actuation stops. The exponential parameters that describe this decay are then fit to the data to extract the Q value.

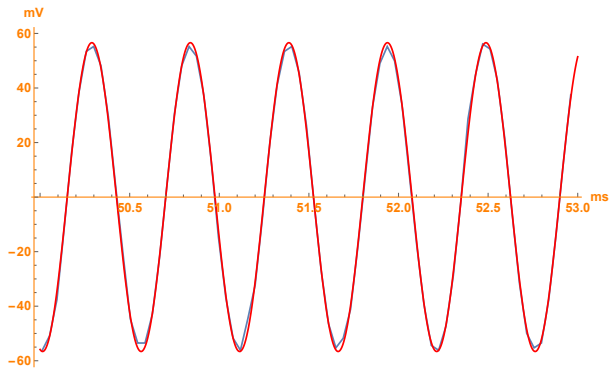


Figure 70. The fit for a short portion of the period before the actuation is turned off is in good agreement with the data. Note that this frequency corresponds to the driver frequency, and may be different from that of the free oscillator. The driver frequency should be taken only as an indicative starting point for the ring-down fit, which will find the true oscillator frequency. If the driver is slightly off-resonance the excitation amplitude will be limited. In this case tuning the driver frequency is easy because the Q is only ~ 30. The peak width is roughly f/Q ~ 60 Hz at 1/e, tuning the driver to resonance within 2-3 Hz is sufficient. Finding the maximum of the excitation would be more difficult for high Q systems. It can be found comparing the phase of the exciting driver signal with the measured oscillator signal. The frequency of the resonance will be marked by a 90^{o} phase shift.

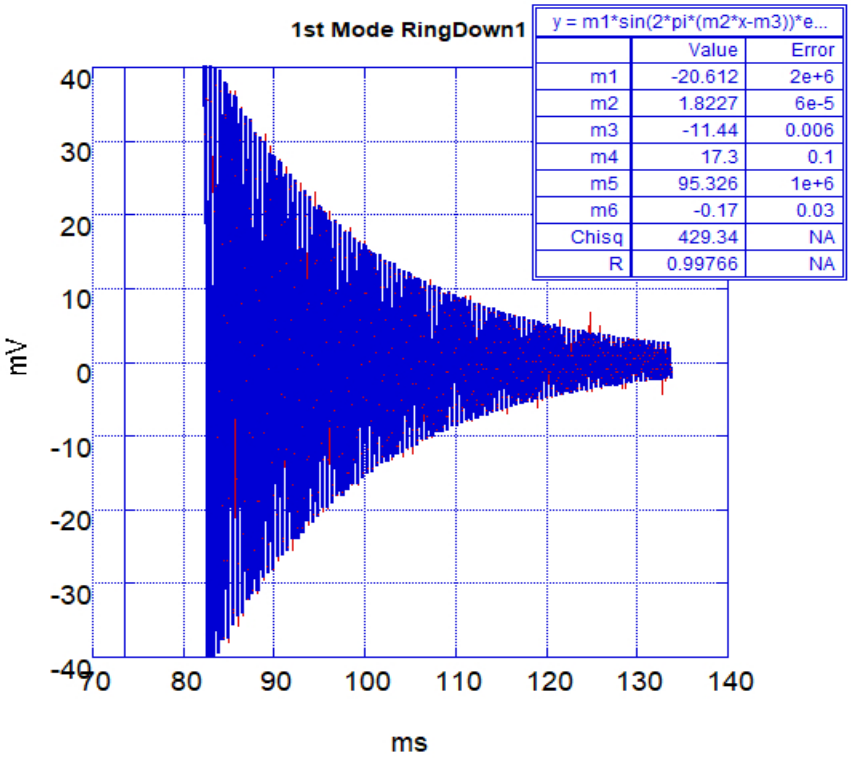


Figure 71. The fit to the ring-down measurement made in KaleidaGraph. The blue curve is the fit superimposed over the red data. Note the large error for parameters m1 and m5. This is an indicator that the fit function was not correct. The two parameters offset each other and may be changed by a large amount without effecting the final result of the fit. The parameter used to extract the Q is m4~17.3.

The functional form used or the fit to the ring-down data of figure 71 is

$$Fit = B\ Sin[2\pi(f_0 t + \phi)]e^{\frac{-t+s}{\alpha}} - d \tag{82}$$

where α holds the Q information since it is related to the damping time of the exponential. Six ring-down measurements were compared to find the average value for α as well as the standard deviation.

Measurement	α
1	17.3
2	16.8
3	16.9
4	17.3
5	17.0
6	16.5

Table 12. The α values extracted from the fit parameters for six ring-down measurements of the first mode for the single slide glass sample. These values give a standard deviation value of +/- 0.3.

The average value for α along with the error using the standard deviation from the mean is 17.0 +/-0.3. This value is used to calculate the Q by solving

$$\frac{1}{e} = e^{-\frac{\tau}{17.0}} \tag{83}$$

for the time, τ which is clearly 17.0 ms, the ring-down time. That is then multiplied (equation 69) with ½ times the frequency found with the average parameter m2 in figure 71 (1.8227 kHz) to deliver the value for Q from the ring-down procedure. This gives the final value for the Quality factor of 15.5+/-0.3. The difference between the Q value found

for the sample using the sweep method (Q~14.7) as opposed to the ring-down measurement (Q~15.5) is approximately 5%.

We will continue to improve the precision of both methods and will perform more measurements, yet the close agreement for this first attempt illustrates the viability of the two methods used in tandem to determine the Q of a sample. Some of the next steps will include extending the period of the sweep and making more sweep measurements so that an average value for the Γ parameter can be used to find the standard deviation.

4.6 Observations of the Effects of Depositing Coatings on the Membrane

A 100-nm thick Silicon Nitride membrane sample, 5mm square, was coated with 100nm of the low index of refraction material, SiO_2 using Ion Beam-Assisted deposition. This was achieved at the coating facility at The University of Sannio, in Benevento, Italy. It was observed that the coated sample exhibited a wrinkled texture that may be indicative of overall negative tension. That system possesses no real oscillatory modes and cannot be used to measure the Q of the coatings. More coating tests will be performed, both with nano-layer coatings and thicker membranes. Ideally, a combination will be found of membrane and coating thickness that will yield positive overall tension. It may be possible to dial in the desired resonant frequency range of the coated system by adjusting these parameters along with the parameters of deposition.

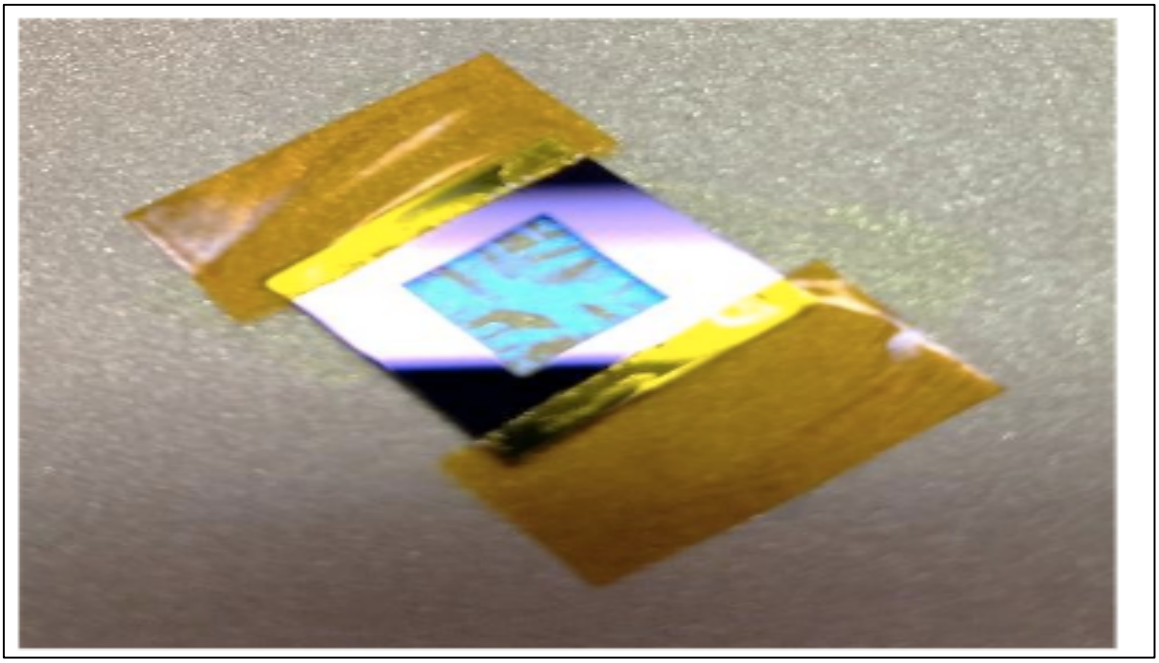


Figure 72. 100nm thick membrane coated with 100nm of Silica. Note the wrinkled texture that may be indicative of negative overall tension.

CHAPTER 5

Conclusion

The following steps were done in the development towards a Q measurement of a coated sample in vacuum.

- Tests were made of the capabilities of the electrostatic actuating system
- Tested the optical lever and QPSPD
- Tests were performed to determine techniques for gluing the samples
- Q measurements were made of a glass sample in air by sweeping through a range of frequencies to measure the peak width, and with ring-down measurements.
- Established the precision of the data acquisition methods by finding best curve fitting parameters, and standard deviation
- COMSOL simulations were made of different membrane thicknesses and sizes that may possess resonant frequencies within the range of the current GW detectors.
- Observed the state of a coating deposited on an actual membrane sample

There are many next steps for the researchers.

- Build the vacuum chamber with electrical feedthrough ports and windows for the optical lever
- Design and build remote controlled actuation system so that the pin or comb may be brought as close as needed to the sample inside vacuum
- Mount the island mass samples in our possession and measure their Q's

- Perform accurate COMSOL simulations to properly model the island mass in membrane system, as well as the relation between coating tension and final overall tension of the coated membrane.

It is possible that the membranes, regardless of thickness and shape, may not be able to maintain positive tension when coated with the optical coatings to be tested. Q measurements may still be made using other methods like GeNS. The author has participated in one GeNS measurement at Caltech and we may be able to continue with that as a resource. While the Dilution Factor from the GeNS measurement technique is not as good as the coated membrane would allow, it is still much more precise than the cantilever method and efforts are being made to coat on thinner disks ~100 microns. Yet, early coating tests have shown that 100 micron fused silica disks shatter after being coated, perhaps due to the tension of the coating.

The steps that have already been taken by this group will allow the next researchers to move forward much more easily, assisting them in the effort to characterize optical coatings and coating methods that will be applied to the next generation of Gravitational Wave detectors to lower their noise. Achieving this will directly expand the scope of our view into the Universe.

References

Press, W. H., & Thorne, K. S. (1972). Gravitational-wave astronomy. *Annual Review of Astronomy and Astrophysics*, *10*(1), 335-374.

Misner, T., & Thorne, K. S. (1973). Wheeler, Gravitation. *R. Adler, M. Bazin, and M. Schiffer, Introduction to General Relativity*, 330.

Scientific, L. I. G. O., Abbott, B. P., Abbott, R., Abbott, T. D., Acernese, F., Ackley, K., ... & Adya, V. B. (2017). GW170104: observation of a 50-solar-mass binary black hole coalescence at redshift 0.2. *Physical Review Letters*, *118*(22), 221101.

Abbott, B. P., Abbott, R., Abbott, T. D., Acernese, F., Ackley, K., Adams, C., ... & Affeldt, C. (2017). GW170817: observation of gravitational waves from a binary neutron star inspiral. *Physical Review Letters*, *119*(16), 161101.

Moore, C. J., Cole, R. H., & Berry, C. P. (2014). Gravitational-wave sensitivity curves. *Classical and Quantum Gravity*, *32*(1), 015014.

Thorne, K. S., & Winstein, C. J. (1999). Human gravity-gradient noise in interferometric gravitational-wave detectors. *Physical Review D*, *60*(8), 082001.

Harry, Gregory M., Andri M. Gretarsson, Peter R. Saulson, Scott E. Kittelberger, Steven D. Penn, William J. Startin, Sheila Rowan et al. "Thermal noise in interferometric gravitational wave detectors due to dielectric optical coatings." *Classical and Quantum Gravity* 19, no. 5 (2002): 897.

Reif, F. (1965). *Fundamentals of statistical mechanics*. McGraw Hill.

Callen, H. B., & Greene, R. F. (1952). On a theorem of irreversible thermodynamics. *Physical Review*, *86*(5), 702.

Harry, G. M., & LIGO Scientific Collaboration. (2010). Advanced LIGO: the next generation of gravitational wave detectors. *Classical and Quantum Gravity*, *27*(8), 084006.

Wu, J., Mizuno, Y., Tabaru, M., & Nakamura, K. (2016). Measurement of mechanical quality factors of polymers in flexural vibration for high-power ultrasonic application. *Ultrasonics*, *69*, 74-82.

Braccini, S., Casciano, C., Cordero, F., Corvace, F., De Sanctis, M., Franco, R., ... & Rapagnani, P. (2000). The maraging-steel blades of the Virgo super attenuator. *Measurement Science and Technology*, *11*(5), 467.

Zwickl, B. M., Shanks, W. E., Jayich, A. M., Yang, C., Bleszynski Jayich, A. C., Thompson, J. D., & Harris, J. G. E. (2008). High quality mechanical and optical properties of commercial silicon nitride membranes. *Applied Physics Letters*, *92*(10), 103125.

Abernathy, M. R., Harry, G. M., Travasso, F., Martin, I., Reid, S., Rowan, S., ... & Armandula, H. (2008). The effects of heating on mechanical loss in tantala/silica optical coatings. *Physics Letters A*, *372*(2), 87-90.

Martin, P. J. (1986). Ion-based methods for optical thin film deposition. *Journal of materials science*, *21*(1), 1-25.

Levin, Y. (1998). Internal thermal noise in the LIGO test masses: A direct approach. *Physical Review D*, *57*(2), 659.

Li, T., Sandoval, F. A. A., Geitner, M., Bellon, L., Cagnoli, G., Degallaix, J., ... & Michel, C. (2014). Measurements of mechanical thermal noise and energy dissipation in optical dielectric coatings. *Physical Review D*, *89*(9), 092004.

Granata, M., Saracco, E., Morgado, N., Cajgfinger, A., Cagnoli, G., Degallaix, J., ... & Pinard, L. (2016). Mechanical loss in state-of-the-art amorphous optical coatings. *Physical Review D*, *93*(1), 012007.

Vajente, G., Ananyeva, A., Billingsley, G., Gustafson, E., Heptonstall, A., Sanchez, E., & Torrie, C. (2017). A high throughput instrument to measure mechanical losses in thin film coatings. *Review of Scientific Instruments*, *88*(7), 073901.

Glover, L., Goff, M., Linker, S., Neilson, J., Patel, J., Pinto, I., ... & Chao, S. (2018, February). A Multi-Step Approach to Assessing LIGO Test Mass Coatings. In *Journal of Physics: Conference Series* (Vol. 957, No. 1, p. 012010). IOP Publishing.

Cole, G. D., Zhang, W., Martin, M. J., Ye, J., & Aspelmeyer, M. (2013). Tenfold reduction of Brownian noise in high-reflectivity optical coatings. *Nature Photonics*, *7*(8), 644.

Griffiths, D. J. (1962). *Introduction to electrodynamics* (p. 609). Prentice Hall.